Distributed quantum sensing with squeezed-vacuum light in a configurable array of Mach-Zehnder interferometers

Marco Malitesta [1,2] Augusto Smerzi [1] and Luca Pezzè [1]
[1] *QSTAR, INO-CNR and LENS, Largo Enrico Fermi 2, 50125 Firenze, Italy*
[2] *Università degli Studi di Napoli "Federico II", Via Cinthia 21, 80126 Napoli, Italy*

(Received 20 June 2023; accepted 1 August 2023; published 29 September 2023)

We study an entangled distributed quantum sensing scheme based on an array of d Mach-Zehnder interferometers (MZIs) for the estimation of relative phase shifts. The scheme uses d coherent states and a single squeezed-vacuum state that is distributed among the MZIs by a quantum circuit (QC). The protocol can be optimized analytically: it overcomes the shot-noise limit and reaches the Heisenberg limit with respect to the average total number of probe particles, $\bar{n}_T$, for the estimation of arbitrary linear combinations of the d phases. We compare the entangled strategy with a separable one that uses d coherent and d squeezed-vacuum states and the same $\bar{n}_T$. The entangled strategy benefits for a substantial reduction of resource overhead and can achieve a maximum gain equal to d when using the same total squeezed-light intensity as the separable strategy. Interestingly, the entangled strategy using a single squeezed-vacuum state can reach the same sensitivity as the separable strategy that uses d copies of the same state. Finally, given a random choices of the QC, we identify the optimal linear combination of the phases that can be estimated with maximum sensitivity. Our scheme paves the ways for a variety of applications in distributed quantum sensing with photonic and atomic interferometers.

DOI: 10.1103/PhysRevA.108.032621

I. INTRODUCTION

Optical interferometry exploiting squeezed light [1–4] has been—since the pioneering proposal by Caves [5]—a cornerstone of theoretical [6–12] and experimental [13–17] photonic quantum sensing [18–22]. A Mach-Zehnder interferometer (MZI) with a high-power coherent state in one input port and a low-intensity squeezed-vacuum light in the other input can reach a phase estimation uncertainty $\Delta^2\theta = e^{-2r}/\bar{n}_T$ [5], where $r \geqslant 0$ is the squeezing parameter, $\bar{n}_T$ is the average total number of photons in the input state, and θ is the relative phase shift between the two arms of the MZI. This scheme can overcome the shot-noise (SN) limit $\Delta^2\theta_{\rm SN} = 1/\bar{n}_T$ by an amount depending on the squeezing strength r. Currently, squeeze factors of more than 10 dB have been observed in several experiments [18,20,23,24]. Furthermore, when the coherent and the squeezed-vacuum states have approximately the same intensity, the MZI can achieve the Heisenberg limit (HL) $\Delta^2\theta_{\rm HL} = 1/\bar{n}_T^2$ [8]. This prediction has been associated [8,25] with the onset of NOON states after the first beam splitter of the MZI, as verified experimentally in Ref. [26]. Overcoming the SN is practically relevant when there are constraints limiting the total light intensity inside the interferometer [27], as in imaging [28,29], microscopy [30], and the probing of biological samples [31]. In gravitational wave detection [32–38], the quantum-enhancement offered by squeezing allows one to boost substantially the rate of detectable events. Squeezed-vacuum states also can be generated via spin-changing collisions in a Bose-Einstein condensate [39–41] and used to enhance the sensitivity of atomic MZIs [42,43].

In this paper we generalize single phase sensing using a MZI with coherent and squeezed-vacuum input light [5–9] to the simultaneous estimation of $d > 1$ relative phase shifts in an array of spatially-distributed MZIs; see Fig. 1(a). This system realizes a distributed quantum sensing scheme [44] that is relevant in quantum optics, as well as in atomic interferometry. It encompasses a variety of interesting possible applications, including clocks [45,46] and spatial magnetometers [47–50]. Compared to other distributed quantum sensing protocols discussed in the literature [44], our scheme, using Gaussian states, is prone to analytical optimizations under different constraints and is expected robust to losses. Due to the use of MZIs, the sensitivity bounds can be clearly identified in terms of the average total number of particles in the input state, $\bar{n}_T$, without ambiguities related to the resource cost necessary to establish a phase reference [51–53].

In our scheme, Fig. 1(a), a single squeezed-vacuum state $|\xi\rangle$ is first split by a linear quantum circuit (QC) implementing a d-mode splitting [54,55]. The QC can be realized, in practice, by a sequence of two-mode linear operations [56,57] and generates entanglement among the d output modes $b_1, \ldots, b_d$. Each mode b_j is used as one input of the jth MZI of the sensing array ($j = 1, \ldots, d$), the other input a_j being in a coherent state. The two input modes mix at a balanced beam splitter, encode a relative phase θ_j, and are detected after a final beam splitter. The overall goal is to estimate *arbitrary linear combinations* $\boldsymbol{v}\cdot\boldsymbol{\theta} = \sum_{j=1}^{d} v_j\theta_j$ of the d phase shifts $\boldsymbol{\theta} = \{\theta_1, \ldots, \theta_d\}$, where $\boldsymbol{v} = \{v_1, \ldots, v_d\}$ is a real vector. Our main results are the following:

(1) We optimize the entangled strategy of Fig. 1(a) over both the QC and the amplitudes of the d coherent states. We show that it is possible to estimate any $\boldsymbol{v}\cdot\boldsymbol{\theta}$ with the same sensitivity scaling with $\bar{n}_T$ as that obtained for the estimation of a single phase shift in a MZI, using same squeezed-vacuum

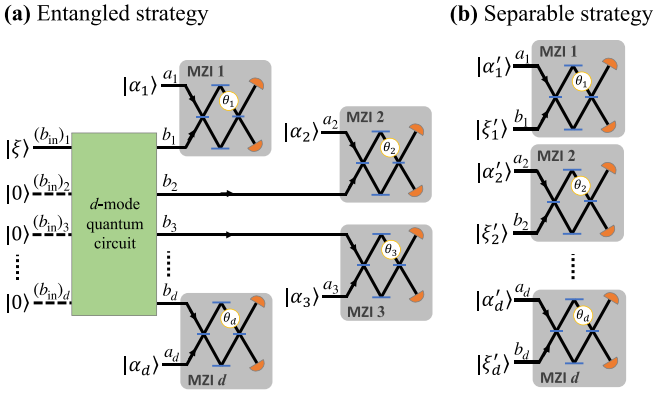

FIG. 1. (a) Distributed quantum sensing scheme using d MZIs. The input of the jth MZI is given by a coherent state $|\alpha_j\rangle$ in the mode a_j, while the other input b_j is one of the outputs of a linear d-mode QC. The input of the QC is a single squeezed-vacuum state $|\xi\rangle$, which is mixed with $d-1$ vacuum states $|0\rangle$. Since the output state of the d-mode QC is mode entangled, we identify the scheme of panel (a) as an entangled distributed sensing strategy. Instead, in the separable strategy of panel (b), the different MZIs are independent. The jth MZI has a coherent state $|\alpha'_j\rangle$ in the input mode a_j and a squeezed-vacuum state $|\xi'_j\rangle$ in the mode b_j. In both strategies, $\theta_1,\ldots,\theta_d$ are relative phase shifts in each MZI.

state and total coherent state intensity. In particular, using an estimation strategy based on the method of moments, we predict sub-SN sensitivities with respect to the average number of photons in the probe state, $\bar{n}_T$. Furthermore, by measuring the number of photons at the output ports of the MZIs, it is possible to saturate the quantum Cramér-Rao bound and reach the Heisenberg limit $\Delta^2(\boldsymbol{v}\cdot\boldsymbol{\theta}) = 1/\bar{n}_T$, when optimizing the relative intensity of the squeezed state.

(2) In the weak-squeezing regime, the multiparameter sensitivity $\Delta^2(\boldsymbol{v}\cdot\boldsymbol{\theta})$ can be written as the variance of a collective quadrature depending on $\boldsymbol{v}$. We show that the QC is able to split the state $|\xi\rangle$ so as to squeeze such a quadrature variance. This possibility is prevented in the separable strategy of Fig. 1(b) that instead requires d squeezed-vacuum states (one for each MZI) in order to achieve sub-SN sensitivities for generic $\boldsymbol{v}\cdot\boldsymbol{\theta}$. This key difference is responsible for the advantage of the entangled scheme over the separable one.

(3) The entangled strategy overcomes the separable one, for every $\boldsymbol{v}\cdot\boldsymbol{\theta}$, in several relevant conditions and under different constraints. The maximum gain is a factor d, equal to the number of parameters to estimate. An interesting comparison is done when the separable strategy of Fig. 1(b) uses d copies of $|\xi\rangle$. In this case, the entangled scheme can perform equally well as the separable one, with the benefit of a substantial reduction of resource overhead.

(4) For any given QC transformation, we identify optimal $\boldsymbol{v}\cdot\boldsymbol{\theta}$ to be estimated with the highest possible sensitivity. This optimization problem is solved by the diagonalization of $d\times d$ matrices. In particular, we show that sensitivity regimes and gains are robust against random choices of the QC.

We notice that the comparison between entangled and separable strategies for multiparameter estimation, already discussed for various schemes [58–68], has led to some controversies. In our case, resources, bounds, and constraints are clearly identified in terms of $\bar{n}_T$, leading to clear conclusions. The effect of noise and imperfections is also included in the analysis. On the practical side, our findings pave the way toward distributed multiphase estimation using quantum resources that are common to many laboratories with photons and atoms.

II. DISTRIBUTED QUANTUM SENSING

A. Definition and strategies

A generic multiparameter estimation problem consists of inferring d unknown parameters $\boldsymbol{\theta} = \{\theta_1,\ldots,\theta_d\}$ of a quantum device. In a distributed scenario, the parameters are encoded in independent (e.g., spatially separated) modes or interferometers. The parameter encoding is thus described by commuting transformations. An example is $e^{-i\boldsymbol{\theta}\cdot\hat{\boldsymbol{H}}} = \otimes_{j=1}^{d} e^{-i\hat{H}_j\theta_j}$, where the generators of the unitary transformation, $\hat{\boldsymbol{H}} = \{\hat{H}_1,\ldots,\hat{H}_d\}$, is a set of commuting Hermitian operators, $[\hat{H}_j,\hat{H}_k]=0$ for $j,k=1,\ldots,d$. The sensing protocol can follow *entangled* or *separable* strategies [54,55,59,62,69]. In the former case, the probe $\hat{\rho}$ is prepared in a mode-entangled state, while the latter uses the product state $\bigotimes_{j=1}^{d}\hat{\rho}_j$, where $\hat{\rho}_j$ is the probe state of the jth sensor. An interesting possibility is to consider local measurements at each sensor, without requiring a mode-entangled measure (a distributed sensing scheme based on a final recombination of parameter-sensing modes has been considered in Refs. [60,66,68,70–72]): local measurements (although being suboptimal in general) can have a practical advantage when the sensing modes are spatially delocalized [73].

B. Figure of merit

In this paper we use, as figure of merit, the variance of a given linear combination $\boldsymbol{v}\cdot\boldsymbol{\theta} = \sum_{j=1}^{d} v_j\theta_j$ of the d parameters $\boldsymbol{\theta}$ [54,55,59,60,62,73–77]. In the following we take real coefficients v_j (either positive or negative). We also consider the normalization $|\boldsymbol{v}|^2 = \sum_{j=1}^{d} v_j^2 = 1/d$, without loss of generality. A relevant example is the average $(\theta_1+\theta_2+\cdots+\theta_d)/d$, corresponding to $v_j = 1/d$.

The method of moments is a feasible and general approach to multiparameter estimation [67]. Here it is based on a set of d Hermitian and commuting measurement operators $\hat{X}_j$ whose mean $\langle\hat{X}_j\rangle$ is a monotonic function of θ_j only. The estimation method consists in repeating the measurement of the local observable $\hat{X}_j$ several times. Taking the sample average $\bar{X}_j$ and inverting the equation $\langle\hat{X}_j\rangle = \bar{X}_j$ provides an estimate of θ_j. The method achieves [67]

$$\Delta^2(\boldsymbol{v}\cdot\boldsymbol{\theta})_{\rm em} = \boldsymbol{v}^T\boldsymbol{\mathcal{M}}^{-1}\boldsymbol{v}, \tag{1}$$

where $\boldsymbol{\mathcal{M}} = \boldsymbol{G}^T\boldsymbol{\Gamma}^{-1}\boldsymbol{G}$, $\boldsymbol{G}_{jk} = \partial\langle\hat{X}_j\rangle/\partial\theta_k$, and $\boldsymbol{\Gamma}_{jk} = \langle\hat{X}_j\hat{X}_k\rangle - \langle\hat{X}_j\rangle\langle\hat{X}_k\rangle$ are $d\times d$ matrices, and the expectation values are calculated with respect to the joint output state of the d sensors, $e^{-i\hat{\boldsymbol{H}}\cdot\boldsymbol{\theta}}\hat{\rho}e^{i\hat{\boldsymbol{H}}\cdot\boldsymbol{\theta}}$. The covariance matrix $\boldsymbol{\Gamma}$ expresses correlations between measurement observables. These correlations are directly linked to mode entanglement in the probe state $\hat{\rho}$ and can be engineered to enhance the sensitivity in the estimation of certain combinations $\boldsymbol{v}\cdot\boldsymbol{\theta}$. In separable

strategies, $\mathbf{\Gamma}$ is diagonal and Eq. (1) becomes

$$\Delta^2(\boldsymbol{v}\cdot\boldsymbol{\theta})_{\rm sm}=\sum_{j=1}^{d}\frac{v_j^2}{M_j}, \tag{2}$$

where $M_j=\Delta^2\hat{X}_j/(d\langle\hat{X}_j\rangle/d\theta_j)^2$ and $\Delta^2\hat{X}_j=\langle\hat{X}_j^2\rangle-\langle\hat{X}_j\rangle^2$, with the expectation values calculated on the output state of the jth sensor, $e^{-i\hat{H}_j\theta_j}\hat{\rho}_j e^{i\hat{H}_j\theta_j}$.

The ultimate sensitivity limit in the estimation of $\boldsymbol{v}\cdot\boldsymbol{\theta}$ is provided by the quantum Cramér-Rao bound (QCRB) [78–80]. In the entangled setting, we have $\Delta^2(\boldsymbol{v}\cdot\boldsymbol{\theta})_{\rm em}\geqslant\Delta^2(\boldsymbol{v}\cdot\boldsymbol{\theta})_{\rm eQ}$, where

$$\Delta^2(\boldsymbol{v}\cdot\boldsymbol{\theta})_{\rm eQ}=\boldsymbol{v}^T\boldsymbol{\mathcal{F}}_{\mathbf{Q}}^{-1}\boldsymbol{v}, \tag{3}$$

and $\boldsymbol{\mathcal{F}}_{\mathbf{Q}}$ is the $d\times d$ quantum Fisher information matrix (QFIM) [81]. If the probe state is pure, $\hat{\rho}=|\psi\rangle\langle\psi|$, then the QFIM is $(\boldsymbol{\mathcal{F}}_{\mathbf{Q}})_{jk}=4(\langle\psi|\hat{H}_j\hat{H}_k|\psi\rangle-\langle\psi|\hat{H}_j|\psi\rangle\langle\psi|\hat{H}_k|\psi\rangle)$ and Eq. (3) can be saturated by optimal measurements and estimators [82,83]. In the separable setting, we have $\Delta^2(\boldsymbol{v}\cdot\boldsymbol{\theta})_{\rm sm}\geqslant\Delta^2(\boldsymbol{v}\cdot\boldsymbol{\theta})_{\rm sQ}$, where

$$\Delta^2(\boldsymbol{v}\cdot\boldsymbol{\theta})_{\rm sQ}=\sum_{j=1}^{d}\frac{v_j^2}{\mathcal{F}_j}, \tag{4}$$

and $\mathcal{F}_j$ is the (scalar) quantum Fisher information [78,79,84]. For pure states, Eq. (4) is obtained from Eq. (3) when taking the product $|\psi\rangle=\bigotimes_{j=1}^{d}|\psi_j\rangle$ such that $\boldsymbol{\mathcal{F}}_{\mathbf{Q}}$ becomes diagonal with entries $\mathcal{F}_j=(\boldsymbol{\mathcal{F}}_{\mathbf{Q}})_{jj}=4(\langle\psi_j|\hat{H}_j^2|\psi_j\rangle-\langle\psi_j|\hat{H}_j|\psi_j\rangle^2)$.

We recall that the different terms on the right-hand side of Eqs. (1)–(4) are understood as divided by the number of repeated independent measurements m used for the estimation. In particular, Eqs. (1)–(4) can be saturated, in general, for $m\gg 1$. Here and in the following, we neglect the factor m: see Ref. [85] for a multiparameter Bayesian estimation analysis including the number of measurements as a resource.

III. MACH-ZEHNDER SENSOR ARRAY

The distributed quantum sensing scheme considered in this paper consists of an array of d MZIs. The entangled strategy is shown in Fig. 1(a) and the separable one in Fig. 1(b). In both cases it is useful to introduce effective angular momentum operators $(\hat{J}_x)_j=(\hat{a}_j^\dagger\hat{b}_j+\hat{a}_j\hat{b}_j^\dagger)/2$, $(\hat{J}_y)_j=(\hat{a}_j^\dagger\hat{b}_j-\hat{a}_j\hat{b}_j^\dagger)/2i$ and $(\hat{J}_z)_j=(\hat{a}_j^\dagger\hat{a}_j-\hat{b}_j^\dagger\hat{b}_j)/2$, where $\hat{a}_j$ and $\hat{b}_j$ ($\hat{a}_j^\dagger$ and $\hat{b}_j^\dagger$) are bosonic mode annihilation (creation) operators [86]. The jth MZI ($j=1,\dots,d$) is described by the unitary phase-encoding transformation $e^{-i\theta_j(\hat{J}_y)_j}$, where θ_j is a relative phase shift between the two interferometers' arms and $\hat{H}_j=(\hat{J}_y)_j$ is the corresponding Hamiltonian. We have $[\hat{a}_j,\hat{a}_k^\dagger]=[\hat{a}_j,\hat{b}_k^\dagger]=[\hat{a}_j,\hat{b}_k]=0$ for $j\neq k$, which guarantees that $[\hat{H}_j,\hat{H}_k]=0$. Finally, we consider local observable $\hat{X}_j=(\hat{J}_z)_j$, measuring the population difference between the two output ports of the jth MZI.

In the entangled strategy, the input mode a_j of the jth MZI is fed with a coherent state $|\alpha_j\rangle$, where $\alpha_j=|\alpha_j|e^{i\phi_j}$. The other input b_j is an output modes of a QC; see Fig. 1(a). The QC is a mode-mixing passive device that generalizes the familiar two-mode beam splitter to an arbitrary number, d, of modes. The QC is the key element of the entangled strategy. It is described by a $d\times d$ unitary matrix $\boldsymbol{U}_{\rm QC}^\dagger$ implementing the mode transformation $\hat{b}_j=\sum_{k=1}^{d}(\boldsymbol{U}_{\rm QC}^\dagger)_{jk}(\hat{b}_{\rm in})_k=\hat{U}_{\rm QC}(\hat{b}_{\rm in})_j\hat{U}_{\rm QC}^\dagger$ between input $(\hat{b}_{\rm in})_j$ and output $\hat{b}_j$ [see Fig. 1(a)], and $\hat{U}_{\rm QC}^\dagger$ is the corresponding unitary operator. In our study, the multimode input state of the QC, $|\Psi_{\rm in}^{\xi}\rangle$, is given by a squeezed-vacuum state in mode D, while the other input modes are empty:

$$|\Psi_{\rm in}^{\xi}\rangle=|0\rangle_1\otimes\cdots\otimes|0\rangle_{D-1}\otimes|\xi\rangle_D\otimes|0\rangle_{D+1}\otimes\cdots\otimes|0\rangle_d, \tag{5}$$

where $\xi=re^{i\varphi}$ and r is the squeezing parameter and $|0\rangle$ is the vacuum. The QC output state is

$$|\Psi_{\rm QC}\rangle=\hat{U}_{\rm QC}^\dagger|\Psi_{\rm in}^{\xi}\rangle. \tag{6}$$

We also introduce $u_j\equiv(\boldsymbol{U}_{\rm QC}^\dagger)_{jD}=|u_j|e^{i\delta_j}$ with $\boldsymbol{u}=\{u_1,\dots,u_d\}$ being the Dth column vector of the QC matrix $\boldsymbol{U}_{\rm QC}^\dagger$.

The average total number of photons in the input state of Fig. 1(a) is $\bar{n}_T=d\bar{n}_c+\bar{n}_s$, where $\bar{n}_c=\sum_{j=1}^{d}|\alpha_j|^2/d$ is the mean number of photons in each coherent state and $\bar{n}_s=\sinh^2 r$ is the mean number of photons in the squeezed-vacuum state.

A. Method of moments sensitivity and QCRB of the entangled strategy

The inverse moment matrix $\boldsymbol{\mathcal{M}}^{-1}$ as well as the QFIM (and its inverse $\boldsymbol{\mathcal{F}}_{\mathbf{Q}}^{-1}$) can be calculated analytically; see Appendix A 1 for the detailed derivation. In the following, we restrict to the optimal conditions $\theta_j=\pi/2$ and $\sin\chi_j=0$, for $j=1,\dots,d$, where $\chi_j\equiv\phi_j-\varphi/2+\delta_j$. The sensitivity achieved by the method of moments, Eq. (1), is

$$\Delta^2(\boldsymbol{v}\cdot\boldsymbol{\theta})_{\rm em}=-(1-e^{-2r})\left(\sum_{j=1}^{d}\frac{|\alpha_j|\tilde{u}_j v_j}{|\alpha_j|^2-\tilde{u}_j^2\bar{n}_s}\right)^2+\sum_{j=1}^{d}\frac{|\alpha_j|^2+\tilde{u}_j^2\bar{n}_s}{\left(|\alpha_j|^2-\tilde{u}_j^2\bar{n}_s\right)^2}v_j^2, \tag{7}$$

while the QCRB, Eq. (3), is

$$\Delta^2(\boldsymbol{v}\cdot\boldsymbol{\theta})_{\rm eQ}=\frac{1-e^{2r}}{1+(e^{2r}-1)\sum_{j=1}^{d}|\alpha_j|^2\tilde{u}_j^2/\left(|\alpha_j|^2+\tilde{u}_j^2\bar{n}_s\right)}\times\left(\sum_{j=1}^{d}\frac{|\alpha_j|\tilde{u}_j v_j}{|\alpha_j|^2+\tilde{u}_j^2\bar{n}_s}\right)^2+\sum_{j=1}^{d}\frac{v_j^2}{|\alpha_j|^2+\tilde{u}_j^2\bar{n}_s}. \tag{8}$$

Equations (7) and (8) depend on the QC transformation only through the vector $\{\tilde{u}_j\}_{j=1,\dots,d}$, where $\tilde{u}_j\equiv\pm|u_j|$ [87]. Notice that the QCRB is independent from $\boldsymbol{\theta}$. When $\delta_j,\ \phi_j,\ \varphi=0$ (thus satisfying the optimal condition $\sin\chi_j=0$ for all j), the measurement of the number of photons at the output ports of the MZIs is an optimal one, according to Ref. [83], and the QCRB can be saturated. Interestingly, the distributed sensing scheme considered in this paper can reach the optimal

sensitivity without requiring a second QC mixing the outputs of the d interferometers before the final detection.

B. Method of moments sensitivity and QCRB of the separable strategy

In the separable strategy of Fig. 1(b), the jth MZI is fed with a coherent state $|\alpha_j'\rangle$ in mode a_j and a squeezed vacuum state $|\xi_j'\rangle$ in mode b_j, where $\alpha_j' = |\alpha_j'|e^{i\phi_j'}$ and $\xi_j' = r_j' e^{i\varphi_j'}$. Under the optimal phase-locking condition $\sin\chi_j' = 0$, where $\chi_j' = \phi_j' - \varphi_j'/2$, we find [5–8]

$$\Delta^2(\boldsymbol{v}\cdot\boldsymbol{\theta})_{\rm sm} = \sum_{j=1}^{d} \frac{|\alpha_j'|^2 e^{-2r_j'} + (\bar{n}_s')_j}{[|\alpha_j'|^2 - (\bar{n}_s')_j]^2} v_j^2, \tag{9}$$

where $(\bar{n}_s')_j = \sinh^2 r_j'$ is the mean number of photon in the state $|\xi_j'\rangle$. The QCRB, Eq. (4), is [8,9]

$$\Delta^2(\boldsymbol{v}\cdot\boldsymbol{\theta})_{\rm sQ} = \sum_{j=1}^{d} \frac{v_j^2}{|\alpha_j'|^2 e^{2r_j'} + (\bar{n}_s')_j}, \tag{10}$$

and it can be saturated by the measurement of the number of particles at the output ports of each MZI [8]. We emphasize that, differently from the entangled strategy, the separable strategy uses d squeezed-vacuum states. The average total number of particles in the overall input state of the separable sensor is thus $\bar{n}_T' = d\bar{n}_c' + \bar{n}_s'$, where $\bar{n}_c' = \sum_{j=1}^{d} |\alpha_j'|^2/d$ and $\bar{n}_s' = \sum_{j=1}^{d} \sinh^2 r_j'$ is the total mean number of photons in the d squeezed-vacuum states.

IV. OPTIMIZED MULTIPHASE SENSITIVITY

A. Optimized method of moments sensitivity

In this section, we study the sensitivity of the entangled strategy, Eq. (7), optimized over the intensities of the d coherent states and over the QC transformation,

$$\gamma_{\rm em}(\boldsymbol{v}, \bar{n}_s, \bar{n}_T) \equiv \min_{|\alpha_1|^2,\ldots,|\alpha_d|^2,\hat{U}_{\rm QC}} \Delta^2(\boldsymbol{v}\cdot\boldsymbol{\theta})_{\rm em}. \tag{11}$$

We assume optimal phase-matching relations between the coherent and the squeezed state.

As a general result, we notice that inverting the sign of an arbitrary number of components of $\boldsymbol{v}$ leaves $\gamma_{\rm em}(\boldsymbol{v}, \bar{n}_s, \bar{n}_T)$ unaltered, as easily seen from Eq. (7). In the following we will thus restrict to only positive linear combinations, with $v_j \geqslant 0$ for $j = 1, \ldots, d$.

As proved in Appendix A 2, for $\bar{n}_T \gg 2\bar{n}_s$ and any $\boldsymbol{v}$, Eq. (11) becomes

$$\gamma_{\rm em}(\boldsymbol{v}, \bar{n}_s, \bar{n}_T) = \left(\frac{e^{-2r}}{\bar{n}_T} + \frac{\bar{n}_s}{\bar{n}_T^2}\right)\left(\sum_{j=1}^{d} |v_j|\right)^2. \tag{12}$$

for the optimal coherent-state intensities and QC parameters

$$|\alpha_j|^2 = \frac{\bar{n}_c d}{\sum_{k=1}^{d} |v_k|}|v_j|, \quad \text{and} \quad \tilde{u}_j = \frac{1}{\sqrt{\sum_{k=1}^{d} |v_k|}} \frac{v_j}{\sqrt{|v_j|}}, \tag{13}$$

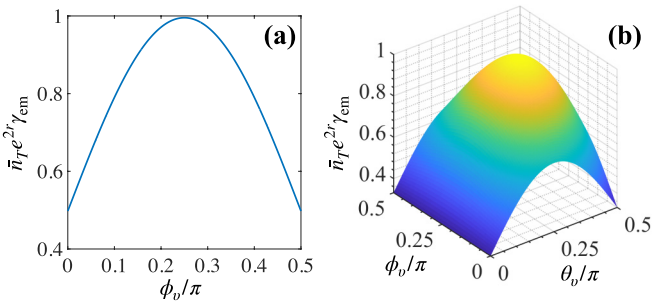

FIG. 2. Optimized sensitivity of the entangled strategy, $\gamma_{\rm em}(\boldsymbol{v}, \bar{n}_s, \bar{n}_T)$, Eq. (12), as a function of $\boldsymbol{v}$, for $d = 2$ (a) and $d = 3$ (b). The vector $\boldsymbol{v}$ is expressed as $\boldsymbol{v}^T = (\cos\phi_v, \sin\phi_v)/\sqrt{2}$, with $\phi_v \in [0, \pi/2]$, for $d = 2$, and as $\boldsymbol{v}^T = (\sin\theta_v\cos\phi_v, \sin\theta_v\sin\phi_v, \cos\theta_v)/\sqrt{3}$, with $\phi_v \in [0, \pi/2]$ and $\theta_v \in [0, \pi/2]$, for $d = 3$. Here $\bar{n}_T = 10^8$ and $\bar{n}_s = 10^2$.

respectively. Equation (12) is plotted in Fig. 2 as a function of $\boldsymbol{v}$ for $d = 2$ and $d = 3$. In particular, Eq. (12) satisfies

$$\gamma_{\rm em}(\boldsymbol{v}_{\rm sing}, \bar{n}_s, \bar{n}_T) \leqslant \gamma_{\rm em}(\boldsymbol{v}, \bar{n}_s, \bar{n}_T) \leqslant \gamma_{\rm em}(\boldsymbol{v}_{\rm av}, \bar{n}_s, \bar{n}_T). \tag{14}$$

In the above equation, $\boldsymbol{v}_{\rm sing}$ indicates any vector with vanishing components except for the jth. This case corresponds to the estimation of a single phase in a MZI [5–9], namely, $\boldsymbol{v}_{\rm sing}\cdot\boldsymbol{\theta} = \theta_j/\sqrt{d}$ with $\boldsymbol{v}_{{\rm sing},j} = 1/\sqrt{d}$, for normalization. The corresponding sensitivity is

$$\gamma_{\rm em}(\boldsymbol{v}_{\rm sing}, \bar{n}_s, \bar{n}_T) = \frac{e^{-2r}}{d\bar{n}_T} + \frac{\bar{n}_s}{d\bar{n}_T^2}, \tag{15}$$

for the optimal choice of parameters: $|\alpha_j|^2 = d\bar{n}_c$, $\tilde{u}_j = 1$ with $\boldsymbol{v}_{{\rm sing},j} \neq 0$, Furthermore, $\boldsymbol{v}_{\rm av} = (1/d, \ldots, 1/d)$ is the average phase, namely, $\boldsymbol{v}_{\rm av}\cdot\boldsymbol{\theta} = (\theta_1 + \cdots + \theta_d)/d$. The corresponding sensitivity is

$$\gamma_{\rm em}(\boldsymbol{v}_{\rm av}, \bar{n}_s, \bar{n}_T) = \frac{e^{-2r}}{\bar{n}_T} + \frac{\bar{n}_s}{\bar{n}_T^2}, \tag{16}$$

for the optimal choice of parameters $|\alpha_j|^2 = \bar{n}_c$ and $\tilde{u}_j = 1/\sqrt{d}$ for $j = 1, \ldots, d$. Remarkably, the lower and upper bounds, Eqs. (15) and (16), respectively, differ by a factor d in the denominator, independently of the normalization of $\boldsymbol{v}$. We thus conclude that, for the estimation of any $\boldsymbol{v}\cdot\boldsymbol{\theta}$, the optimized sensitivity of the entangled strategy, $\gamma_{\rm em}$, is characterized by the same scaling with $\bar{n}_T$ as that obtained for single phase estimation in a MZI when using exactly the same resources. In the following we distinguish different cases.

1. Regime $\bar{n}_T \gg (e^{2r} + 1)\bar{n}_s$

In this regime, Eq. (12) is

$$\gamma_{\rm em}(\boldsymbol{v}, \bar{n}_s, \bar{n}_T) = \frac{e^{-2r}}{\bar{n}_T}\left(\sum_{j=1}^{d} |v_j|\right)^2. \tag{17}$$

It corresponds to a sub-SN uncertainty depending on the squeezing parameter r. As discussed in Sec. V A, Eq. (17) is recovered by a Holstein-Primakoff transformation and can be directly related to quadrature squeezing. Equation (17) is similar to that obtained in Ref. [55] for the sensitivity of distributed

radio-frequency sensing via phase modulation using coherent and squeezed vacuum light and homodyne detection. The main difference is that here $\bar{n}_T$ is the total amount of resources used for the estimation (including probe and measurement) and Eq. (17) shows the possibility of overcoming the SN, $1/\bar{n}_T$. Instead, in Ref. [55] the coherent states necessary for the homodyne detection are not included in the resource cost.

2. Optimal squeezing

We minimize Eq. (12) with respect to $\bar{n}_s$, with fixed $\bar{n}_T$. Assuming $r \gg 1$ (so that $e^{2r} \approx 4\bar{n}_s$), we obtain

$$\min_{\bar{n}_s} \gamma_{\rm em}(\boldsymbol{v}, \bar{n}_s, \bar{n}_T) = \frac{1}{\bar{n}_T^{3/2}} \left(\sum_{j=1}^{d} |v_j| \right)^2, \tag{18}$$

for the optimal value $\bar{n}_s \approx \sqrt{\bar{n}_T}/2$. This predicts a scaling $O(\bar{n}_T^{-3/2})$, faster than the SN. The same scaling has been discussed for single phase estimation in a MZI using coherent and squeezed-vacuum light with optimized intensities; see Refs. [6,7].

3. Transient Heisenberg scaling for $2\bar{n}_s \ll \bar{n}_T \ll (e^{2r}+1)\bar{n}_s$

In this regime, Eq. (12) predicts

$$\gamma_{\rm em}(\boldsymbol{v}, \bar{n}_s, \bar{n}_T) = \frac{\bar{n}_s}{\bar{n}_T^2} \left(\sum_{j=1}^{d} |v_j| \right)^2, \tag{19}$$

which is understood as a Heisenberg scaling, $O(1/\bar{n}_T^2)$, when neglecting the dependence of $\bar{n}_T$ on $\bar{n}_s$ (as approximately valid in the considered regime).

In Fig. 3 we compare a numerical evaluation of Eq. (11) (green dots) for $\boldsymbol{v} = \boldsymbol{v}_{\rm av}$ with the analytical prediction Eq. (16) (thin solid green line) as a function of $\bar{n}_T/\bar{n}_s$. As expected, the two lines agree for $\bar{n}_T \gg 2\bar{n}_s$. We clearly recognize the different regimes discussed above: the dot-dashed line is $e^{-2r}/\bar{n}_T$, the dashed line is $1/\bar{n}_T^{3/2}$, and the dotted line is $\bar{n}_s/\bar{n}_T^2$. In Fig. 3(b) we plot $\min_{\bar{n}_s} \gamma_{\rm em}(\boldsymbol{v}_{\rm av}, \bar{n}_s, \bar{n}_T)$ as a function of $\bar{n}_T$. Circles are numerical results, and the thick solid line is $1/\bar{n}_T^{3/2}$.

B. Optimized quantum Cramér-Rao sensitivity

In analogy with Eq. (11), we also study the optimization of the QCRB,

$$\gamma_{\rm eQ}(\boldsymbol{v}, \bar{n}_s, \bar{n}_T) \equiv \min_{|\alpha_1|^2,\ldots,|\alpha_d|^2, \hat{U}_{\rm QC}} \Delta^2(\boldsymbol{v}\cdot\boldsymbol{\theta})_{\rm eQ}, \tag{20}$$

Similarly to Eq. (14) we have

$$\frac{1}{d(d\bar{n}_c e^{2r} + \bar{n}_s)} \leqslant \gamma_{\rm eQ}(\boldsymbol{v}_{\rm av}, \bar{n}_s, \bar{n}_T) \leqslant \frac{1}{d\bar{n}_c e^{2r} + \bar{n}_s}, \tag{21}$$

where the lower bound is $\gamma_{\rm eQ}(\boldsymbol{v}_{\rm sing}, \bar{n}_s, \bar{n}_T)$ and the upper bound is $\gamma_{\rm eQ}(\boldsymbol{v}_{\rm av}, \bar{n}_s, \bar{n}_T)$ (see Appendix A 2).

1. Regime $\bar{n}_T \gg 2\bar{n}_s$

From Eq. (21), we directly find

$$\frac{e^{-2r}}{d\bar{n}_T} \leqslant \gamma_{\rm eQ}(\boldsymbol{v}, \bar{n}_s, \bar{n}_T) \leqslant \frac{e^{-2r}}{\bar{n}_T}. \tag{22}$$

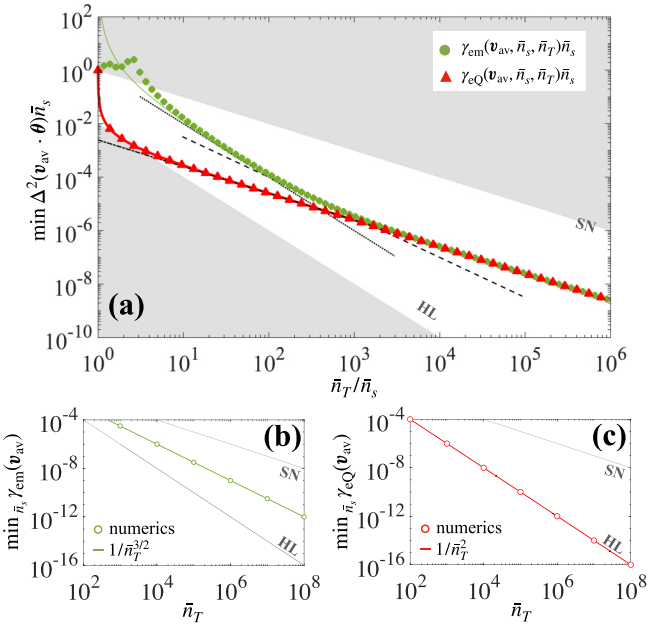

FIG. 3. (a) Optimized sensitivity in the estimation of $\boldsymbol{v}_{\rm av}\cdot\boldsymbol{\theta}$, as a function of $\bar{n}_T/\bar{n}_s$, for fixed $\bar{n}_s = 100$. Green dots are $\gamma_{\rm em}(\boldsymbol{v}_{\rm av}, \bar{n}_s, \bar{n}_T)$, and red triangles $\gamma_{\rm eQ}(\boldsymbol{v}_{\rm av}, \bar{n}_s, \bar{n}_T)$, both evaluated numerically. The thin solid green line is Eq. (16), and the thick solid red line is the upper bound in Eq. (21). Other lines correspond to different limiting behaviors: the dot-dashed line is $e^{-2r}/\bar{n}_T$, the dashed line is $1/\bar{n}_T^{3/2}$, and the dotted line is $\bar{n}_s/\bar{n}_T^2$. Panels (b) and (c) show $\min_{\bar{n}_s} \gamma_{\rm em}(\boldsymbol{v}_{\rm av}, \bar{n}_s, \bar{n}_T)$ and $\min_{\bar{n}_s} \gamma_{\rm eQ}(\boldsymbol{v}_{\rm av}, \bar{n}_s, \bar{n}_T)$, respectively, as a function of $\bar{n}_T$. Circles are numerical results. Thick solid lines are expected analytical behaviors: $1/\bar{n}_T^{3/2}$ (b) and $1/\bar{n}_T^2$ (c). In all panels $d = 2$ and we indicate the SN ($1/\bar{n}_T$) and the HL ($1/\bar{n}_T^2$).

Furthermore, as discussed in Appendix A 3, in this regime we have

$$\gamma_{\rm eQ}(\boldsymbol{v}, \bar{n}_s, \bar{n}_T) = \frac{e^{-2r}}{\bar{n}_T} \left(\sum_{j=1}^{d} |v_j| \right)^2. \tag{23}$$

It should be noticed that Eq. (23) coincides with Eq. (17). However, the latter equation is valid for $\bar{n}_T \gg (e^{2r}+1)\bar{n}_s$, whereas the former for $\bar{n}_T \gg 2\bar{n}_s$. This demonstrates that the method of moments is an optimal estimation strategy in the regime $\bar{n}_T \gg (e^{2r}+1)\bar{n}_s$.

2. Heisenberg limit for $\bar{n}_T \approx 2\bar{n}_s$

We optimize both the upper and lower bounds in Eq. (21) with respect to $\bar{n}_s$, for fixed $\bar{n}_T$. Taking $r \gg 1$ (so that $\bar{n}_s \approx e^{2r}/4$), gives

$$\frac{1}{d\bar{n}_T^2} \leqslant \gamma_{\rm eQ}(\boldsymbol{v}, \bar{n}_s, \bar{n}_T) \leqslant \frac{1}{\bar{n}_T^2}. \tag{24}$$

The value of the squeezing parameter that minimizes the bounds in Eq. (24) is $\bar{n}_s = \bar{n}_T/2$. This is different from the value $\bar{n}_s \approx \sqrt{\bar{n}_T}/2$ that minimizes Eq. (18). The different optimizations also correspond to different scalings, $O(\bar{n}_T^{-3/2})$ and $O(\bar{n}_T^{-2})$, respectively.

A numerical evaluation of $\gamma_{\rm eQ}(\boldsymbol{v}, \bar{n}_s, \bar{n}_T)$ for $\boldsymbol{v} = \boldsymbol{v}_{\rm av}$ is shown in Fig. 3(a) (red triangles). For $\bar{n}_T \gg 2\bar{n}_s$, $\gamma_{\rm eQ}$ agrees with the dot-dashed line $e^{-2r}/\bar{n}_T$, as predicted by Eq. (23). In Fig. 3(c) we plot the numerical calculation of $\min_{\bar{n}_s} \gamma_{\rm eQ}(\boldsymbol{v}_{\rm av}, \bar{n}_s, \bar{n}_T)$ as functions of $\bar{n}_T$ (circles): it perfectly agrees with the expected Heisenberg limit $1/\bar{n}_T^2$ (thick solid line).

C. Optimized sensitivity of the separable strategy

Finally, for comparison, we also minimize the sensitivity of the separable strategy, introducing

$$\gamma_{\rm sm}(\boldsymbol{v}, \bar{n}_s', \bar{n}_T') \equiv \min_{|\alpha_1'|^2,\ldots,|\alpha_d'|^2,r_1',\ldots,r_d'} \Delta^2(\boldsymbol{v}\cdot\boldsymbol{\theta})_{\rm sm}. \tag{25}$$

and

$$\gamma_{\rm sq}(\boldsymbol{v}, \bar{n}_s', \bar{n}_T') \equiv \min_{|\alpha_1'|^2,\ldots,|\alpha_d'|^2,r_1',\ldots,r_d'} \Delta^2(\boldsymbol{v}\cdot\boldsymbol{\theta})_{\rm sq}. \tag{26}$$

The minimum is searched with respect to the d coherent state intensities and squeezing parameters (the optimal phase-matching condition between the coherent and squeezed-vacuum at the input of each MZI is assumed). The optimization of Eq. (25) is generally difficult. We can obtain an analytical expression in the regime $\bar{n}_T' \gg (e^{2r_T'}+1)\bar{n}_s'$ and under the assumption $r_j' \gg 1$, $j = 1,\ldots,d$ (see Appendix A 2):

$$\gamma_{\rm sm}(\boldsymbol{v}, \bar{n}_s', \bar{n}_T') = \frac{e^{-2r_T'}}{\bar{n}_T'}\left(\sum_{j=1}^d |v_j|^{2/3}\right)^3, \tag{27}$$

where $r_T' = \operatorname{arcsinh}\sqrt{\bar{n}_s'}$. The optimal parameters are

$$|\alpha_j'|^2 = \frac{d\bar{n}_c'}{\sum_{k=1}^d |v_k|^{2/3}}|v_j|^{2/3} \quad \text{and} \quad (\bar{n}_s')_j = \frac{\bar{n}_s'}{d\bar{n}_c'}|\alpha_j'|^2. \tag{28}$$

Notice that the optimized QCRB of the separable strategy, $\gamma_{\rm sQ}$, equals the right-hand side of Eq. (27) in the regime $\bar{n}_T' \gg 2\bar{n}_s'$.

V. COMPARISON BETWEEN OPTIMAL ENTANGLED AND SEPARABLE STRATEGIES

In the following, we compare optimal entangled and separable strategies for the estimation of arbitrary linear combinations of the parameters. We first clarify the role of the QC by relating the sensitivity to the quadrature variance in an opportune regime. We then provide a quantitative comparison when considering different constraints on resources.

A. Multimode quadrature squeezing

At the optimal working point $\theta_j = \pi/2$, for all $j = 1,\ldots,d$, Eq. (1) can be written as

$$\begin{aligned}\Delta^2(\boldsymbol{v}\cdot\boldsymbol{\theta})_{\rm em} &= \Delta^2\left[\sum_{j=1}^d \frac{(\hat{J}_x)_j}{\langle(\hat{J}_z)_j\rangle} v_j\right]_{|\Psi_{\rm in}\rangle} \\ &\approx 2\Delta^2\left[\sum_{j=1}^d \hat{x}_j \frac{v_j}{|\alpha_j|}\right]_{|\Psi_{\rm QC}\rangle}.\end{aligned} \tag{29}$$

The mean value and variance after the first equality sign are evaluated on the state $|\Psi_{\rm in}\rangle = |\Psi_{\rm in}^{\alpha}\rangle \otimes |\Psi_{\rm QC}\rangle$, where $|\Psi_{\rm in}^{\alpha}\rangle = \bigotimes_{j=1}^d |\alpha_j\rangle$ is the product of coherent states entering the d MZIs, and $|\Psi_{\rm QC}\rangle$ is given in Eq. (6). The subsequent approximation is obtained by assuming that the numbers of particles in the jth coherent state, $|\alpha_j|^2$, is large enough to replace the mode operator with a number, $\hat{a}_j \sim |\alpha_j| e^{i\phi_j}$, also implying $(\hat{J}_x)_j \approx |\alpha_j|\hat{x}_j/\sqrt{2}$, $(\hat{J}_y)_j \approx |\alpha_j|\hat{p}_j/\sqrt{2}$ and $(\hat{J}_z)_j \approx |\alpha_j|^2/2$, where $\hat{x}_j = (e^{-\phi_j}\hat{b}_j + e^{i\phi_j}\hat{b}_j^\dagger)/\sqrt{2}$ and $\hat{p}_j = (e^{-i\phi_j}\hat{b}_j - e^{i\phi_j}\hat{b}_j^\dagger)/\sqrt{2}i$ are quadrature operators satisfying the canonical commutation relation $[\hat{x}_j, \hat{p}_j] = i$. On the second line of Eq. (29), mean values and variances are evaluated on state $|\Psi_{\rm QC}\rangle$. Equation (29) reveals that minimizing the estimation uncertainty is equivalent to looking for the minimum variance of a linear combination of quadrature operators. We then plug the optimal value of $|\alpha_j|$ given by Eq. (13), obtaining

$$\Delta^2(\boldsymbol{v}\cdot\boldsymbol{\theta})_{\rm em} \approx \frac{2}{d\bar{n}_c}\left(\sum_{j=1}^d |v_j|\right)^2 \Delta^2\left[\sum_{j=1}^d \hat{x}_j\tilde{v}_j\right]_{|\Psi_{\rm QC}\rangle}, \tag{30}$$

where $\tilde{v}_j = v_j/(|v_j|\sum_{k=1}^d |v_k|)^{1/2}$. We can rewrite the variance on the right-hand side as

$$\begin{aligned}\Delta^2\left[\sum_{j=1}^d \hat{x}_j\tilde{v}_j\right]_{|\Psi_{\rm QC}\rangle} &= \Delta^2\left[\sum_{j=1}^d \frac{e^{-i\varphi/2}w_j\hat{b}_j + e^{i\varphi/2}w_j^*\hat{b}_j^\dagger}{\sqrt{2}}\right]_{|\Psi_{\rm QC}\rangle} \\ &= \langle\Psi_{\rm in}^{\xi}|\hat{U}_{\rm QC}\hat{W}^\dagger\hat{x}_D^2\hat{W}\hat{U}_{\rm QC}^\dagger|\Psi_{\rm in}^{\xi}\rangle,\end{aligned} \tag{31}$$

where $|\Psi_{\rm in}^{\xi}\rangle$ is given in Eq. (5) and $w_j = e^{i(\varphi/2-\phi_j)}\tilde{v}_j$. Furthermore, we have used the relation $\sum_{j=1}^d w_j\hat{b}_j = \hat{W}^\dagger\hat{b}_D\hat{W}$, where D refers to the squeezed-vacuum input mode, $\hat{x}_D = (e^{-i\varphi/2}\hat{b}_D + e^{i\varphi/2}\hat{b}_D^\dagger)/\sqrt{2}$ and $\hat{W}$ is a unitary operator [88]. We have also rewritten the variance as an average value by noticing that $\langle\Psi_{\rm QC}|\hat{x}_j|\Psi_{\rm QC}\rangle = 0$ and made use of Eq. (6). Finally, by choosing $\hat{U}_{\rm QC} = \hat{W}$, we can reverse the unitary transformation $\hat{W}$ acting on $\hat{x}_D$ and get

$$\Delta^2\left[\sum_{j=1}^d \hat{x}_j\tilde{v}_j\right]_{|\Psi_{\rm QC}\rangle} = \Delta^2[\hat{x}_D]_{|\xi\rangle_D}. \tag{32}$$

This equation conveys one of the key messages of this paper: the optimized quantum circuits transform the squeezing in the input quadrature D into the squeezing of a linear combination of the d quadrature operators depending on the arbitrary $\boldsymbol{v}$. Such transformation enhances the sensitivity in the estimation of the corresponding linear combination $\boldsymbol{v}\cdot\boldsymbol{\theta}$ of the parameters. This idea is summarized schematically in Fig. 4. By plugging Eq. (32) into Eq. (30), we obtain

$$\Delta^2(\boldsymbol{v}\cdot\boldsymbol{\theta})_{\rm em} \approx \frac{2}{d\bar{n}_c}\left(\sum_{j=1}^d |v_j|\right)^2 \Delta^2[\hat{x}_D]_{|\xi\rangle_D}. \tag{33}$$

Finally, taking $\Delta^2[\hat{x}_D]_{|\xi\rangle_D} = e^{-2r}/2$, namely, the squeezed (for $r > 0$) quadrature variance associated to the squeezed-vacuum state injected into input mode D, we recover Eq. (17), with $d\bar{n}_c \approx \bar{n}_T$. Notice also that, from the relation $\hat{U}_{\rm QC} = \hat{W}$,

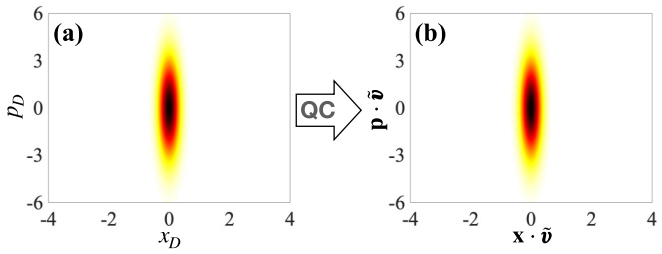

FIG. 4. Basic illustration of QC operation: it transforms the squeezed-vacuum state in the input mode D, from being squeezed in the quadrature plane x_D-p_D (a), to being squeezed in the quadrature plane $\boldsymbol{x}\cdot\tilde{\boldsymbol{v}}=\sum_{j=1}^{d}x_j\tilde{v}_j$ and $\boldsymbol{p}\cdot\tilde{\boldsymbol{v}}=\sum_{j=1}^{d}p_j\tilde{v}_j$ (b). Here $r=1$.

we get $u_j=(\boldsymbol{U}_{\rm QC})_{Dj}=\boldsymbol{W}_{Dj}=w_j=e^{i(\varphi/2-\phi_j)}\tilde{v}_j$. This gives back the optimal QC parameters $\tilde{u}_j=\tilde{v}_j$ [compare Eq. (13) and the expression of $\tilde{v}_j$ given above] and implies $\delta_j=\varphi/2-\phi_j$ $(+\pi)$, where the extra $+\pi$ has to be included if $\tilde{v}_j$ is negative, thus recovering the optimal phase-matching condition $\sin\chi_j=\sin(\phi_j-\varphi/2+\delta_j)=0$ discussed in Sec. III A.

The situation is quite different for the separable strategy. In this case, under a Holstein-Primakoff transformation analogous to the one considered above, we find

$$\begin{aligned}\Delta^2(\boldsymbol{v}\cdot\boldsymbol{\theta})_{\rm sm}&=\sum_{j=1}^{d}\Delta^2\left[\frac{(\hat{J}_x)_j}{\langle(\hat{J}_z)_j\rangle}v_j\right]_{|\alpha'_j\rangle\otimes|\xi'_j\rangle}\\&\approx 2\sum_{j=1}^{d}\Delta^2\left[\hat{x}_j\frac{v_j}{|\alpha'_j|}\right]_{|\xi'_j\rangle}\\&=2\sum_{j=1}^{d}\frac{v_j^2}{|\alpha'_j|^2}\Delta^2[\hat{x}_j]_{|\xi'_j\rangle}.\end{aligned}\tag{34}$$

The sensitivity breaks up into the sum of d quadrature variances, with $\Delta^2[\hat{x}_j]_{|\xi'_j\rangle}=e^{-2r'_j}/2$. Upon optimizing Eq. (34) over the d squeezing parameters r'_j with $r'_j\gg 1$, for a given $\boldsymbol{v}$, it is possible to recover Eq. (27). Equation (34) shows that the estimation of an arbitrary $\boldsymbol{v}\cdot\boldsymbol{\theta}$ with a sensitivity overcoming the standard quantum limit (set by vacuum fluctuations) requires, in general, having d squeezed-vacuum states. On the other hand, the entangled strategy requires only the QC to optimally distribute a single squeezed vacuum state among the d MZIs.

B. Comparison between optimal entangled and separable strategies under different constraints

In the following we study the gain factors $\mathcal{G}_C(\boldsymbol{v})$ and $\mathcal{G}^{\rm Q}_C(\boldsymbol{v})$, defined as the ratio between the estimation uncertainties of the separable and the entangled strategy, evaluated using the method of moments and QCRB, respectively, and optimized under a common constraint C on resources. Different cases are considered.

1. C_1: *Same average total number of particles and same total squeezed-vacuum intensities*

Under the constraint $\{C_1:\bar{n}'_T=\bar{n}_T,\bar{n}'_s=\bar{n}_s\}$, we write

$$\mathcal{G}^{\rm Q}_{C_1}(\boldsymbol{v},\bar{n}_s,\bar{n}_T)=\frac{\gamma_{\rm sQ}(\boldsymbol{v},\bar{n}_s,\bar{n}_T)}{\gamma_{\rm eQ}(\boldsymbol{v},\bar{n}_s,\bar{n}_T)}.\tag{35}$$

For $\bar{n}_T\gg 2\bar{n}_s$, the optimized QCRB in the entangled case is given in Eq. (23). In the same limit, and for $r'_j\gg 1$ $(j=1,\ldots,d)$, the optimized QCRB in the separable case is $\gamma_{\rm sQ}=e^{-2r}/\bar{n}_T(\sum_{j=1}^{d}|v_j|^{2/3})^3$; see Sec. IV C. We thus find

$$\mathcal{G}^{\rm Q}_{C_1}(\boldsymbol{v})=\left(\sum_{j=1}^{d}|v_j|^{2/3}\right)^3\left(\sum_{j=1}^{d}|v_j|\right)^{-2},\tag{36}$$

which, in particular, is independent of $\bar{n}_s$ and $\bar{n}_T$. It is possible to prove that

$$1=\mathcal{G}^{\rm Q}_{C_1}(\boldsymbol{v}_{\rm sing})\leqslant\mathcal{G}^{\rm Q}_{C_1}(\boldsymbol{v})\leqslant\mathcal{G}^{\rm Q}_{C_1}(\boldsymbol{v}_{\rm av})=d.\tag{37}$$

The left-hand-side inequality follows from monotonicity of the p-norm and the triangular inequality [89]. The right-hand side is a consequence of the reverse Hölder's inequality [90]. The highest gain, in the considered regime, is a factor d, achieved for the estimation of $\boldsymbol{v}_{\rm av}\cdot\boldsymbol{\theta}$. Clearly, the entangled and the separable strategies reach the same optimal estimation of a single parameter (namely, $\boldsymbol{v}_{\rm sing}\cdot\boldsymbol{\theta}$).

Let us now turn to the gain obtained with the method of moments,

$$\mathcal{G}_{C_1}(\boldsymbol{v},\bar{n}_s,\bar{n}_T)=\frac{\gamma_{\rm sm}(\boldsymbol{v},\bar{n}_s,\bar{n}_T)}{\gamma_{\rm em}(\boldsymbol{v},\bar{n}_s,\bar{n}_T)},\tag{38}$$

given by the ratio between Eq. (25) and Eq. (11). We find that $\mathcal{G}_{C_1}(\boldsymbol{v},\bar{n}_s,\bar{n}_T)$ recovers Eq. (36) for $\bar{n}_T\gg(e^{2r}+1)\bar{n}_s$ and $r'_j\gg 1$ for all $j=1,\ldots,d$. A plot of $\mathcal{G}_{C_1}=\mathcal{G}^{\rm Q}_{C_1}$, in this regime, is shown in Fig. 5(a) for $d=2$ and in Fig. 5(b) for $d=3$. We clearly observe the gain factor d for $\boldsymbol{v}=\boldsymbol{v}_{\rm av}$.

In the rest of this section, we focus on the optimal case $\boldsymbol{v}=\boldsymbol{v}_{\rm av}$ and explore a wider parameter regime than the one considered above. In Fig. 6(a) we plot the numerical evaluation of $\mathcal{G}_{C_1}(\boldsymbol{v}_{\rm av},\bar{n}_s,\bar{n}_T)$ as a function of $\bar{n}_T/\bar{n}_s$ and for $d=2$ (dots). The solid line is

$$\mathcal{G}_{C_1}(\boldsymbol{v}_{\rm av},\bar{n}_s,\bar{n}_T)=\frac{\bar{n}_T e^{-2r'}+\bar{n}_s}{\bar{n}_T e^{-2r}+\bar{n}_s},\tag{39}$$

where $r'=\operatorname{arcsinh}\sqrt{\bar{n}_s/d}$ (note that $\bar{n}_s=d\sinh^2 r'=\sinh^2 r$). This equation is the ratio between Eq. (16), valid for $\bar{n}_T\gg 2\bar{n}_s$, and

$$\gamma_{\rm sm}(\boldsymbol{v}_{\rm av},\bar{n}_s,\bar{n}_T)=\frac{e^{-2r'}}{\bar{n}'_T}+\frac{\bar{n}'_s}{\bar{n}'^2_T},\tag{40}$$

with $\bar{n}'_T=\bar{n}_T$ and $\bar{n}'_s=\bar{n}_s$. Equation (40) is derived from Eq. (9) by assuming an even splitting of resources, $|\alpha'_j|^2=\bar{n}_c$ and $(\bar{n}'_s)_j=\bar{n}_s/d$ for $j=1,\ldots,d$, as predicted by Eq. (28).

Let us first analyze the behavior of the gain in the limit $\bar{n}_T\gg e^{2r}\bar{n}_s$, which also implies $\bar{n}_T\gg e^{2r'}\bar{n}_s$ since $r\geqslant r'$. Equation (39) simplifies to

$$\mathcal{G}_{C_1}(\boldsymbol{v}_{\rm av},\bar{n}_s,\bar{n}_T)\approx e^{2(r-r')}=\begin{cases}d & \text{for } \bar{n}_s\gg d\\ e^{2r} & \text{for } \bar{n}_s\ll d.\end{cases}\tag{41}$$

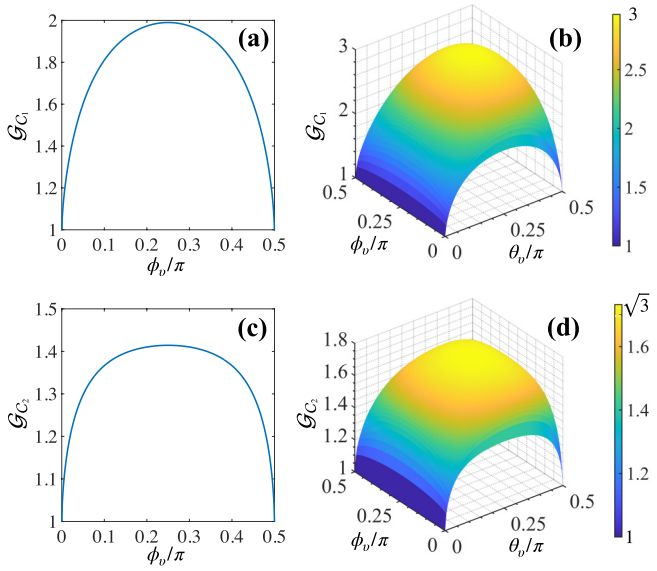

FIG. 5. Sensitivity gain of the entangled over the separable strategy for $d = 2$ (left column) and $d = 3$ (right column). Panels (a) and (b) plot $\mathcal{G}_{C_1}(\boldsymbol{v}, \bar{n}_s, \bar{n}_T)$, Eq. (38). Notice that in the regime of parameters of panels (a) and (b), we have $\mathcal{G}_{C_1} = \mathcal{G}^{\mathrm{Q}}_{C_1}$, with $\mathcal{G}^{\mathrm{Q}}_{C_1}$ given in Eq. (36). Panels (c) and (d) show the result of the numerical evaluation of $\mathcal{G}_{C_2}(\boldsymbol{v}, \bar{n}_T)$, Eq. (43). The vector $\boldsymbol{v}$ is expressed as in polar and spherical coordinates, respectively, as in Fig. 2. In all panels $\bar{n}_T = \bar{n}'_T = 10^8$. In panels (a) and (b), $\bar{n}_s = \bar{n}'_s = 10^2$.

The case $\bar{n}_s \gg d$ is obtained by recognizing that, in this limit, $\bar{n}_s \approx e^{2r}/4 \approx d e^{2r'}/4$. In particular, we recover the gain factor d discussed previously. In the opposite case, $\bar{n}_s \ll d$, and, in particular, taking the limit $d \to \infty$, the even splitting of squeezed photons among the modes, namely, $r'_j = r' = \mathrm{arcsinh}\sqrt{\bar{n}_s/d}$ for all $j = 1, \ldots, d$, implies $r'_j \to 0$. The separable sensing scheme thus reduces to d MZIs fed with coherent state in one port and (approximately) the vacuum in the other port. This is characterized by a SN sensitivity, $\gamma_{\mathrm{sm}}(\boldsymbol{v}_{\mathrm{av}}, \bar{n}_s, \bar{n}_T) \to 1/(d\bar{n}_c) = 1/\bar{n}_T$, as seen in Eq. (40). It is possible to show that the same sensitivity is also achieved for the optimized quantum Cramér-Rao bound. The situation is different for the entangled scheme. In this case, r remains finite in the limit $d \to \infty$ and the entangled strategy still achieves a sub-SN sensitivity; see Eq. (16). Surprisingly, a finite gain is obtained when a single squeezed-vacuum state is mixed, by the QC, with a large number $(d-1)$ of vacuum states $|0\rangle$. The discussion reported in Sec. V A explains the physical reason for the finite gain: the QC is able to turn the squeezed state in a single input port to a squeezing in the opportune combination of quadrature modes, regardless of the number of such modes (thus also in the limit $d \to \infty$).

The evaluation of the gain $\mathcal{G}_{C_1}(\boldsymbol{v}_{\mathrm{av}}, \bar{n}_s, \bar{n}_T)$ for relatively small values of $\bar{n}_T/\bar{n}_s$ is more difficult. In this case, Eq. (40) breaks down, and, although Eq. (39) predicts $\mathcal{G}_{C_1}(\boldsymbol{v}_{\mathrm{av}}, \bar{n}_s, \bar{n}_T) = 1$, we observe smaller values numerically [see, for example, Fig. 6(a)]. In particular, the numerical study gives a bifurcation of optimal resources in the separable strategy [see the inset of Fig. 6(a)]. In this case, $\Delta^2(\boldsymbol{v}_{\mathrm{av}} \cdot \boldsymbol{\theta})_{\mathrm{sm}}$ is minimized by an uneven splitting of resources such that one phase is estimated much better than the other. This is due

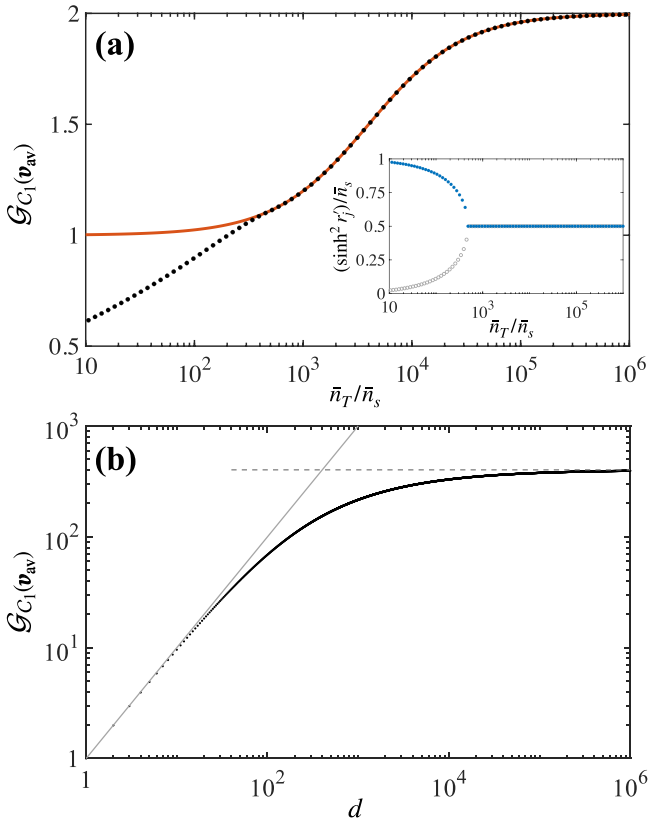

FIG. 6. (a) Gain $\mathcal{G}_{C_1}(\boldsymbol{v}_{\mathrm{av}}, \bar{n}_s, \bar{n}_T)$ as a function of $\bar{n}_T/\bar{n}_s$, with fixed $\bar{n}_s = 10^3$ and for $d = 2$. The numerical evaluation (dots) is compared with Eq. (39) (solid line). The inset shows the average number of squeezed photons to be injected into each of the two MZIs in order to optimize the sensitivity of the separable strategy: $(\sinh^2 r'_j)/\bar{n}_s$ for $j = 1$ (blue dots) and $j = 2$ (gray circles). For low values of $\bar{n}_T/\bar{n}_s$, a bifurcation appears, meaning that one interferometer gets more squeezed photons than the other. (b) $\mathcal{G}_{C_1}(\boldsymbol{v}_{\mathrm{av}}, \bar{n}_s, \bar{n}_T)$ plotted as a function of d (dots), Eq. (39), with $\bar{n}_c = 10^8$ and $\bar{n}_s = 10^2$. The solid line is $\mathcal{G}_{C_1}(\boldsymbol{v}_{\mathrm{av}}, \bar{n}_s, \bar{n}_T) = d$, which is expected for $d \ll \bar{n}_s$; the dashed line is $\mathcal{G}_{C_1}(\boldsymbol{v}_{\mathrm{av}}, \bar{n}_s, \bar{n}_T) = e^{2r}$, for $d \gg \bar{n}_s$; see Eq. (41).

to the existence of an optimal sensitivity point for the single MZI when $\bar{n}_s \approx \sqrt{\bar{n}_T}/2$. For low values of the ratio $\bar{n}_T/\bar{n}_s$, an even distribution of input resources would result in a low number of coherent photons per interferometer, keeping each MZI away from its optimal working point. A nonsymmetric configuration is therefore favorable in this regime.

2. C_2: Same average total number of particles

With the constraint $\{C_2 : \bar{n}'_T = \bar{n}_T\}$ we impose only the same total average number of particles. We optimize the sensitivity of the entangled and of the separable strategies over $\bar{n}_s$ and $\bar{n}'_s$, respectively. We thus define

$$\mathcal{G}^{\mathrm{Q}}_{C_2}(\boldsymbol{v}, \bar{n}_T) = \frac{\min_{\bar{n}'_s} \gamma_{\mathrm{sQ}}(\boldsymbol{v}, \bar{n}'_s, \bar{n}_T)}{\min_{\bar{n}_s} \gamma_{\mathrm{eQ}}(\boldsymbol{v}, \bar{n}_s, \bar{n}_T)} \tag{42}$$

and

$$\mathcal{G}_{C_2}(\boldsymbol{v}, \bar{n}_T) = \frac{\min_{\bar{n}'_s} \gamma_{\mathrm{sm}}(\boldsymbol{v}, \bar{n}'_s, \bar{n}_T)}{\min_{\bar{n}_s} \gamma_{\mathrm{em}}(\boldsymbol{v}, \bar{n}_s, \bar{n}_T)}. \tag{43}$$

The numerical evaluation of Eq. (43) is shown in Fig. 5(c) for $d = 2$ and Fig. 5(d) for $d = 3$. We see that $\mathcal{G}_{C_2}(\boldsymbol{v}, \bar{n}_T) \geqslant 1$ for all $\boldsymbol{v}$, with the maximum gain achieved for $\boldsymbol{v} = \boldsymbol{v}_{\rm av}$. Similar results are also obtained for $\mathcal{G}^{\rm Q}_{C_2}(\boldsymbol{v}, \bar{n}_T)$.

In the specific case $\boldsymbol{v} = \boldsymbol{v}_{\rm av}$, we find

$$\mathcal{G}^{\rm Q}_{C_2}(\boldsymbol{v}_{\rm av}, \bar{n}_T) = d. \tag{44}$$

This follows from $\min_{\bar{n}_s} \gamma_{\rm eQ}(\boldsymbol{v}_{\rm av}, \bar{n}_s, \bar{n}_T) = \bar{n}_T^{-2}$ for $\bar{n}_s \approx \bar{n}_T/2$, and $\min_{\bar{n}'_s} \gamma_{\rm sQ}(\boldsymbol{v}_{\rm av}, \bar{n}'_s, \bar{n}_T) = 1/d(\bar{n}_T/d)^{-2} = d/\bar{n}_T^2$ for $\bar{n}'_s \approx \bar{n}_T/2$. It should be noticed that Eq. (44) holds for $\bar{n}'_s = \bar{n}_s$. The entangled strategy uses a single squeezed-vacuum state of $\bar{n}_s$ particles, while the separable strategy uses d squeezed-vacuum states, each with $\bar{n}_s/d$ photons. The gain for the method of moments is instead

$$\mathcal{G}_{C_2}(\boldsymbol{v}_{\rm av}, \bar{n}_T) = \sqrt{d}. \tag{45}$$

This is obtained by optimizing Eqs. (16) and (40), over $\bar{n}_s$ and $\bar{n}'_s$, respectively. This gives $\min_{\bar{n}_s} \gamma_{\rm em}(\boldsymbol{v}_{\rm av}, \bar{n}_s, \bar{n}_T) = \bar{n}_T^{-3/2}$ for $\bar{n}_s \approx \sqrt{\bar{n}_T}/2$, and $\min_{\bar{n}'_s} \gamma_{\rm sm}(\boldsymbol{v}_{\rm av}, \bar{n}'_s, \bar{n}_T) = 1/d(\bar{n}_T/d)^{-3/2} = \sqrt{d}/\bar{n}_T^{3/2}$, for $\bar{n}'_s \approx d(\sqrt{\bar{n}_T/d})/2$, respectively. A maximum gain $\sqrt{2}$ and $\sqrt{3}$ is observed in Figs. 5(c) and 5(d), for $d = 2$ and $d = 3$, respectively.

3. C_3: Same average total number of particles and equal squeezed-vacuum intensities for all modes

Here we impose the constraint $\{C_3 : \bar{n}'_T = \bar{n}_T, r'_j = r, \text{for } j = 1, \ldots, d\}$: namely, the separable strategy uses d copies of the squeezed-vacuum state $|\xi\rangle$ used in the entangled strategy. We write

$$\mathcal{G}^{\rm Q}_{C_3}(\boldsymbol{v}, \bar{n}_s, \bar{n}_T) = \frac{\min_{|\alpha'_1|^2, \ldots, |\alpha'_d|^2} \Delta^2(\boldsymbol{v}\cdot\boldsymbol{\theta})_{\rm sQ}}{\min_{|\alpha_1|^2, \ldots, |\alpha_d|^2, \hat{U}_{\rm QC}} \Delta^2(\boldsymbol{v}\cdot\boldsymbol{\theta})_{\rm eQ}}. \tag{46}$$

Notice that the condition $r'_j = r$ implies $\bar{n}'_s = d\bar{n}_s$: the total number of squeezed photons used by the separable strategy is d times larger than the one used by the entangled strategy. For $\bar{n}_T \gg 2\bar{n}_s$, we find

$$\mathcal{G}^{\rm Q}_{C_3}(\boldsymbol{v}, \bar{n}_s, \bar{n}_T) = 1. \tag{47}$$

Equation (47) is derived in Appendix A 2. Although there is no effective gain in this case, it is still interesting that the entangled strategy using a *single* squeezed-vacuum state achieves the same performance as the sequential strategy using d squeezed states with the same squeezing parameter.

Let us now focus on the gain obtained from the method of moments sensitivity,

$$\mathcal{G}_{C_3}(\boldsymbol{v}, \bar{n}_s, \bar{n}_T) = \frac{\min_{|\alpha'_1|^2, \ldots, |\alpha'_d|^2} \Delta^2(\boldsymbol{v}\cdot\boldsymbol{\theta})_{\rm sm}}{\min_{|\alpha_1|^2, \ldots, |\alpha_d|^2, \hat{U}_{\rm QC}} \Delta^2(\boldsymbol{v}\cdot\boldsymbol{\theta})_{\rm em}}, \tag{48}$$

and let us consider the case $\boldsymbol{v} = \boldsymbol{v}_{\rm av}$. In Fig. 7 we show $\mathcal{G}_{C_3}(\boldsymbol{v}_{\rm av}, \bar{n}_s, \bar{n}_T)$ as a function of $\bar{n}_T/\bar{n}_s$. The numerical optimization (dots) is compared with

$$\mathcal{G}_{C_3}(\boldsymbol{v}_{\rm av}, \bar{n}_s, \bar{n}_T) = \frac{\bar{n}_T e^{-2r} + d\bar{n}_s}{\bar{n}_T e^{-2r} + \bar{n}_s} \tag{49}$$

shown as a solid line. This equation is derived by taking the ratio between Eq. (40) and Eq. (16) with $\bar{n}'_T = \bar{n}_T$ and $\bar{n}'_s = d\bar{n}_s$. In the regime $\bar{n}_T \gg d e^{2r}\bar{n}_s$, we find $\mathcal{G}_{C_3}(\boldsymbol{v}_{\rm av}, \bar{n}_s, \bar{n}_T) = 1$.

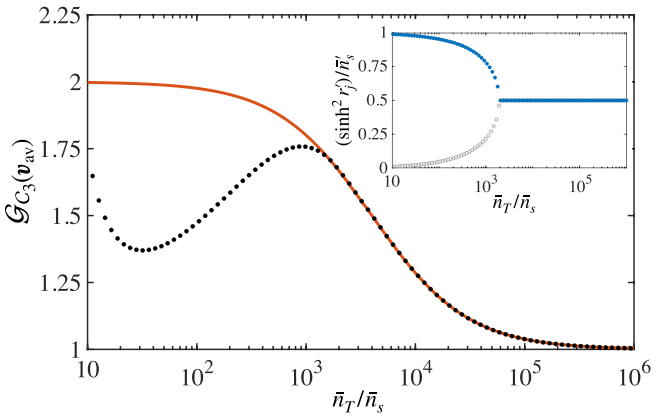

FIG. 7. Gain factor $\mathcal{G}_{C_3}(\boldsymbol{v}_{\rm av}, \bar{n}_s, \bar{n}_T)$ as a function of $\bar{n}_T/\bar{n}_s$, with $\bar{n}_s = 10^3$ and for $d = 2$. The numerical evaluation of the gain Eq. (48) (dots) is compared with Eq. (49) (solid line). The inset shows the average number of squeezed photons to be injected into each MZI in order to optimize the sensitivity of the separable strategy, $(\sinh^2 r'_j)/\bar{n}'_s$ for $j = 1$ (blue dots) and $j = 2$ (gray circles): a bifurcation appears for low values of $\bar{n}_T/\bar{n}_s$.

Equation (49) predicts an increase of the gain when decreasing $\bar{n}_T/\bar{n}_s$ and $\mathcal{G}_{C_3}(\boldsymbol{v}_{\rm av}, \bar{n}_s, \bar{n}_T) = d$ for low enough values of the ratio. As shown in Fig. 7, this regime is characterized, however, by a bifurcation of optimal parameters for the separable case (see inset), and the assumption leading to Eq. (49), namely, the even distribution of resources among the d MZIs for the separable case, breaks down.

C. Impact of noise and imperfections

So far we have focused on the sensitivity gain obtained in the noiseless case. In the following we analyze different possible sources of imperfections. For simplicity, we study the estimation of the average phase $\boldsymbol{v}_{\rm av}\cdot\boldsymbol{\theta}$ taking $|\alpha_j|^2 = \bar{n}_c$, $j = 1, \ldots, d$. We also consider the optimal working point $\theta_j = \pi/2$. Under these conditions, the sensitivity for the entangled strategy reads

$$\begin{aligned}\Delta^2(\boldsymbol{v}_{\rm av}\cdot\boldsymbol{\theta})_{\rm em} = {} & \frac{(e^{2r}-1)\bar{n}_c}{d^2}\left(\sum_{j=1}^{d}\frac{\tilde{u}_j \sin\chi_j}{\bar{n}_c - \tilde{u}_j^2\bar{n}_s}\right)^2 \\ & - \frac{(1-e^{-2r})\bar{n}_c}{d^2}\left(\sum_{j=1}^{d}\frac{\tilde{u}_j \cos\chi_j}{\bar{n}_c - \tilde{u}_j^2\bar{n}_s}\right)^2 \\ & + \frac{1}{d^2}\sum_{j=1}^{d}\frac{\bar{n}_c + \tilde{u}_j^2\bar{n}_s}{\bar{n}_c - \tilde{u}_j^2\bar{n}_s}.\end{aligned} \tag{50}$$

1. Imperfect choice of parameters

In this section we restrict to the case $d = 3$. We assume the relative phases χ_j distributed on a circle around the optimal point $\chi_j = 0$ with

$$p_\sigma(\chi_j) = \frac{1}{2\pi I_0(1/\sigma^2)} \exp\left[\cos\left(\chi_j\right)/\sigma_\chi^2\right], \tag{51}$$

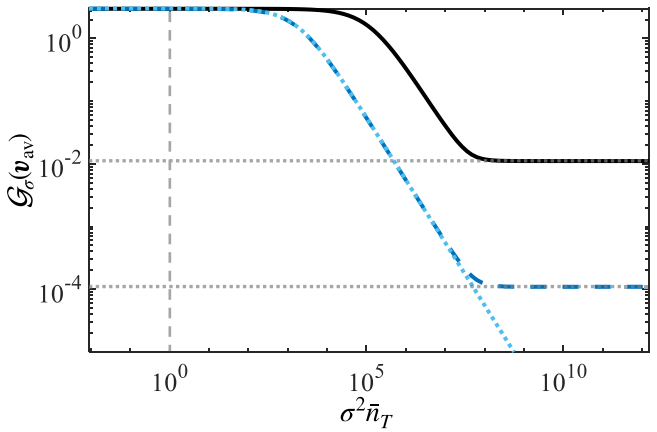

FIG. 8. Average gain Eq. (53) as a function of the parameters σ_χ^2 (dashed blue line) and $\sigma_{\tilde{u}}^2$ (solid black line) normalized to $1/\bar{n}_T$. The numeric is compared with analytical predictions: the dotted blue curve is Eq. (54); the two dotted horizontal lines are the limiting values of the gain, for $\sigma^2 \to \infty$ (see main text). The dashed vertical line corresponds to $\sigma^2 = 1/\bar{n}_T$. Here $\bar{n}_T = 10^8$, $\bar{n}_s = 100$ and averaging is done under 10^6 repetitions.

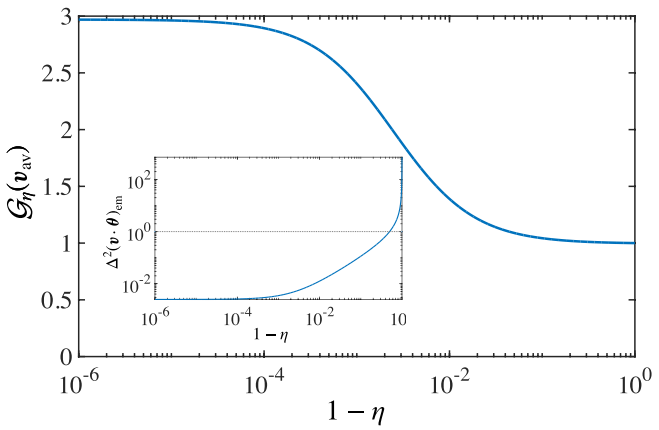

FIG. 9. Gain Eq. (56) as a function of the parameter $1-\eta$ corresponding to the probability of losses at each detector. The inset shows the sensitivity Eq. (55) as a function of $1-\eta$. Here $d = 3$, $\bar{n}_T = 10^8$, $\bar{n}_s = 100$, and we assume optimal parameters.

where $I_0(1/\sigma^2)$ is the modified Bessel function of the first kind of order 0. Equation (51) models imperfections in the phase locking. Similarly, we take the vector $\tilde{\boldsymbol{u}} = (\tilde{u}_1, \tilde{u}_2, \tilde{u}_3)$ (defining the configuration of the QC) distributed on the sphere according to the probability density function

$$p_\sigma(\tilde{\boldsymbol{u}}) = \frac{k}{4\pi \sinh k} \exp\left[\tilde{\boldsymbol{u}}_{\rm opt}^T \tilde{\boldsymbol{u}}/\sigma_{\tilde{u}}^2\right], \tag{52}$$

where $\tilde{\boldsymbol{u}}_{\rm opt}$ is the optimal direction [$\tilde{\boldsymbol{u}}_{\rm opt} = (1,1,1)/\sqrt{3}$ in our case]. This corresponds to an imperfection in the QC (still considered to be lossless). The analysis of a nonunitary QC due to losses and decoherence is more difficult, and it is beyond the scope of this paper.

In Fig. 8 we show the results of a numerical analysis. We plot

$$\mathcal{G}_\sigma(\boldsymbol{v}_{\rm av}, \bar{n}_s, \bar{n}_T) = \frac{\Delta^2(\boldsymbol{v}_{\rm av}\cdot\boldsymbol{\theta})_{\rm sm}}{\langle \Delta^2(\boldsymbol{v}_{\rm av}\cdot\boldsymbol{\theta})_{\rm em}\rangle_\sigma} \tag{53}$$

as a function of σ^2. Two cases are considered: (1) $\sigma = \sigma_\chi$ and $\sigma_{\tilde{u}} = 0$ (dashed blue line) and (2) $\sigma = \sigma_{\tilde{u}}$ and $\sigma_\chi = 0$ (solid black line). In the evaluation of Eq. (53), the constraint C_1 is considered; see Sec. V B 1.

It is worth examining the first case in more detail. When $\sigma_\chi \ll 1$, Eq. (51) can be well approximated by a Gaussian of width σ_χ. We thus have $\langle \sin\chi_j\rangle_{\sigma_\chi} = 0$ by simple symmetry arguments, and, to the first order in σ_χ^2, $\langle\cos\chi_j\rangle_{\sigma_\chi} \simeq 1 - \sigma_\chi^2/2$, $\langle\sin^2\chi_j\rangle_{\sigma_\chi} \simeq \langle\chi_j^2\rangle \sim \sigma_\chi^2$ and $\langle\cos^2\chi_j\rangle_{\sigma_\chi} \sim 1 - \sigma_\chi^2$. In the regime $\bar{n}_T \gg (e^{2r}+1)\bar{n}_s, \bar{n}_s/d \gg 1$, we find

$$\mathcal{G}_{\sigma_\chi}(\boldsymbol{v}_{\rm av}, \bar{n}_s, \bar{n}_T) \approx d\left(1 + \frac{e^{4r}}{d}\sigma_\chi^2\right)^{-1}, \tag{54}$$

recovering the gain d for $\sigma_\chi^2 \to 0$. Equation (54) can also be used to derive the value of the gain corresponding to $\sigma_\chi^2 \sim 1/\bar{n}_T$, with $\bar{n}_T \gg 1$. This is a relevant check as controlling parameter fluctuations with precision at the shot-noise limit is a task achievable in most laboratories. If $\sigma_\chi^2 \ll de^{-4r}$, Eq. (54) can be linearized and the relative decrease in gain approximated as $\Delta\mathcal{G}_{\sigma_\chi}(\boldsymbol{v}_{\rm av}, \bar{n}_s, \bar{n}_T)/d \approx e^{4r}\sigma_\chi^2/d \ll 1$. This is precisely the situation we get for $\sigma_\chi^2 \sim 1/\bar{n}_T$ and in the regime specified above. The gain of our scheme is thus proven to be robust against reasonably small fluctuations around its optimal configuration, in a relevant regime of parameters.

In the opposite limit, $\sigma_\chi^2 \to \infty$ or $\sigma_{\tilde{u}}^2 \to \infty$, the probability distributions (51) and (52) become uniform. A simple calculation shows that $\lim_{\sigma_\chi\to\infty}\mathcal{G}_{\sigma_\chi}(\boldsymbol{v}_{\rm av}, \bar{n}_s, \bar{n}_T) = d^2e^{-2r}/(\cosh r + d - 1)$ and $\lim_{\sigma_{\tilde{u}}\to\infty}\mathcal{G}_{\sigma_{\tilde{u}}}(\boldsymbol{v}_{\rm av}, \bar{n}_s, \bar{n}_T) = d^2e^{-2r}/(e^{-2r} + d - 1)$. Notice that $\lim_{\sigma_\chi\to\infty}\mathcal{G}_{\sigma_\chi}(\boldsymbol{v}_{\rm av}, \bar{n}_s, \bar{n}_T) \leqslant \lim_{\sigma_{\tilde{u}}\to\infty}\mathcal{G}_{\sigma_{\tilde{u}}}(\boldsymbol{v}_{\rm av}, \bar{n}_s, \bar{n}_T) \leqslant d$. These results, together with a direct comparison between the two main curves of the figure, prove that our scheme is generally more robust against fluctuations in the QC parameters than in relative-phase fluctuations between the input states. Also, as one could expect, large fluctuations imply an exponential suppression of the gain achieved by the entangled strategy with the squeezing parameter r.

2. *Particle losses and finite detection efficiency*

Photon losses in a given output mode or, equivalently, finite detection efficiency, can be described through a beam splitter which couples that mode with a fictitious vacuum mode. Taking, for simplicity, the same loss coefficient η ($\eta = 1$ in the ideal case) for all output modes, we obtain

$$\begin{aligned}[\Delta^2(\boldsymbol{v}\cdot\boldsymbol{\theta})_{\rm em}]_\eta =& \Delta^2(\boldsymbol{v}\cdot\boldsymbol{\theta})_{\rm em} \\ &+ \frac{1-\eta}{\eta}\sum_{j=1}^{d}\frac{|\alpha_j|^2 + \tilde{u}_j^2\bar{n}_s}{\left(|\alpha_j|^2 - \tilde{u}_j^2\bar{n}_s\right)^2} \\ &\times (1 + \cot^2\theta_j)v_j^2,\end{aligned} \tag{55}$$

as derived in Appendix A 5, where $\Delta^2(\boldsymbol{v}\cdot\boldsymbol{\theta})_{\rm em}$ is given in Eq. (A44) of Appendix A 1 and corresponds to the ideal case

($\eta = 1$). In Fig. 9 we plot the sensitivity gain

$$\mathcal{G}_\eta(\boldsymbol{v}_{\rm av}, \bar{n}_s, \bar{n}_T) = \frac{[\Delta^2(\boldsymbol{v}_{\rm av}\cdot\boldsymbol{\theta})_{\rm sm}]_\eta}{[\Delta^2(\boldsymbol{v}_{\rm av}\cdot\boldsymbol{\theta})_{\rm em}]_\eta} \tag{56}$$

as a function of $1-\eta$. Here the entangled and separable strategies are compared for the same number of losses and applying the constraint C_1; see Sec. V B 1. The sensitivity of the separable case is derived by taking $d = 1$ in Eq. (55) and then making use of Eq. (2). Overall, we find a gain larger than one for any amount losses, recovering the factor d for $\eta \to 1$. In the opposite limit, $\eta \to 0$, the uncertainty of both the entangled and the separable strategies diverges (see inset of Fig. 9) such that $\mathcal{G}_\eta(\boldsymbol{v}_{\rm av}, \bar{n}_s, \bar{n}_T) \to 1$.

VI. OPTIMAL LINEAR COMBINATION OF PHASES

In the previous section, we have discussed the optimal configuration of the sensor network of Fig. 1(a) that minimizes the uncertainty $\Delta^2(\boldsymbol{v}\cdot\boldsymbol{\theta})$ for the estimation of a given linear combination of phases $\boldsymbol{v}\cdot\boldsymbol{\theta}$. Here we consider the opposite problem. For a specific configuration of the sensor network, namely, a specific QC transformation $\boldsymbol{U}_{\rm QC}^\dagger$, coherent state intensities, and squeezing parameter, we want to find the optimal linear combination of phases $\boldsymbol{v}\cdot\boldsymbol{\theta}$ that can estimated with the smallest possible uncertainty.

A. Fisher spectrum and squeezing spectrum

Finding the optimal vector $\boldsymbol{v} \in \mathbb{R}^d$ that minimizes Eq. (1) and/or Eq. (3) is solved by calculating the spectrum of the matrices $\boldsymbol{\mathcal{F}}_{\rm Q}$ and $\boldsymbol{\mathcal{M}}$, which we indicate as Fisher and squeezing spectrum, respectively. These spectra contain useful information regarding the multiparameter problem, in general. We have

$$\min_{\boldsymbol{v}\in\mathbb{R}^d} \Delta^2(\boldsymbol{v}\cdot\boldsymbol{\theta})_{\rm em} = \frac{1}{\mu_{\max} d}, \tag{57}$$

where $\mu_{\max}$ is the largest eigenvalue of $\boldsymbol{\mathcal{M}}$. The corresponding optimal eigenvector $\boldsymbol{v}_{\mu_{\max}}$ gives the linear combination of parameters $\boldsymbol{v}_{\mu_{\max}}\cdot\boldsymbol{\theta}$ that can be estimated with the smallest possible uncertainty when using the specific method of moments considered (namely, based on the chosen measurement observables $\hat{X}_j$, probe state, and phase encoding transformation). Following the inequality $\Delta^2(\boldsymbol{v}\cdot\boldsymbol{\theta})_{\rm eQ} \leqslant \Delta^2(\boldsymbol{v}\cdot\boldsymbol{\theta})_{\rm em}$, we have $f_{\max} \geqslant \mu_{\max}$, where $f_{\max}$ is the largest eigenvalue of the QFIM and satisfies

$$\min_{\boldsymbol{v}\in\mathbb{R}^d} \Delta^2(\boldsymbol{v}\cdot\boldsymbol{\theta})_{\rm eQ} = \frac{1}{f_{\max} d}. \tag{58}$$

The corresponding optimal eigenvector $\boldsymbol{v}_{f_{\max}}$ (in general, $\boldsymbol{v}_{f_{\max}} \neq \boldsymbol{v}_{\mu_{\max}}$) gives the linear combinations of parameters, $\boldsymbol{v}_{f_{\max}}\cdot\boldsymbol{\theta}$, that can be estimated with the highest possible sensitivity (when optimized over all generalized output measurements and all possible estimation strategies) for the given probe state and phase encoding transformation. The demonstration of Eqs. (57) and (58) is reported in Appendix A 4. Furthermore, a degeneracy (e.g., in the squeezing spectrum) reveals independent linear combinations of parameters that can be estimated with the same sensitivity. Specifically, if d_μ is the degeneracy of the eigenvalue μ of $\boldsymbol{\mathcal{M}}$, then the sensitivity $\Delta^2(\boldsymbol{v}\cdot\boldsymbol{\theta})_{\rm em} = 1/(\mu d)$ is the same for any $\boldsymbol{v}$ given by a linear combination of the d_μ orthonormal eigenvectors $\boldsymbol{v}_\mu^{(1)}, \ldots, \boldsymbol{v}_\mu^{(d_\mu)}$. In particular, $\boldsymbol{\mathcal{M}}^{-1}$ ($\boldsymbol{\mathcal{F}}_{\rm Q}^{-1}$) is defined on the subspace of $\mathbb{R}^d$ generated by a basis of eigenvectors of $\boldsymbol{\mathcal{M}}$ ($\boldsymbol{\mathcal{F}}_{\rm Q}$) corresponding to finite eigenvalues.

B. Random choice of quantum circuit

Here we consider random choices of the QC and find the corresponding optimal $\Delta^2(\boldsymbol{v}\cdot\boldsymbol{\theta})_{\rm em}$. To be more explicit, we generate random unitary QC matrices $\boldsymbol{U}_{\rm QC}^\dagger$ (with uniform Haar measure) and calculate the largest eigenvalue $\mu_{\max}$ of $\boldsymbol{\mathcal{M}}$ (see Appendix A 1 for the analytical expression of this matrix). Furthermore, without loss of generality, we take the same number of photons in each coherent state, namely, $|\alpha_j|^2 = \bar{n}_c = (\bar{n}_T - \bar{n}_s)/d$, for all $j = 1, \ldots, d$.

Figure 10 summarizes our findings, while different analytical limits are discussed below. The figure shows $\mathcal{E}_{\rm QC}[1/(\mu_{\max} d)]$ (green dots), where $\mathcal{E}_{\rm QC}[\cdots]$ indicates statistical averaging. For comparison, we also consider $\mathcal{E}_{\rm QC}[1/(f_{\max} d)]$ (red triangles). An analytical upper bound to Eq. (57),

$$\min_{\boldsymbol{v}\in\mathbb{R}^d} \Delta^2(\boldsymbol{v}\cdot\boldsymbol{\theta})_{\rm em} \leqslant \frac{\tilde{\boldsymbol{u}}^T \boldsymbol{\mathcal{M}}(\tilde{\boldsymbol{u}})^{-1}\tilde{\boldsymbol{u}}}{d}, \tag{59}$$

is derived by taking the suboptimal $\boldsymbol{v} = \tilde{\boldsymbol{u}}/\sqrt{d}$ [91]. The inequality (59) is valid for every QC, and numerical calculations reveal that it is tight in a wide regimes of parameters. In particular, for $\bar{n}_T \gg 2\bar{n}_s$, and taking the statistical average, we find the simplified expression

$$\frac{\mathcal{E}_{\rm QC}[\tilde{\boldsymbol{u}}^T \boldsymbol{\mathcal{M}}(\tilde{\boldsymbol{u}})^{-1}\tilde{\boldsymbol{u}}]}{d} = \frac{e^{-2r}}{\bar{n}_T} + \frac{\bar{n}_s \mathcal{S}}{\bar{n}_T^2}, \tag{60}$$

where $\mathcal{S} \equiv \mathcal{E}_{\rm QC}[d\sum_{j=1}^d \tilde{u}_j^4]$ [91]. Equation (60) is plot as solid black line in Fig. 10(a). We recognize different scalings for different regimes of parameters and discuss them in the following.

1. Regime $\bar{n}_T \gg (e^{2r}+1)\bar{n}_s$

In this regime, the moment matrix simplifies to

$$\boldsymbol{\mathcal{M}}^{-1} = \frac{e^{-2r}-1}{\bar{n}_c}\tilde{\boldsymbol{u}}\tilde{\boldsymbol{u}}^T + \frac{1}{\bar{n}_c}\boldsymbol{I}_d, \tag{61}$$

where $\boldsymbol{I}_d$ is the $d\times d$ identity matrix. Equation (61) can be diagonalized straightforwardly: we find $\mu_{\max} = \bar{n}_c e^{2r}$, the corresponding eigenvector being $\boldsymbol{v}_{\mu_{\max}} = \tilde{\boldsymbol{u}}/\sqrt{d}$. In this case, the upper bound $\tilde{\boldsymbol{u}}^T \boldsymbol{\mathcal{M}}(\tilde{u})^{-1}\tilde{\boldsymbol{u}})/\sqrt{d}$ is tight, with the first term in Eq. (60) dominating over the second one. The optimal sensitivity

$$\min_{\boldsymbol{v}\in\mathbb{R}^d} \Delta^2(\boldsymbol{v}\cdot\boldsymbol{\theta})_{\rm em} = \frac{e^{-2r}}{\bar{n}_T} \tag{62}$$

is shown as a dot-dashed line in Fig. 10(a) and found to agree with the numerics. It is worth noticing that the result of Eq. (62) is independent of vector $\tilde{\boldsymbol{u}}$, so that averaging over the QC has almost no effect on the sensitivity [error bars in Fig. 10(a) are so small that they are hidden by the corresponding numerical data points]. Below we show

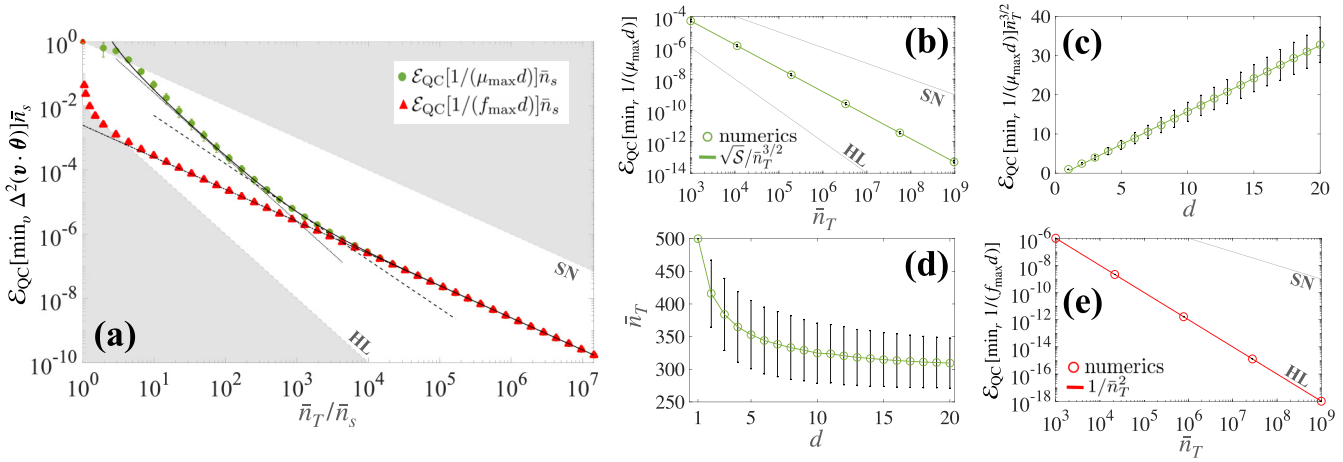

FIG. 10. (a) Optimized phase uncertainties as functions of $\bar{n}_T/\bar{n}_s$, for fixed $\bar{n}_s = 100$ and $d = 10$. In all panels, $\mathcal{E}_{\rm QC}[\cdots]$ indicates statistical average over 10^4 random choices of the unitary transformation $\boldsymbol{U}^\dagger_{\rm QC}$. Symbols show $\mathcal{E}_{\rm QC}[1/(\mu_{\max}d)]$ (green dots) and $\mathcal{E}_{\rm QC}[1/(f_{\max}d)]$ (red triangles). The solid black line is Eq. (60). The dot-dashed line is $e^{-2r}/\bar{n}_T$, Eq. (62), the dashed line is $\sqrt{\mathcal{S}}/\bar{n}_T^{3/2}$, Eq. (63), and the dotted line is $\bar{n}_s\mathcal{S}/\bar{n}_T^2$, Eq. (64). The gray regions are defined by $1/\bar{n}_T$ (SN) and $1/\bar{n}_T^2$ (HL) [these limits are also reported in panels (b) and (e)]. (b) $\mathcal{E}_{\rm QC}[\min_r 1/(\mu_{\max}d)]$ as a function of $\bar{n}_T$ and for $d = 10$ (circles). The solid green line is Eq. (63). Panel (c) shows $\mathcal{E}_{\rm QC}[\min_r 1/(\mu_{\max}d)]\bar{n}_T^{3/2}$ as a function of d and for $\bar{n}_T = 10^6$ (circles). The solid green line is Eq. (63). The corresponding optimal values of $\bar{n}_s$ are shown as circles in panel (d), where the solid line is the theoretical prediction $\bar{n}_s \approx \sqrt{\bar{n}_T/(4\mathcal{S})}$ with $\mathcal{S} \equiv \mathcal{E}_{\rm QC}[d\sum_{j=1}^d \tilde{u}_j^4]$. Finally, panel (e) plots $\mathcal{E}_{\rm QC}[\min_r 1/(f_{\max}d)]$ as a function of $\bar{n}_T$ and for $d = 10$ (circles). The solid red line is Eq. (66). Error bars in all panels are root mean square fluctuations.

that $f_{\max} = \mu_{\max} = \bar{n}_c e^{2r}$ in this regime, with corresponding eigenvectors $\boldsymbol{v}_{f_{\max}} = \boldsymbol{v}_{\mu_{\max}} = \tilde{\boldsymbol{u}}/\sqrt{d}$. The optimal sensitivity predicted by the QFIM is thus saturated by the practical estimation method given by the method of moments: in the present limit, $\mathcal{E}_{\rm QC}[1/(\mu_{\max}d)] = \mathcal{E}_{\rm QC}[1/(f_{\max}d)] = e^{-2r}/\bar{n}_T$ with negligible fluctuations due to random choices of the QC.

2. *Optimal squeezing for $\bar{n}_T \approx (e^{2r}+1)\bar{n}_s$*

We now optimize the squeezing parameter in order to maximize $\mu_{\max}$, for a given average total number of particles $\bar{n}_T$ and QC transformation. Such optimization cannot be performed analytically: for each QC, we evaluate numerically the maximum eigenvalue $\mu_{\max}$ of the corresponding $\boldsymbol{\mathcal{M}}$ and optimize it with respect to $\bar{n}_s$. Numerical results are compared to the analytical optimization of Eq. (60). For $\bar{n}_s \gg 1$ (such that $e^{2r} \approx 4\bar{n}_s$) this predicts

$$\min_r \frac{\mathcal{E}_{\rm QC}[\tilde{u}^T\mathcal{M}(\tilde{u})^{-1}\tilde{u}]}{d} \approx \frac{\sqrt{\mathcal{S}}}{\bar{n}_T^{3/2}} \tag{63}$$

for $\bar{n}_s \approx \sqrt{\bar{n}_T/(4\mathcal{S})}$. In Fig. 10(b) we plot $\mathcal{E}_{\rm QC}[\min_{\bar{n}_s} 1/(\mu_{\max}d)]$ as a function of $\bar{n}_T$ and for fixed d (dots). The solid line is Eq. (63). In Fig. 10(c) we plot $\mathcal{E}_{\rm QC}[\min_{\bar{n}_s} 1/\mu_{\max}]\bar{n}_T^{3/2}$ as a function of d, and the corresponding optimal values of $\bar{n}_s$ are shown in Fig. 10(d). Dots are numerical results, and the solid line is the theoretical prediction $\bar{n}_s \approx \sqrt{\bar{n}_T/(4\mathcal{S})}$. Equation (63) is further shown as a dashed line in Fig. 10(a).

3. *Transient Heisenberg scaling for $2\bar{n}_s \ll \bar{n}_T \ll (e^{2r}+1)\bar{n}_s$*

In this regime, the first term in Eq. (60) can be neglected, and we obtain

$$\frac{\mathcal{E}_{\rm QC}[\tilde{u}^T\mathcal{M}(\tilde{u})^{-1}\tilde{u}]}{d} \approx \frac{\bar{n}_s\mathcal{S}}{\bar{n}_T^2}. \tag{64}$$

This predicts a transient Heisenberg scaling, for fixed $\bar{n}_s$, with prefactor approximately given by $\bar{n}_s$. This prediction is confirmed in Fig. 10(a), where Eq. (64) is shown as a dotted line.

4. *Quantum Cramér-Rao bound*

In the regime $\bar{n}_T \gg 2\bar{n}_s$, the QFIM assumes the simple form

$$\mathcal{F}_{\mathbf{Q}} = \bar{n}_c(e^{2r}-1)\tilde{\boldsymbol{u}}\tilde{\boldsymbol{u}}^T + \bar{n}_c\boldsymbol{I}_d. \tag{65}$$

The maximum eigenvalue is $f_{\max} = e^{2r}\bar{n}_c$ and the corresponding eigenvector is $\boldsymbol{v}_{f_{\max}} = \tilde{\boldsymbol{u}}/\sqrt{d}$. For $\bar{n}_T \gg 2\bar{n}_s$ we find $\min_{\boldsymbol{v}\in\mathbb{R}^d}\Delta^2(\boldsymbol{v}\cdot\boldsymbol{\theta})_{\rm eQ} = e^{-2r}/\bar{n}_T$. Furthermore, taking $\bar{n}_s \gg 1$ (so that $\bar{n}_s \approx e^{2r}/4$), we can optimize $f_{\max} = 4\bar{n}_c\bar{n}_s$ with respect to $\bar{n}_s$, for a fixed $\bar{n}_T$: replacing $\bar{n}_s = \bar{n}_T - \bar{n}_c d$ and taking the derivative with respect to $\bar{n}_c$, we find the optimal condition $d\bar{n}_c = \bar{n}_s = \bar{n}_T/2$. This predicts the saturation of the Heisenberg limit

$$\min_{\boldsymbol{v}\in\mathbb{R}^d}\Delta^2(\boldsymbol{v}\cdot\boldsymbol{\theta})_{\rm eQ} = \frac{1}{\bar{n}_T^2} \tag{66}$$

with respect to the total number of particles $\bar{n}_T$. In Fig. 10(e) we show the the statistical average of $\min_{\bar{n}_s} 1/(f_{\max}d)$ (dots) as a function of $\bar{n}_T$. The solid line is $1/\bar{n}_T^2$.

In Fig. 10(a) we plot $1/(f_{\max}d)$, averaged on random choices of the QC (triangles) for fixed $\bar{n}_s = 100$ and d. Numerical simulations agree well with analytical predictions in

the different limits. The QCRB shows Heisenberg scaling for $\bar{n}_T/\bar{n}_s \approx 2$ and tends to subshot noise scaling faster than the method of moments sensitivity, i.e., the sub-SN scaling is achieved for smaller values of $\bar{n}_T$.

VII. DISCUSSION AND CONCLUSIONS

We have studied an analytically solvable, versatile, and experimentally-relevant model of multiparameter estimation. The protocol is based on an array of MZIs [see Fig. 1(a)] and uses a single squeezed-vacuum state and d coherent states. We address various regimes depending on the relative intensity of the squeezed light. We show the possibility to estimate arbitrary linear combination $\boldsymbol{v}\cdot\boldsymbol{\theta}$ of d phase shifts with sub-SN sensitivity with respect to the average total number of particles in the input state.

The key element of our proposal is the configurable QC. It optimally distributes a single squeezed-vacuum state among d output modes, generating mode entanglement. In particular, we have explicitly shown that the QC allows to squeeze the variance of an opportune collective quadrature, given by a linear combination of modes, below the vacuum limit. Such a quadrature squeezing is responsible for reducing the uncertainty $\Delta^2(\boldsymbol{v}\cdot\boldsymbol{\theta})$ below the SN. This possibility is absent in the separable strategy of Fig. 1(b), which instead requires d squeezed-vacuum states, one for each MZI, in order to estimate $\boldsymbol{v}\cdot\boldsymbol{\theta}$ with a sub-SN sensitivity. An analysis of possible imperfections shows that the scheme is not especially fragile and tolerates a reasonable amount of losses and noise. Upscaling to large d builds on the possibility to create reliable multimode QCs [54,55], which is a general problem in quantum technologies. We notice that Refs. [54,55] have experimentally realized a QC for the splitting of squeezed light up to $d = 4$ modes and used it for sensing. As a main difference, our protocol consider the estimation of relative phase shifts in MZIs: here sensitivity bounds and the comparison with the separable strategy accounts for the total average number of particles in the probe state and the output detection does not require additional resources.

The maximum gain of the entangled over the separable strategy is a factor d, reached for the estimation of the average phase $\boldsymbol{v}_{\rm av}\cdot\boldsymbol{\theta} = \sum_{j=1}^{d}\theta_j/d$ and obtained when fixing the average total number of particles in the squeezed state(s). An interesting case is when the separable strategy is run with d copies of the squeezed-vacuum state used in the entangled scheme and the same mean number of particles $\bar{n}_T$. In this case, the two strategies reach the same sensitivity, despite the entangled scheme using (a factor d) less nonclassical states.

While the literature on distributed quantum sensing has mainly focused on the estimation of specific linear combinations of different parameters, the possibility of optimizing the sensor array for the estimation of *any* $\boldsymbol{v}\cdot\boldsymbol{\theta}$, as discussed in this paper, is generally highly desirable. This possibility has been shown only in the configurable multimode displacement sensor of Ref. [55] and for multipass phase sensing [85] using a photonic Bell state [73]. Further configurable approaches include the splitting and multimode recombination of squeezed-vacuum light [68] and twin-Fock states [60]. In our case, the sensing scheme uses local measurements, a simple phase estimation scheme, and avoids the recombination of the states using a second multimode beam-splitter [60,66,68]. In addition, we show the possibility to saturate the quantum Cramér-Rao bound by measuring the intensity at the local outputs of the MZIs, without requiring any additional recombination of the modes. The scheme is thus particularly suitable for spatially distributed sensing. In particular, optimizing the relative intensity of the squeezed-vacuum state, it is possible to reach the Heisenberg limit.

A further interesting problems raised in the context of multiparameter estimation is whether a single sensor network allows the estimation of multiple linear combination of phases at the same time [76]. This problem is solved here by changing the mode D of the QC where the squeezed-vacuum state is injected; see Fig. 1(a). Indeed, a single d-mode QC can be optimized to estimate d different (e.g., orthogonal) linear combinations $\boldsymbol{v}_D\cdot\boldsymbol{\theta}$ (with $D = 1,\ldots,d$ and $\boldsymbol{v}_i\cdot\boldsymbol{v}_j = \delta_{ij}$) with the same sensitivity: each input mode D of the QC corresponds to a specific optimal $\boldsymbol{v}_D\cdot\boldsymbol{\theta}$.

The results of this work are relevant in current experiments realizing squeezed-vacuum light and multimode linear splitting transformations [54,55,57]. They pave the way to distributed sensing using multiple MZIs—in both optical and atomic systems—with a large variety of applications ranging from field and biological sensing, gravitational wave detection, quantum clocks, and inertial measurements.

ACKNOWLEDGMENTS

We thank R. Corgier and V. Gebhart for discussions. We acknowledge financial support from the European Union's Horizon 2020 Qombs Project (FET Flagship on Quantum Technologies Grant No. 820419) and the QuantEra grant SQUEIS.

APPENDIX

1. Derivation of Eqs. (7) and (8)

Our methods are based on a technique to calculate the QFIM that was outlined in Ref. [92]. It should be noticed, however, that Ref. [92] considered a different sensing configuration: the generalization to the array of MZIs is not straightforward and requires additional algebraic work. Furthermore, our calculation leads to a different expression for the matrix $\boldsymbol{h}$ than that reported in Ref. [92] [see Eq. (A22) below, the subsequent discussion, and the Erratum Ref. [93]]. Alternative approaches to calculate the QFIM of Gaussian states have been also considered; see Refs. [63,66,94,95].

a. Preliminary definitions

We consider the general case where a product of d' single-mode squeezed states is sent to a passive linear network $\hat{A}^\dagger$ and transformed according to

$$|\Psi\rangle = \hat{A}^\dagger \bigotimes_{k=1}^{d'} |\beta_k, \xi_k\rangle. \tag{A1}$$

Here $|\beta_k, \xi_k\rangle$ is the single-mode displaced squeezed state in the mode k: β_k is the coherent amplitude of the state and $\xi_k = r_k e^{i\varphi_k}$ its squeezing parameter. In the following, we will

assume that $\hat{A}^\dagger$ is a Gaussian unitary, that is, a unitary operator which transforms Gaussian states into Gaussian states. Because $\hat{A}^\dagger$ is also a passive, i.e., particle-number preserving, transformation, if we set $\hat{\boldsymbol{c}} = (\hat{c}_1, \ldots, \hat{c}_{d'})^T$, a relation $\hat{A}\hat{\boldsymbol{c}}\hat{A}^\dagger = \hat{\boldsymbol{c}}' = \mathcal{A}\hat{\boldsymbol{c}}$ must hold, with $\mathcal{A}$ a unitary matrix (similarly, $\hat{A}\hat{\boldsymbol{c}}^\dagger\hat{A}^\dagger = \mathcal{A}^*\hat{\boldsymbol{c}}^\dagger$). Here $\hat{c}_k^\dagger$ and $\hat{c}_k$ are bosonic creation and annihilation operators, respectively,

We recall the definition of the Q function for the state $|\Phi\rangle$ of a generic d'-mode system:

$$Q(\boldsymbol{\alpha}) = \frac{|\langle\boldsymbol{\alpha}|\Phi\rangle|^2}{\pi}, \tag{A2}$$

where $|\boldsymbol{\alpha}\rangle = \bigotimes_{k=1}^{d'} |\alpha_k\rangle$, $|\alpha_k\rangle$ being an arbitrary single-mode coherent state in mode k. From the point of view of the Q function, a transformation $\hat{A}^\dagger|\Phi\rangle$ is equivalent to a transformation $\hat{A}|\boldsymbol{\alpha}\rangle$ of the coherent states; moreover, it is a well-known property that a Gaussian passive transformation $\hat{A}$ sends a product of coherent states into another product of coherent states, in particular: $\hat{A}|\boldsymbol{\alpha}\rangle = |\boldsymbol{\alpha}'\rangle = |\boldsymbol{A\alpha}\rangle$. $\boldsymbol{A}$ is the matrix that implements the transformation $\boldsymbol{\alpha}' = \boldsymbol{A\alpha}$ of the amplitudes of the coherent states associated with the Q function. It is possible to show that this matrix is the same as the one which describes the transformation of the annihilation operators implemented by $\hat{A}$, that is, $\hat{A}^\dagger\,\hat{\boldsymbol{c}}\,\hat{A} = \hat{\boldsymbol{c}}' = \boldsymbol{A}\hat{\boldsymbol{c}}$, and, correspondingly, the Hermitian conjugate of the matrix which describes the transformation of the annihilation operators implemented by $\hat{A}^\dagger$, which we have denoted as $\mathcal{A}$ above. The relation $\mathcal{A}^\dagger = \boldsymbol{A}$ will be frequently used in what follows.

Using the Q-function representation of the states, (A1), Ref. [92] showed that

$$\langle\hat{n}_j\rangle = -1 + \partial_j\partial_j^* G(\boldsymbol{\mu})|_{\boldsymbol{\mu}=0}, \tag{A3}$$

$$\langle\hat{n}_j\hat{n}_k\rangle = [\partial_j\partial_j^*\partial_k\partial_k^* - (1+\delta_{jk})\partial_j\partial_j^* - \partial_k\partial_k^*]G(\boldsymbol{\mu})|_{\boldsymbol{\mu}=0} + 1, \tag{A4}$$

where $\boldsymbol{\mu} = (\lambda_1, \ldots, \lambda_{d'}, \lambda_1^*, \ldots, \lambda_{d'}^*)^T$ is an arbitrary $2d'$-dimensional complex vector, ∂_j, ∂_j^* are shorthand notation for $\partial/\partial\lambda_j$, $\partial/\partial\lambda_j^*$, $\hat{n}_j = \hat{c}_j^\dagger\hat{c}_j$, and the expectation values are evaluated in state $|\Psi\rangle$. We have $G(\boldsymbol{\mu}) = e^\Delta$, where

$$\Delta \equiv \tfrac{1}{4}(\boldsymbol{v}_{\boldsymbol{b}}^\dagger\boldsymbol{M}^{-1}\boldsymbol{\mu} + \boldsymbol{\mu}^\dagger\boldsymbol{M}^{-1}\boldsymbol{v}_{\boldsymbol{b}} + \boldsymbol{\mu}^\dagger\boldsymbol{M}^{-1}\boldsymbol{\mu}), \tag{A5}$$

$$\boldsymbol{v}_{\boldsymbol{b}} = (b_1, \ldots, b_{d'}, b_1^*, \ldots, b_{d'}^*)^T, \tag{A6}$$

$$b_j = \sum_k \boldsymbol{A}_{jk}^\dagger(\beta_k + \beta_k^* e^{i\varphi_k}\tanh r_k), \tag{A7}$$

$$\boldsymbol{M}^{-1} = 2\begin{pmatrix} \boldsymbol{E} & -\boldsymbol{N}\boldsymbol{E}^T \\ -\boldsymbol{N}^\dagger\boldsymbol{E} & \boldsymbol{E}^T \end{pmatrix}, \tag{A8}$$

$$\boldsymbol{N} = \boldsymbol{A}^\dagger\boldsymbol{D}\boldsymbol{A}^*, \tag{A9}$$

$$\boldsymbol{E} = \boldsymbol{A}^\dagger\boldsymbol{C}\boldsymbol{A}, \tag{A10}$$

$$\boldsymbol{C}_{jk} = \delta_{jk}\cosh^2 r_k, \tag{A11}$$

and

$$\boldsymbol{D}_{jk} = \delta_{jk}e^{i\varphi_k}\tanh r_k. \tag{A12}$$

Using Eq. (A8), we find

$$\Delta = \frac{1}{4}\left[\begin{pmatrix}\boldsymbol{b}^* & \boldsymbol{b}\end{pmatrix}\cdot 2\begin{pmatrix}\boldsymbol{E} & -\boldsymbol{N}\boldsymbol{E}^T\\ -\boldsymbol{N}^\dagger\boldsymbol{E} & \boldsymbol{E}^T\end{pmatrix}\begin{pmatrix}\boldsymbol{\lambda}\\ \boldsymbol{\lambda}^*\end{pmatrix} + \begin{pmatrix}\boldsymbol{\lambda}^* & \boldsymbol{\lambda}\end{pmatrix}\cdot 2\begin{pmatrix}\boldsymbol{E} & -\boldsymbol{N}\boldsymbol{E}^T\\ -\boldsymbol{N}^\dagger\boldsymbol{E} & \boldsymbol{E}^T\end{pmatrix}\begin{pmatrix}\boldsymbol{b}\\ \boldsymbol{b}^*\end{pmatrix} + \begin{pmatrix}\boldsymbol{\lambda}^* & \boldsymbol{\lambda}\end{pmatrix}\cdot 2\begin{pmatrix}\boldsymbol{E} & -\boldsymbol{N}\boldsymbol{E}^T\\ -\boldsymbol{N}^\dagger\boldsymbol{E} & \boldsymbol{E}^T\end{pmatrix}\begin{pmatrix}\boldsymbol{\lambda}\\ \boldsymbol{\lambda}^*\end{pmatrix}\right],$$

which we can write more explicitly as

$$\begin{aligned}\Delta = \tfrac{1}{2}[&\boldsymbol{b}^*\cdot(\boldsymbol{E}\boldsymbol{\lambda} - \boldsymbol{N}\boldsymbol{E}^T\boldsymbol{\lambda}^*) + \boldsymbol{b}\cdot(-\boldsymbol{N}^\dagger\boldsymbol{E}\boldsymbol{\lambda} + \boldsymbol{E}^T\boldsymbol{\lambda}^*) + \boldsymbol{\lambda}^*\cdot(\boldsymbol{E}\boldsymbol{b} - \boldsymbol{N}\boldsymbol{E}^T\boldsymbol{b}^*) + \boldsymbol{\lambda}\cdot(-\boldsymbol{N}^\dagger\boldsymbol{E}\boldsymbol{b} + \boldsymbol{E}^T\boldsymbol{b}^*)\\ &+ \boldsymbol{\lambda}^*\cdot(\boldsymbol{E}\boldsymbol{\lambda} - \boldsymbol{N}\boldsymbol{E}^T\boldsymbol{\lambda}^*) + \boldsymbol{\lambda}\cdot(-\boldsymbol{N}^\dagger\boldsymbol{E}\boldsymbol{\lambda} + \boldsymbol{E}^T\boldsymbol{\lambda}^*)].\end{aligned}$$

We then calculate the first and second partial derivatives of Δ with respect to λ_j and λ_j^*:

$$\partial_j\Delta = \frac{1}{2}\sum_k[-((\boldsymbol{N}^\dagger\boldsymbol{E})_{jk} + (\boldsymbol{N}^\dagger\boldsymbol{E})_{kj})(\boldsymbol{\lambda}_k + \boldsymbol{b}_k) + 2\boldsymbol{E}_{kj}(\boldsymbol{\lambda}_k^* + \boldsymbol{b}_k^*)] = \sum_k \boldsymbol{E}_{jk}^*(\boldsymbol{\lambda}_k^* + \boldsymbol{b}_k^*) - (\boldsymbol{E}\boldsymbol{N})_{jk}^*(\boldsymbol{\lambda}_k + \boldsymbol{b}_k), \tag{A13}$$

$$\partial_j^*\Delta = \frac{1}{2}\sum_k[2\boldsymbol{E}_{jk}(\boldsymbol{\lambda}_k + \boldsymbol{b}_k) - ((\boldsymbol{N}\boldsymbol{E}^T)_{jk} + (\boldsymbol{N}\boldsymbol{E}^T)_{kj})(\boldsymbol{\lambda}_k^* + \boldsymbol{b}_k^*)] = \sum_k \boldsymbol{E}_{jk}(\boldsymbol{\lambda}_k + \boldsymbol{b}_k) - (\boldsymbol{E}\boldsymbol{N})_{jk}(\boldsymbol{\lambda}_k^* + \boldsymbol{b}_k^*), \tag{A14}$$

$$\partial_j^*\partial_k\Delta = \boldsymbol{E}_{jk}, \tag{A15}$$

$$\partial_j\partial_k^*\Delta = \boldsymbol{E}_{kj} = \boldsymbol{E}_{jk}^*, \tag{A16}$$

$$\partial_j^*\partial_k^*\Delta = -\tfrac{1}{2}((\boldsymbol{N}\boldsymbol{E}^T)_{jk} + (\boldsymbol{N}\boldsymbol{E}^T)_{kj}) = -(\boldsymbol{E}\boldsymbol{N})_{jk}, \tag{A17}$$

$$\partial_j\partial_k\Delta = -\tfrac{1}{2}((\boldsymbol{N}^\dagger\boldsymbol{E})_{jk} + (\boldsymbol{N}^\dagger\boldsymbol{E})_{kj}) = -(\boldsymbol{E}\boldsymbol{N})_{jk}^*. \tag{A18}$$

To derive the above equations, we have used the following relations: $\boldsymbol{E} = \boldsymbol{E}^\dagger$ and $\boldsymbol{N} = \boldsymbol{N}^T$, which also imply $\boldsymbol{E}^T = \boldsymbol{E}^*$ and $\boldsymbol{N}^\dagger = \boldsymbol{N}^*$, respectively, $(\boldsymbol{E}\boldsymbol{N})^T = \boldsymbol{E}\boldsymbol{N}$, $\boldsymbol{N}\boldsymbol{E}^T = (\boldsymbol{E}\boldsymbol{N})^T = \boldsymbol{E}\boldsymbol{N}$, and $\boldsymbol{N}^\dagger\boldsymbol{E} = (\boldsymbol{E}\boldsymbol{N})^\dagger = ((\boldsymbol{E}\boldsymbol{N})^T)^* = (\boldsymbol{E}\boldsymbol{N})^*$. We are now ready to work out the partial derivatives of $G(\boldsymbol{\mu})$ that appear in Eqs. (A3) and (A4):

$$\partial_j\partial_j^* G(\boldsymbol{\mu}) = (\partial_j\partial_j^*\Delta)e^\Delta + (\partial_j\Delta)(\partial_j^*\Delta)e^\Delta = (\boldsymbol{E}_{jj} + (\partial_j\Delta)(\partial_j^*\Delta))e^\Delta$$

and

$$\begin{aligned}\partial_j\partial_j^*\partial_k\partial_k^* G(\boldsymbol{\mu}) &= \partial_j[(\boldsymbol{E}_{kk}+(\partial_k\Delta)(\partial_k^*\Delta))(\partial_j^*\Delta)e^{\Delta}+((\partial_j^*\partial_k\Delta)(\partial_k^*\Delta)+(\partial_k\Delta)(\partial_j^*\partial_k^*\Delta))e^{\Delta}]\\ &= [(\boldsymbol{EN})_{jk}(\boldsymbol{EN})_{jk}^*-(\boldsymbol{EN})_{jk}^*(\partial_j^*\Delta)(\partial_k^*\Delta)-(\boldsymbol{EN})_{jk}(\partial_j\Delta)(\partial_k\Delta)+\boldsymbol{E}_{jk}\boldsymbol{E}_{jk}^*+\boldsymbol{E}_{jk}(\partial_j\Delta)(\partial_k^*\Delta)+\boldsymbol{E}_{jk}^*(\partial_j^*\Delta)(\partial_k\Delta).\\ &\quad+(\boldsymbol{E}_{jj}+(\partial_j\Delta)(\partial_j^*\Delta))(\boldsymbol{E}_{kk}+(\partial_k\Delta)(\partial_k^*\Delta))]e^{\Delta}.\end{aligned}$$

By evaluating the derivatives at $\boldsymbol{\mu}=0$, we get

$$\partial_j\partial_j^* G(\boldsymbol{\mu})|_{\boldsymbol{\mu}=0} = \boldsymbol{E}_{jj}+(\partial_j\Delta)_0(\partial_j^*\Delta)_0,$$

where $(\partial_j\Delta)_0$ is shorthand notation for $(\partial_j\Delta)|_{\boldsymbol{\mu}=0}$, and

$$\begin{aligned}\partial_j\partial_j^*\partial_k\partial_k^* G(\boldsymbol{\mu})|_{\boldsymbol{\mu}=0} &= (\boldsymbol{EN})_{jk}(\boldsymbol{EN})_{jk}^*-(\boldsymbol{EN})_{jk}^*(\partial_j^*\Delta)_0(\partial_k^*\Delta)_0-(\boldsymbol{EN})_{jk}(\partial_j\Delta)_0(\partial_k\Delta)_0+\boldsymbol{E}_{jk}\boldsymbol{E}_{jk}^*+\boldsymbol{E}_{jk}(\partial_j\Delta)_0(\partial_k^*\Delta)_0\\ &\quad+\boldsymbol{E}_{jk}^*(\partial_j^*\Delta)_0(\partial_k\Delta)_0+(\boldsymbol{E}_{jj}+(\partial_j\Delta)_0(\partial_j^*\Delta)_0)(\boldsymbol{E}_{kk}+(\partial_k\Delta)_0(\partial_k^*\Delta)_0).\end{aligned}$$

Finally, Eqs. (A3) and (A4) are rewritten as

$$\langle\hat{n}_j\rangle = -1+\boldsymbol{E}_{jj}+(\partial_j\Delta)_0(\partial_j^*\Delta)_0 \tag{A19}$$

and

$$\begin{aligned}\langle\hat{n}_j\hat{n}_k\rangle &= (\boldsymbol{EN})_{jk}(\boldsymbol{EN})_{jk}^*-(\boldsymbol{EN})_{jk}^*(\partial_j^*\Delta)_0(\partial_k^*\Delta)_0-(\boldsymbol{EN})_{jk}(\partial_j\Delta)_0(\partial_k\Delta)_0+\boldsymbol{E}_{jk}\boldsymbol{E}_{jk}^*+\boldsymbol{E}_{jk}(\partial_j\Delta)_0(\partial_k^*\Delta)_0+\boldsymbol{E}_{jk}^*(\partial_j^*\Delta)_0(\partial_k\Delta)_0\\ &\quad+\langle\hat{n}_j\rangle\langle\hat{n}_k\rangle-\delta_{jk}(\boldsymbol{E}_{jj}+(\partial_j\Delta)_0(\partial_j^*\Delta)_0).\end{aligned} \tag{A20}$$

At this point, we introduce the $d'\times d'$ matrix $\boldsymbol{h}$, with elements $\boldsymbol{h}_{jk}=\langle\hat{n}_j\hat{n}_k\rangle-\langle\hat{n}_j\rangle\langle\hat{n}_k\rangle$. Taking into account the above equations for $\langle\hat{n}_j\rangle$ and $\langle\hat{n}_j\hat{n}_k\rangle$, we have

$$\begin{aligned}\boldsymbol{h}_{jk} &= (\boldsymbol{EN})_{jk}(\boldsymbol{EN})_{jk}^*-(\boldsymbol{EN})_{jk}^*(\partial_j^*\Delta)_0(\partial_k^*\Delta)_0-(\boldsymbol{EN})_{jk}(\partial_j\Delta)_0(\partial_k\Delta)_0+\boldsymbol{E}_{jk}\boldsymbol{E}_{jk}^*+\boldsymbol{E}_{jk}(\partial_j\Delta)_0(\partial_k^*\Delta)_0+\boldsymbol{E}_{jk}^*(\partial_j^*\Delta)_0(\partial_k\Delta)_0\\ &\quad-\delta_{jk}(\boldsymbol{E}_{jj}+(\partial_j\Delta)_0(\partial_k^*\Delta)_0).\end{aligned}$$

This equation can be rewritten in a compact form by introducing the vector $\boldsymbol{\gamma}_j\equiv(\partial_j\Delta)_0$. Notice that $(\gamma_j)^*=(\partial_j^*\Delta)_0$. From Eqs. (A13) and (A14), we get $\boldsymbol{\gamma}_j=\sum_k\boldsymbol{E}_{jk}^*b_k^*-(\boldsymbol{EN})_{jk}^*b_k$, namely,

$$\boldsymbol{\gamma}=\boldsymbol{E}^*\boldsymbol{b}^*-(\boldsymbol{EN})^*\boldsymbol{b}. \tag{A21}$$

Finally, making use of vector $\boldsymbol{\gamma}$ and of the Hadamard entry-wise product $\circ$, we can rewrite $\boldsymbol{h}$ in the compact form:

$$\begin{aligned}\boldsymbol{h} &= \boldsymbol{EN}\circ(\boldsymbol{EN})^*-\boldsymbol{EN}\circ\boldsymbol{\gamma}\boldsymbol{\gamma}^T-(\boldsymbol{EN})^*\circ(\boldsymbol{\gamma}\boldsymbol{\gamma}^T)^*+\boldsymbol{E}\circ\boldsymbol{E}^*\\ &\quad+\boldsymbol{E}\circ\boldsymbol{\gamma}\boldsymbol{\gamma}^\dagger+\boldsymbol{E}^*\circ(\boldsymbol{\gamma}\boldsymbol{\gamma}^\dagger)^*-(\boldsymbol{E}+\boldsymbol{\gamma}\boldsymbol{\gamma}^\dagger)\circ\boldsymbol{I}.\end{aligned} \tag{A22}$$

Matrix $\boldsymbol{h}$ is real and symmetric. An expression similar to Eq. (A22) was derived in Ref. [92]; see Eq. (14) in that reference. There are, however, important differences with respect to Eq. (A22). Only our formula for $\boldsymbol{h}$ reproduces the correct and well-known expression of the QFIM relative to a single MZI fed with coherent and squeezed-vacuum input light, corresponding to the case $d=1$ (see the following section for the derivation of the QFIM).

In our sensing scheme, the initial state is given by

$$|\Psi_{\text{in}}\rangle = |\Psi_{\text{in}}^{\alpha}\rangle\otimes|\Psi_{\text{in}}^{\xi}\rangle.$$

The state $|\Psi_{\text{in}}^{\alpha}\rangle=|\alpha_1\rangle\otimes\cdots\otimes|\alpha_d\rangle$ is a product state of coherent states in modes $a_1,\ldots,a_d$. The state $|\Psi_{\text{in}}^{\xi}\rangle=|0\rangle\otimes\cdots\otimes|\xi\rangle\otimes\cdots\otimes|0\rangle$ is a product of a squeezed-vacuum state $|\xi\rangle$ in mode $(b_{\text{in}})_D$ and the vacuum $|0\rangle$ in modes $(b_{\text{in}})_j$ for $j=1,\ldots,d$ and $j\neq D$. This initial state should be compared with the product state in Eq. (A1). In order to facilitate the identification of the two cases, we can set $\hat{a}_j\equiv\hat{c}_j$ and $(\hat{b}_{\text{in}})_j\equiv\hat{c}_{j+d}$ $(j=1,\ldots,d)$, thus introducing a more homogeneous notation valid for all of the $2d=d'$ input modes of the sensor array. We then identify the $2d\times 2d$ unitary matrix corresponding to the mode transformation performed by the QC as

$$\boldsymbol{U}^\dagger=\begin{pmatrix}\boldsymbol{I}_d & 0\\ 0 & \boldsymbol{U}_{\text{QC}}^\dagger\end{pmatrix}.$$

The $d\times d$ identity matrix $\boldsymbol{I}_d$ describes the action of the QC on the coherent states, while $\hat{b}_j=\sum_{k=1}^d(\boldsymbol{U}_{\text{QC}}^\dagger)_{jk}(\hat{b}_{\text{in}})_k$ $(j=1,\ldots,d)$, $\boldsymbol{U}_{\text{QC}}^\dagger$ being a unitary $d\times d$ matrix. We denote the system state after the QC as $|\Psi_{\text{out}}\rangle$, so that we have $|\Psi_{\text{out}}\rangle=\hat{U}^\dagger|\Psi_{\text{in}}\rangle=(\hat{\mathbb{I}}\otimes\hat{U}_{\text{QC}}^\dagger)|\Psi_{\text{in}}^{\alpha}\rangle\otimes|\Psi_{\text{in}}^{\xi}\rangle=|\Psi_{\text{in}}^{\alpha}\rangle\otimes|\Psi_{\text{QC}}\rangle$. In the last equality, we have set $|\Psi_{\text{QC}}\rangle=\hat{U}_{\text{QC}}^\dagger|\Psi_{\text{in}}^{\xi}\rangle$.

b. Inverse moment matrix and method of moments sensitivity

The so-called *moment matrix* corresponds to the covariance matrix of a particular set of estimators of the unknown parameters θ_j, $j=1,\ldots,d$. It is defined as follows [67]:

$$\boldsymbol{\mathcal{M}}=\boldsymbol{G}^T\boldsymbol{\Gamma}^{-1}\boldsymbol{G}, \tag{A23}$$

where

$$\boldsymbol{G}_{jk}=\frac{\partial\langle\hat{X}_j\rangle_{\rho(\boldsymbol{\theta})}}{\partial\theta_k},\qquad j=1,\ldots,K;\ k=1,\ldots,d \tag{A24}$$

and

$$\boldsymbol{\Gamma}_{jk}=\langle\hat{X}_j\hat{X}_k\rangle_{\hat{\rho}(\boldsymbol{\theta})}-\langle\hat{X}_j\rangle_{\hat{\rho}(\boldsymbol{\theta})}\langle\hat{X}_k\rangle_{\hat{\rho}(\boldsymbol{\theta})},\qquad j,k=1,\ldots,K, \tag{A25}$$

$\hat{\rho}(\boldsymbol{\theta})$ being the output state of the whole sensor array. The $\hat{X}_j$, $j = 1, \ldots, K$, are K Hermitian operators which correspond to measurements performed on the output state $\hat{\rho}(\boldsymbol{\theta})$. We choose $\hat{X}_j \equiv (\hat{J}_z)_j = (\hat{a}_j^\dagger \hat{a}_j - \hat{b}_j^\dagger \hat{b}_j)/2$, with $j = 1, \ldots, d$. By this choice, the two matrices $\boldsymbol{G}$ and $\boldsymbol{\Gamma}$ can be evaluated through the Q-function-based technique already illustrated in the previous section. In our case, $\hat{\rho}(\boldsymbol{\theta}) = |\Psi(\boldsymbol{\theta})\rangle\langle\Psi(\boldsymbol{\theta})|$ is a pure state. The phases $\theta_1, \ldots, \theta_d$ to be estimated are encoded in $|\Psi_{\text{out}}\rangle$ [defined in the previous section] through the unitary transformation $\otimes_{j=1}^d e^{-i\theta_j(\hat{J}_y)_j}$, where $e^{-i\theta_j(\hat{J}_y)_j}$ identifies the jth MZI in the array, with $(\hat{J}_y)_j = (\hat{a}_j^\dagger \hat{b}_j - \hat{b}_j^\dagger \hat{a}_j)/2i$. Therefore

$$|\Psi(\boldsymbol{\theta})\rangle = \otimes_{j=1}^d e^{-i\theta_j(\hat{J}_y)_j}|\Psi_{\text{out}}\rangle = \otimes_{j=1}^d e^{-i\theta_j(\hat{J}_y)_j}\hat{U}|\Psi_{\text{in}}\rangle.$$

This equation should be compared with Eq. (A1): the identification $\hat{A}^\dagger = \otimes_{j=1}^d e^{-i\theta_j(\hat{J}_y)_j}\hat{U}^\dagger$ is straightforward. The action of $\hat{A}^\dagger$ on the annihilation operators of the input modes can be represented by the relation $\hat{c}'_j = \sum_k \boldsymbol{A}^\dagger_{jk}\hat{c}_k$ ($j = 1, \ldots, 2d$) with

$$\boldsymbol{A}^\dagger = \begin{pmatrix} \tilde{\boldsymbol{C}} & \tilde{\boldsymbol{S}} \\ -\tilde{\boldsymbol{S}} & \tilde{\boldsymbol{C}} \end{pmatrix}\begin{pmatrix} \boldsymbol{I}_d & 0 \\ 0 & \boldsymbol{U}_{\text{QC}}^\dagger \end{pmatrix} = \begin{pmatrix} \tilde{\boldsymbol{C}} & \tilde{\boldsymbol{S}}\boldsymbol{U}_{\text{QC}}^\dagger \\ -\tilde{\boldsymbol{S}} & \tilde{\boldsymbol{C}}\boldsymbol{U}_{\text{QC}}^\dagger \end{pmatrix}, \quad \text{(A26)}$$

where $\tilde{\boldsymbol{C}}_{jk} = \cos(\theta_j/2)\delta_{jk}$ and $\tilde{\boldsymbol{S}}_{jk} = \sin(\theta_j/2)\delta_{jk}$. On the basis of Eq. (A25) and having set $\hat{X}_j \equiv (\hat{J}_z)_j$, we have

$$\begin{aligned}\boldsymbol{\Gamma}_{jk} &= \langle\Psi(\boldsymbol{\theta})|(\hat{J}_z)_j(\hat{J}_z)_k|\Psi(\boldsymbol{\theta})\rangle \\ &\quad - \langle\Psi(\boldsymbol{\theta})|(\hat{J}_z)_j|\Psi(\boldsymbol{\theta})\rangle\langle\Psi(\boldsymbol{\theta})|(\hat{J}_z)_k|\Psi(\boldsymbol{\theta})\rangle. \quad \text{(A27)}\end{aligned}$$

Since $(\hat{J}_z)_j = (\hat{a}_j^\dagger \hat{a}_j - \hat{b}_j^\dagger \hat{b}_j)/2 = (\hat{c}_j^\dagger \hat{c}_j - \hat{c}_{j+d}^\dagger \hat{c}_{j+d})/2 = (\hat{n}_j - \hat{n}_{j+d})/2$, through simple calculations we can write $\boldsymbol{\Gamma}_{jk}$ in terms of the elements of matrix $\boldsymbol{h}$:

$$\begin{aligned}&\boldsymbol{\Gamma}_{jk} = \tfrac{1}{4}(\boldsymbol{h}_{j,k} + \boldsymbol{h}_{j+d,k+d} - \boldsymbol{h}_{j,k+d} - \boldsymbol{h}_{j+d,k}), \\ &j, k = 1, \ldots, d. \quad \text{(A28)}\end{aligned}$$

Notice that $\boldsymbol{\Gamma}$ is a $d \times d$ matrix, whose elements, according to Eq. (A28), can be obtained as combinations of the elements of $\boldsymbol{h}$, a $2d \times 2d$ matrix. Equation (A22) expresses $\boldsymbol{h}$ in terms of the two matrices $\boldsymbol{E}$ and $\boldsymbol{EN}$ and the vector $\boldsymbol{\gamma}$. $\boldsymbol{E}$ and $\boldsymbol{EN}$ are derived by referring to Eqs. (A9) to (A12). In particular, from Eqs. (A11) and (A12) we get

$$\boldsymbol{C} = \begin{pmatrix} \boldsymbol{I}_d & 0 \\ 0 & \boldsymbol{C}_1 \end{pmatrix} \quad \text{(A29)}$$

and

$$\boldsymbol{CD} = \begin{pmatrix} 0 & 0 \\ 0 & \boldsymbol{C}_1\boldsymbol{D}_1 \end{pmatrix}. \quad \text{(A30)}$$

In the above equations, $\boldsymbol{C_1}$ and $\boldsymbol{C_1D_1}$ are $d \times d$ matrices with elements

$$(\boldsymbol{C_1})_{jk} = \delta_{jk}[(1 - \delta_{Dk}) + \delta_{Dk}c^2] \quad \text{(A31)}$$

and

$$(\boldsymbol{C_1D_1})_{jk} = \delta_{jk}\delta_{Dk}e^{i\varphi}sc, \quad \text{(A32)}$$

respectively, where D is the index of the input port into which $|\xi\rangle$ is injected, and $s \equiv \sinh r$, $c \equiv \cosh r$ (these shortcuts will be repeatedly used below). So we get

$$\boldsymbol{E} = \boldsymbol{A}^\dagger\boldsymbol{C}\boldsymbol{A} = \begin{pmatrix} \tilde{\boldsymbol{C}}^2 + \tilde{\boldsymbol{S}}\boldsymbol{E_1}\tilde{\boldsymbol{S}} & -(\tilde{\boldsymbol{S}}\tilde{\boldsymbol{C}} - \tilde{\boldsymbol{S}}\boldsymbol{E_1}\tilde{\boldsymbol{C}}) \\ -(\tilde{\boldsymbol{S}}\tilde{\boldsymbol{C}} - \tilde{\boldsymbol{C}}\boldsymbol{E_1}\tilde{\boldsymbol{S}}) & \tilde{\boldsymbol{S}}^2 + \tilde{\boldsymbol{C}}\boldsymbol{E_1}\tilde{\boldsymbol{C}} \end{pmatrix}, \quad \text{(A33)}$$

with $\boldsymbol{E_1} = \boldsymbol{U}_{\text{QC}}^\dagger\boldsymbol{C_1}\boldsymbol{U}_{\text{QC}}$, and

$$\boldsymbol{EN} = \boldsymbol{A}^\dagger\boldsymbol{C}\boldsymbol{D}\boldsymbol{A}^* = \begin{pmatrix} \tilde{\boldsymbol{S}}\boldsymbol{E_1}\boldsymbol{N_1}\tilde{\boldsymbol{S}} & \tilde{\boldsymbol{S}}\boldsymbol{E_1}\boldsymbol{N_1}\tilde{\boldsymbol{C}} \\ \tilde{\boldsymbol{C}}\boldsymbol{E_1}\boldsymbol{N_1}\tilde{\boldsymbol{S}} & \tilde{\boldsymbol{C}}\boldsymbol{E_1}\boldsymbol{N_1}\tilde{\boldsymbol{C}} \end{pmatrix}, \quad \text{(A34)}$$

with $\boldsymbol{E_1N_1} = \boldsymbol{U}_{\text{QC}}^\dagger\boldsymbol{C_1}\boldsymbol{D_1}\boldsymbol{U}_{\text{QC}}^*$. We also have

$$\boldsymbol{\gamma} = \boldsymbol{b}^* = \begin{pmatrix} \tilde{\boldsymbol{C}}\boldsymbol{\beta}_0^* \\ -\tilde{\boldsymbol{S}}\boldsymbol{\beta}_0^* \end{pmatrix} = \begin{pmatrix} \tilde{\boldsymbol{C}}\boldsymbol{\gamma}_0 \\ -\tilde{\boldsymbol{S}}\boldsymbol{\gamma}_0 \end{pmatrix}, \quad \text{(A35)}$$

so that

$$\boldsymbol{\gamma}\boldsymbol{\gamma}^\dagger = \begin{pmatrix} \tilde{\boldsymbol{C}}\boldsymbol{\phi}_-\tilde{\boldsymbol{C}} & -\tilde{\boldsymbol{C}}\boldsymbol{\phi}_-\tilde{\boldsymbol{S}} \\ -\tilde{\boldsymbol{S}}\boldsymbol{\phi}_-\tilde{\boldsymbol{C}} & \tilde{\boldsymbol{S}}\boldsymbol{\phi}_-\tilde{\boldsymbol{S}} \end{pmatrix} \quad \text{(A36)}$$

and

$$\boldsymbol{\gamma}\boldsymbol{\gamma}^T = \begin{pmatrix} \tilde{\boldsymbol{C}}\boldsymbol{\phi}_+\tilde{\boldsymbol{C}} & -\tilde{\boldsymbol{C}}\boldsymbol{\phi}_+\tilde{\boldsymbol{S}} \\ -\tilde{\boldsymbol{S}}\boldsymbol{\phi}_+\tilde{\boldsymbol{C}} & \tilde{\boldsymbol{S}}\boldsymbol{\phi}_+\tilde{\boldsymbol{S}} \end{pmatrix}, \quad \text{(A37)}$$

where $(\boldsymbol{\beta_0})_j = |\alpha_j|e^{i\phi_j}$, $(\boldsymbol{\phi_+})_{jk} = |\alpha_j||\alpha_k|e^{-i(\phi_j+\phi_k)}$, $(\boldsymbol{\phi_-})_{jk} = |\alpha_j||\alpha_k|e^{-i(\phi_j-\phi_k)}$. Notice that, to derive $\boldsymbol{\gamma}$, we made use of Eq. (A21) in its simplified form $\boldsymbol{\gamma} = \boldsymbol{b}^*$. Indeed, if each input mode is either in a coherent or in a squeezed-vacuum state, then the following special relations hold: $\boldsymbol{E}^*\boldsymbol{b}^* = \boldsymbol{b}^*$, $(\boldsymbol{EN})^*\boldsymbol{b} = 0$ and $\boldsymbol{b} = \boldsymbol{A}^\dagger\boldsymbol{\beta}$ with $\boldsymbol{\beta} = (\boldsymbol{\beta_0}\ 0)^T$, reducing Eq. (A21) to $\boldsymbol{\gamma} = \boldsymbol{b}^*$.

At this point, we easily get

$$(\boldsymbol{E_1N_1})_{jk} = (\boldsymbol{U}_{\text{QC}}^\dagger\boldsymbol{C_1}\boldsymbol{D_1}\boldsymbol{U}_{\text{QC}}^*)_{jk} = e^{i\varphi}sc\ |u_j||u_k|e^{-i\delta_j}e^{-i\delta_k}, \quad \text{(A38)}$$

$$(\boldsymbol{E_1})_{jk} = (\boldsymbol{U}_{\text{QC}}^\dagger\boldsymbol{C_1}\boldsymbol{U}_{\text{QC}})_{jk} = \delta_{jk} + s^2|u_j||u_k|e^{-i\delta_j}e^{i\delta_k}, \quad \text{(A39)}$$

where we have set $(\boldsymbol{U}_{\text{QC}})_{Dj} \equiv u_j = |u_j|e^{i\delta_j}$. Making use of these two equations, explicit expressions can be easily derived for the submatrices $(\tilde{\boldsymbol{C}}^2 + \tilde{\boldsymbol{S}}\boldsymbol{E_1}\tilde{\boldsymbol{S}})_{jk} = \delta_{jk} + s^2|u_j||u_k|e^{-i\delta_j}e^{i\delta_k}\sin(\theta_j/2)\sin(\theta_k/2)$, $(\tilde{\boldsymbol{S}}\boldsymbol{E_1}\boldsymbol{N_1}\tilde{\boldsymbol{S}})_{jk} = e^{i\varphi}sc\ |u_j||u_k|e^{-i\delta_j}e^{-i\delta_k}\sin(\theta_j/2)\sin(\theta_k/2)$, etc., and also $(\tilde{\boldsymbol{C}}\boldsymbol{\phi}_-\tilde{\boldsymbol{C}})_{jk} = c^2|\alpha_j|\ |\alpha_k|\ e^{-i(\phi_j-\phi_k)}$, $(\tilde{\boldsymbol{C}}\boldsymbol{\phi}_+\tilde{\boldsymbol{C}})_{jk} = c^2|\alpha_j||\alpha_k|e^{-i(\phi_j+\phi_k)}$, etc. Using these results and relying on Eq. (A22), we obtain $\boldsymbol{h}$. Then, making use of Eq. (A28), we get the following expression for $\boldsymbol{\Gamma}$:

$$\begin{aligned}\boldsymbol{\Gamma}_{jk} &= \tfrac{1}{4}\{|\alpha_j||\alpha_k||u_j||u_k|\sin\theta_j\sin\theta_k[(e^{2r} - 1)\sin\chi_j\sin\chi_k \\ &\quad - (1 - e^{-2r})\cos\chi_j\cos\chi_k] + (|\alpha_j|^2 + |u_j|^2\bar{n}_s)\delta_{jk}\} \\ &\quad + \tfrac{1}{4}|u_j|^2|u_k|^2(2c^2 - 1)s^2\cos\theta_j\cos\theta_k. \quad \text{(A40)}\end{aligned}$$

Here we have introduced the symbol $\chi_j = \phi_j - \varphi/2 + \delta_j$. Consider now Eq. (A24), rewritten for the specific choice $\hat{X}_j \equiv (\hat{J}_z)_j$:

$$\begin{aligned}\boldsymbol{G}_{jk} &= \frac{\partial\langle\Psi(\boldsymbol{\theta})|(\hat{J}_z)_j|\Psi(\boldsymbol{\theta})\rangle}{\partial\theta_k} \\ &= \frac{1}{2}\frac{\partial\langle\Psi(\boldsymbol{\theta})|(\hat{n}_j - \hat{n}_{j+d})|\Psi(\boldsymbol{\theta})\rangle}{\partial\theta_j}\delta_{jk}, \qquad j, k = 1, \ldots, d. \quad \text{(A41)}\end{aligned}$$

A formula for the evaluation of $\langle\Psi(\boldsymbol{\theta})|\hat{n}_j|\Psi(\boldsymbol{\theta})\rangle$ was derived in Eq. (A19): $\langle\Psi(\boldsymbol{\theta})|\hat{n}_j|\Psi(\boldsymbol{\theta})\rangle = -1 + \boldsymbol{E}_{jj} + \boldsymbol{\gamma}_j\boldsymbol{\gamma}_j^*$ for $j = 1,\ldots,2d$. The same information is conveniently condensed in the (diagonal) matrix $-\boldsymbol{I}_{2d} + (\boldsymbol{E} + \boldsymbol{\gamma}\boldsymbol{\gamma}^\dagger)\circ\boldsymbol{I}_{2d}$, whose diagonal elements are the $\langle\Psi(\boldsymbol{\theta})|\hat{n}_j|\Psi(\boldsymbol{\theta})\rangle$, $j = 1,\ldots,2d$.

Making use of Eqs. (A33) and (A36), one finds

$$-\boldsymbol{I}_{2d} + (\boldsymbol{E} + \boldsymbol{\gamma}\boldsymbol{\gamma}^\dagger)\circ\boldsymbol{I}_{2d} = \begin{pmatrix} -\boldsymbol{I}_d + \tilde{\boldsymbol{C}}^2 + (\tilde{\boldsymbol{S}}\boldsymbol{E}_1\tilde{\boldsymbol{S}})\circ\boldsymbol{I}_d + \tilde{\boldsymbol{C}}\boldsymbol{\phi}\_\tilde{\boldsymbol{C}} & 0 \\ 0 & -\boldsymbol{I}_d + \tilde{\boldsymbol{S}}^2 + (\tilde{\boldsymbol{C}}\boldsymbol{E}_1\tilde{\boldsymbol{C}})\circ\boldsymbol{I}_d + \tilde{\boldsymbol{S}}\boldsymbol{\phi}\_\tilde{\boldsymbol{S}} \end{pmatrix} \times \begin{pmatrix} -\boldsymbol{I}_d + \tilde{\boldsymbol{C}}^2 + \tilde{\boldsymbol{S}}^2(\boldsymbol{E}_1\circ\boldsymbol{I}_d) + \tilde{\boldsymbol{C}}\boldsymbol{\phi}\_\tilde{\boldsymbol{C}} & 0 \\ 0 & -\boldsymbol{I}_d + \tilde{\boldsymbol{S}}^2 + \tilde{\boldsymbol{C}}^2(\boldsymbol{E}_1\circ\boldsymbol{I}_d) + \tilde{\boldsymbol{S}}\boldsymbol{\phi}\_\tilde{\boldsymbol{S}} \end{pmatrix},$$

where the general result $(\boldsymbol{ZYZ})\circ\boldsymbol{I}_d = \boldsymbol{Z}^2(\boldsymbol{Y}\circ\boldsymbol{I}_d)$ has been used, $\boldsymbol{Z}$ being a diagonal matrix. Note that, for $j = 1,\ldots,d$, the expectation value $\langle\Psi(\boldsymbol{\theta})|(\hat{n}_j - \hat{n}_{j+d})|\Psi(\boldsymbol{\theta})\rangle$ corresponds to the difference between the two diagonal blocks of this matrix, so that, after simple algebraic manipulation, we get

$$\boldsymbol{G}_{jk} = \frac{1}{2}\frac{\partial\langle\Psi(\boldsymbol{\theta})|(\hat{n}_j - \hat{n}_{j+d})|\Psi(\boldsymbol{\theta})\rangle}{\partial\theta_j}\delta_{jk} = \frac{1}{2}\sin\theta_j[|u_j|^2 s^2 - |\alpha_j|^2]\delta_{jk}. \tag{A42}$$

At this point, if we aimed to obtain the explicit expression of the moment matrix, we would still have to compute the inverse matrix $\boldsymbol{\Gamma}^{-1}$. On the other hand, we only need $\boldsymbol{G}^{-1}$ to derive $\boldsymbol{M}^{-1} = (\boldsymbol{G}^{-1})^T\boldsymbol{\Gamma}\boldsymbol{G}^{-1}$, the advantage being that $\boldsymbol{G}$ is diagonal and thus is easily inverted. From Eqs. (A40) and (A42), one readily gets

$$\begin{aligned}(\boldsymbol{M}^{-1})_{jk} = |\alpha_j||\alpha_k||u_j||u_k|\Bigg[&(e^{2r}-1)\frac{\sin\chi_j}{|\alpha_j|^2 - |u_j|^2\bar{n}_s}\frac{\sin\chi_k}{|\alpha_k|^2 - |u_k|^2\bar{n}_s} - (1-e^{-2r})\frac{\cos\chi_j}{|\alpha_j|^2 - |u_j|^2\bar{n}_s}\frac{\cos\chi_k}{|\alpha_k|^2 - |u_k|^2\bar{n}_s}\Bigg] \\ &+ \frac{|\alpha_j|^2 + |u_j|^2\bar{n}_s}{(|\alpha_j|^2 - |u_j|^2\bar{n}_s)^2}\delta_{jk} + \frac{|\alpha_j|^2 + |u_j|^2\bar{n}_s}{(|\alpha_j|^2 - |u_j|^2\bar{n}_s)^2}\cot^2\theta_j\,\delta_{jk} + (2\bar{n}_s+1)\bar{n}_s|u_j|^2|u_k|^2\frac{\cot\theta_j}{|\alpha_j|^2 - |u_j|^2\bar{n}_s}\frac{\cot\theta_k}{|\alpha_k|^2 - |u_k|^2\bar{n}_s},\end{aligned} \tag{A43}$$

where $s^2 \equiv \sinh^2 r = \bar{n}_s$. By plugging Eq. (A43) into $\Delta^2(\boldsymbol{v}\cdot\boldsymbol{\theta})_{\rm em} = \boldsymbol{v}^T\boldsymbol{\mathcal{M}}^{-1}\boldsymbol{v}$, we obtain

$$\begin{aligned}\Delta^2(\boldsymbol{v}\cdot\boldsymbol{\theta})_{\rm em} = &(e^{2r}-1)\left(\sum_{j=1}^d \frac{|\alpha_j||u_j|\sin\chi_j}{|\alpha_j|^2 - |u_j|^2\bar{n}_s}v_j\right)^2 - (1-e^{-2r})\left(\sum_{j=1}^d \frac{|\alpha_j||u_j|\cos\chi_j}{|\alpha_j|^2 - |u_j|^2\bar{n}_s}v_j\right)^2 + \sum_{j=1}^d \frac{|\alpha_j|^2 + |u_j|^2\bar{n}_s}{(|\alpha_j|^2 - |u_j|^2\bar{n}_s)^2}v_j^2 \\ &+ \sum_{j=1}^d \cot^2\theta_j\frac{|\alpha_j|^2 + |u_j|^2\bar{n}_s}{(|\alpha_j|^2 - |u_j|^2\bar{n}_s)^2}v_j^2 + (2\bar{n}_s+1)\bar{n}_s\left(\sum_{j=1}^d \cot\theta_j\frac{|u_j|^2}{|\alpha_j|^2 - |u_j|^2\bar{n}_s}v_j\right)^2.\end{aligned} \tag{A44}$$

We can write $\Delta^2(\boldsymbol{v}\cdot\boldsymbol{\theta})_{\rm em} = \Delta^2(\boldsymbol{v}\cdot\boldsymbol{\theta})_{\rm em}|_{\theta_1 = \ldots = \theta_d = \pi/2} + \mathcal{Q}(\cot\theta_1,\ldots,\cot\theta_d)$, where $\mathcal{Q}$ is a second-degree polynomial in the variables $\cot\theta_1,\ldots,\cot\theta_d$ such that $Q = 0$ at $\theta_1 = \cdots = \theta_d = \pi/2$. Since $\mathcal{Q} \geqslant 0$ for all values of $\theta_1,\ldots,\theta_d$, the condition

$$\theta_j = \frac{\pi}{2}, \quad j = 1,\ldots,d \tag{A45}$$

identifies the optimal working point of the scheme, i.e., the point, among all possible values of $\theta_1,\ldots,\theta_d$, at which the estimation uncertainty is the smallest. In a similar way, we can minimize the uncertainty with respect to the parameters $\chi_1,\ldots,\chi_d$. As $\mathcal{Q}(\cot\theta_1,\ldots,\cot\theta_d)$ is independent of these parameters, we focus on $\Delta^2(\boldsymbol{v}\cdot\boldsymbol{\theta})_{\rm em}|_{\theta_1 = \ldots = \theta_d = \pi/2}$. By setting

$$\sin\chi_j = 0, \quad j = 1,\ldots,d, \tag{A46}$$

we minimize the first squared term in Eq. (A44) and *simultaneously* maximize the second one by a suitable choice of sign for $\cos\chi_j = \pm 1$, $j = 1,\ldots,d$. To maximize the second squared term in Eq. (A44), a sum of terms of equal sign is expected between round brackets, providing a criterion for the correct choice of sign. Overall this yields the absolute minimum of $\Delta^2(\boldsymbol{v}\cdot\boldsymbol{\theta})_{\rm em}$ with respect to $\chi_1,\ldots,\chi_d$. In the following, we will set $|u_j|\cos\chi_j = \pm|u_j| \equiv \tilde{u}_j$. At the optimal working point $\theta_j = \pi/2$ and applying the optimal condition $\sin\chi_j = 0$ to the phases of the input states, the sensitivity equation simplifies to Eq. (7). The optimal choice of sign for the cosine terms $\cos\chi_j = \pm 1$ is now embedded in the more general problem of optimizing the sensitivity with respect to the QC parameters $\{\tilde{u}_j\}_{j=1,\ldots,d}$.

c. Quantum Fisher information matrix and quantum Cramér-Rao bound

The derivation of the QFIM follows closely that of the inverse moment matrix, reported above. If a system is in the pure state $|\Psi\rangle$ and subject to a phase-encoding transformation of the form $\otimes_{j=1}^d e^{-i\theta_j(\hat{J}_z)_j}$, the elements of the QFIM can be calculated as

$$(\boldsymbol{\mathcal{F}}_{\mathbf{Q}})_{jk} = 4[\langle\Psi|(\hat{J}_z)_j(\hat{J}_z)_k|\Psi\rangle - \langle\Psi|(\hat{J}_z)_j|\Psi\rangle\langle\Psi|(\hat{J}_z)_k|\Psi\rangle]. \tag{A47}$$

To make use of this equation, we notice that, in our scheme, encoding the phases in the state $|\Psi_{\text{out}}\rangle$ through the unitary transformation $\otimes_{j=1}^{d} e^{-i\theta_j(\hat{J}_y)_j}$, as assumed in the previous section, is equivalent to encoding them in the state $|\Psi\rangle = \otimes_{j=1}^{d} e^{-i\frac{\pi}{2}(\hat{J}_x)_j}|\Psi_{\text{out}}\rangle$, where $(\hat{J}_x)_j = (\hat{a}_j^\dagger \hat{b}_j + \hat{b}_j^\dagger \hat{a}_j)/2$, through the unitary transformation $\otimes_{j=1}^{d} e^{-i\theta_j(\hat{J}_z)_j}$, with $(\hat{J}_z)_j = (\hat{a}_j^\dagger \hat{a}_j - \hat{b}_j^\dagger \hat{b}_j)/2$. This alternative formulation is more convenient here. Overall, $|\Psi\rangle$ can be expressed as

$$|\Psi\rangle = \left(\otimes_{j=1}^{d} e^{-i\frac{\pi}{2}(\hat{J}_x)_j}\right)\hat{U}^\dagger|\Psi_{\text{out}}\rangle.$$

Therefore, this time we have $\hat{A}^\dagger = (\otimes_{j=1}^{d} e^{-i\frac{\pi}{2}(\hat{J}_x)_j})\hat{U}^\dagger$ or, in matrix form:

$$\begin{aligned} \boldsymbol{A}^\dagger &= \frac{1}{\sqrt{2}}\begin{pmatrix} \boldsymbol{I}_d & -i\boldsymbol{I}_d \\ -i\boldsymbol{I}_d & \boldsymbol{I}_d \end{pmatrix}\begin{pmatrix} \boldsymbol{I}_d & 0 \\ 0 & \boldsymbol{U}_{\text{QC}}^\dagger \end{pmatrix} \\ &= \frac{1}{\sqrt{2}}\begin{pmatrix} \boldsymbol{I}_d & -i\boldsymbol{U}_{\text{QC}}^\dagger \\ -i\boldsymbol{I}_d & \boldsymbol{U}_{\text{QC}}^\dagger \end{pmatrix}. \end{aligned} \tag{A48}$$

Similarly to what has been done for $\boldsymbol{\mathcal{M}}^{-1}$, we can express $(\boldsymbol{\mathcal{F}}_{\mathbf{Q}})_{jk}$ as

$$\begin{aligned} (\boldsymbol{\mathcal{F}}_{\mathbf{Q}})_{jk} &= \boldsymbol{h}_{j,k} + \boldsymbol{h}_{j+d,k+d} - \boldsymbol{h}_{j,k+d} - \boldsymbol{h}_{j+d,k}, \\ & j,k = 1,\ldots,d, \end{aligned} \tag{A49}$$

where $\boldsymbol{h}_{jk} = \langle\Psi|\hat{n}_j\hat{n}_k|\Psi\rangle - \langle\Psi|\hat{n}_j|\Psi\rangle\langle\Psi|\hat{n}_k|\Psi\rangle$. The old expressions of $\boldsymbol{E}$, $\boldsymbol{EN}$, and $\boldsymbol{\gamma}$, Eqs. (A33) to (A35), will change according to the change in the evolution operator $\boldsymbol{A}^\dagger$, Eq. (A48):

$$\boldsymbol{E} = \boldsymbol{A}^\dagger\boldsymbol{C}\boldsymbol{A} = \tfrac{1}{2}\begin{pmatrix} \boldsymbol{I}_d + \boldsymbol{E_1} & i(\boldsymbol{I}_d - \boldsymbol{E_1}) \\ -i(\boldsymbol{I}_d - \boldsymbol{E_1}) & \boldsymbol{I}_d + \boldsymbol{E_1} \end{pmatrix},$$

$$\boldsymbol{EN} = \boldsymbol{A}^\dagger\boldsymbol{C}\boldsymbol{D}\boldsymbol{A}^* = \tfrac{1}{2}\begin{pmatrix} -\boldsymbol{E_1}\boldsymbol{N_1} & -i\boldsymbol{E_1}\boldsymbol{N_1} \\ -i\boldsymbol{E_1}\boldsymbol{N_1} & \boldsymbol{E_1}\boldsymbol{N_1} \end{pmatrix},$$

$$\boldsymbol{\gamma} = \frac{1}{\sqrt{2}}\begin{pmatrix} \boldsymbol{\beta_0}^* \\ i\boldsymbol{\beta_0}^* \end{pmatrix} = \frac{1}{\sqrt{2}}\begin{pmatrix} \boldsymbol{\gamma_0} \\ i\boldsymbol{\gamma_0} \end{pmatrix}.$$

However, notice that Eqs. (A38) and (A39) for $\boldsymbol{E_1}\boldsymbol{N_1}$ and $\boldsymbol{E_1}$ and the expression of $\boldsymbol{\beta_0}$ are left unaltered. We then derive matrix $\boldsymbol{h}$ by making use of Eq. (A22), and, finally, from Eq. (A49), we find

$$\begin{aligned} (\boldsymbol{\mathcal{F}}_{\mathbf{Q}})_{jk} &= |\alpha_j||\alpha_k|[(e^{-i\varphi}u_j e^{i\phi_j}u_k e^{i\phi_k} + e^{i\varphi}u_j^* e^{-i\phi_j}u_k^* e^{-i\phi_k})sc \\ &\quad + (u_j^* e^{-i\phi_j}u_k e^{i\phi_k} + u_j e^{i\phi_j}u_k^* e^{-i\phi_k})s^2 + \delta_{jk}] + |u_j|^2 s^2\delta_{jk} \\ &= |\alpha_j||\alpha_k||u_j||u_k|[(e^{2r}-1)\cos\chi_j\cos\chi_k \\ &\quad - (1-e^{-2r})\sin\chi_j\sin\chi_k] + (|\alpha_j|^2 + |u_k|^2\bar{n}_s)\delta_{jk}. \end{aligned} \tag{A50}$$

The QFIM derived in Eq. (A50) does not depend on the phases $\theta_1,\ldots,\theta_d$ to be estimated. However, it still needs to be optimized with respect to the parameters $\{\chi_j\}_{j=1,\ldots,d}$. Since, unlike the case of Eq. (A44), a simple expression for $\boldsymbol{v}^T\boldsymbol{\mathcal{F}_Q}^{-1}\boldsymbol{v}$ is not available, we here assume that the optimal condition $\sin\chi_j = 0$ derived for $\boldsymbol{v}^T\boldsymbol{\mathcal{M}}^{-1}\boldsymbol{v}$ still holds for the present case. By applying that to Eq. (A50), we find

$$(\boldsymbol{\mathcal{F}}_{\mathbf{Q}})_{jk} = (e^{2r}-1)|\alpha_j||\alpha_k|\tilde{u}_j\tilde{u}_k + \left(|\alpha_j|^2 + \tilde{u}_j^2\bar{n}_s\right)\delta_{jk}. \tag{A51}$$

To obtain the quantum Cramér-Rao bound, we first use the Sherman-Morrison formula to invert the above equation:

$$\begin{aligned} (\boldsymbol{\mathcal{F}}_{\mathbf{Q}}{}^{-1})_{jk} &= \frac{1}{|\alpha_j|^2 + \tilde{u}_j^2\bar{n}_s}\delta_{jk} - \frac{(e^{2r}-1)}{1+\mathcal{K}(e^{2r}-1)} \\ &\quad \times \frac{|\alpha_j||\alpha_k|\tilde{u}_j\tilde{u}_k}{\left(|\alpha_j|^2 + \tilde{u}_j^2\bar{n}_s\right)\left(|\alpha_k|^2 + \tilde{u}_k^2\bar{n}_s\right)}, \end{aligned} \tag{A52}$$

where $\mathcal{K} = \sum_{j=1}^{d}|\alpha_j|^2\tilde{u}_j^2/(|\alpha_j|^2 + \tilde{u}_j^2\bar{n}_s)$. Finally, the QCRB of Eq. (8) is derived by making use of $\Delta^2(\boldsymbol{v}\cdot\boldsymbol{\theta})_{\text{eQ}} = \boldsymbol{v}^T\boldsymbol{\mathcal{F}_Q}^{-1}\boldsymbol{v}$.

2. Optimized sensitivities

a. Derivation of Eq. (17)

Our starting point is Eq. (7). Taking

$$|\alpha_j|^2 \gg \tilde{u}_j^2\bar{n}_s \tag{A53}$$

for all j, we can simplify the denominator of all terms in the equation, obtaining

$$\begin{aligned} \Delta^2(\boldsymbol{v}\cdot\boldsymbol{\theta})_{\text{em}} &= -\left(\sum_{j=1}^{d}\tilde{u}_j\frac{v_j}{|\alpha_j|}\right)^2 + e^{-2r}\left(\sum_{j=1}^{d}\tilde{u}_j\frac{v_j}{|\alpha_j|}\right)^2 \\ &\quad + \sum_{j=1}^{d}\frac{v_j^2}{|\alpha_j|^2} + \sum_{j=1}^{d}\frac{\tilde{u}_j^2 v_j^2}{|\alpha_j|^4}\bar{n}_s. \end{aligned} \tag{A54}$$

To proceed with the optimization, we want to neglect the last terms with respect to the others. Taking into account Eq. (A53) and the further condition

$$e^{-2r}\left(\sum_{j=1}^{d}\tilde{u}_j\frac{v_j}{|\alpha_j|}\right)^2 \gg \sum_{j=1}^{d}\frac{\tilde{u}_j^2 v_j^2}{|\alpha_j|^4}\bar{n}_s \tag{A55}$$

allows us to simplify Eq. (7) to

$$\Delta^2(\boldsymbol{v}\cdot\boldsymbol{\theta})_{\text{em}} = -(1-e^{-2r})\left(\sum_{j=1}^{d}\tilde{u}_j\frac{v_j}{|\alpha_j|}\right)^2 + \sum_{j=1}^{d}\frac{v_j^2}{|\alpha_j|^2}. \tag{A56}$$

We recognize that the first terms writes as a scalar product: it can be minimized by taking $\tilde{u}_i \propto v_i/|\alpha_i|$, which gives

$$\min_{\tilde{\boldsymbol{u}}}\Delta^2(\boldsymbol{v}\cdot\boldsymbol{\theta})_{\text{em}} = \left(\sum_{j=1}^{d}\frac{v_i^2}{|\alpha_j|^2}\right)e^{-2r}. \tag{A57}$$

For the optimization over the coherent state intensities, $(\bar{n}_c)_j = |\alpha_j|^2$, we rely on the method of Lagrangiam multipliers. The derivative of the Lagrangian function $\mathcal{L}[(\bar{n}_c)_k,\lambda]$ associated with the minimization of Eq. (A57) under the constraint $\sum_{j=1}^{d}(\bar{n}_c)_j = d\bar{n}_c$ is

$$\frac{\partial}{\partial(\bar{n}_c)_j}\mathcal{L}[(\bar{n}_c)_k,\lambda] = -\frac{v_j^2}{(\bar{n}_c)_j^2}e^{-2r} - \lambda. \tag{A58}$$

Setting this to zero, we find that the first term on the right-hand side of the above equation equals λ for all j. We have

$$\frac{|v_{j+1}|}{(\bar{n}_c)_{j+1}} = \frac{|v_j|}{(\bar{n}_c)_j}, \tag{A59}$$

for $j = 1, \ldots, d-1$. Making use of the constraint on the total number of coherent photons, we obtain the optimal parameters $(\bar{n}_c)_j$ and $\tilde{u}_j$ given in Eq. (13). By replacing these parameters into Eq. (A57), we recover Eq. (17). Finally, using the above optimal parameters, we obtain that Eq. (A53) is satisfied for $\bar{n}_T \gg 2\bar{n}_s$ and Eq. (A55) is satisfied for the more restrictive $\bar{n}_T \gg (e^{2r}+1)\bar{n}_s$.

b. Derivation of Eq. (23)

Under the condition $|\alpha_j|^2 \gg \tilde{u}_j^2 \bar{n}_s$, one can make the approximation $|\alpha_j|^2 + \tilde{u}_j^2 \bar{n}_s \approx |\alpha_j|^2$ and simplify the denominators of Eq. (A52). The quantity $\mathcal{K}$ appearing in the same equation also simplifies, as $\mathcal{K} \approx 1$. The QCRB derived from this approximated form of $\mathcal{F}_{\mathbf{Q}}^{-1}$ coincides with Eq. (A56). Therefore, the optimization performed on $\Delta^2(\boldsymbol{v}\cdot\boldsymbol{\theta})_{\mathrm{em}}$ also works for $\Delta^2(\boldsymbol{v}\cdot\boldsymbol{\theta})_{\mathrm{eQ}}$. However, only the assumption $|\alpha_j|^2 \gg \tilde{u}_j^2\bar{n}_s$ is needed in this case. Therefore, the result must hold in the wider regime $\bar{n}_T \gg 2\bar{n}_s$.

c. Derivation of Eq. (27)

The starting point is Eq. (9). Taking $(\bar{n}'_c)_j \gg (\bar{n}'_s)_j$ for all j allows us to simplify the denominator of Eq. (9), giving

$$\Delta^2(\boldsymbol{v}\cdot\boldsymbol{\theta})_{\mathrm{sm}} = \sum_{j=1}^{d}\left(\frac{e^{-2r'_j}}{(\bar{n}'_c)_j} + \frac{(\bar{n}'_s)_j}{(\bar{n}'_c)_j^2}\right)v_j^2. \tag{A60}$$

In the limit,

$$(\bar{n}'_c)_j \gg (\bar{n}'_s)_j e^{2r'_j} \tag{A61}$$

the above equation reduces to

$$\Delta^2(\boldsymbol{v}\cdot\boldsymbol{\theta})_{\mathrm{sm}} = \sum_{j=1}^{d}\frac{e^{-2r'_j}}{(\bar{n}'_c)_j}v_j^2. \tag{A62}$$

To minimize this equation with respect to all r'_j under the constraint $\sum_{j=1}^d (\bar{n}'_s)_j = \sum_{j=1}^d \sinh^2 r'_j = \bar{n}'_s$, we further assume $r'_j \gg 1$, so that $e^{-2r'_j} \approx 1/[4(\bar{n}'_s)_j]$. Using the method of Lagrange multipliers we obtain

$$\min_{\{r'_j\}} \Delta^2(\boldsymbol{v}\cdot\boldsymbol{\theta})_{\mathrm{sm}} = e^{-2r}\left(\sum_{j=1}^{d}\frac{|v_j|}{|\alpha'_j|}\right)^2, \tag{A63}$$

which is achieved for

$$(\bar{n}'_s)_j = \bar{n}_s \frac{|v_j|/|\alpha'_j|}{\sum_{k=1}^d |v_k|/|\alpha'_k|}, \tag{A64}$$

where $|\alpha'_j| = \sqrt{(\bar{n}'_c)_j}$. Next, we minimize Eq. (A63) with respect to all the amplitudes $|\alpha'_j|$ under the constraint $\sum_{j=1}^d |\alpha'_j|^2 = d\bar{n}'_c$. The derivative of the Lagrangian function $\mathcal{L}[|\alpha'_k|, \lambda]$ is

$$\frac{\partial}{\partial|\alpha'_j|}\mathcal{L}[|\alpha'_k|,\lambda] = -2\left(\sum_{k=1}^{d}\frac{|v_k|}{|\alpha'_k|}\right)\frac{|v_j|}{|\alpha'_j|^2} - 2\lambda|\alpha'_j|. \tag{A65}$$

We set the derivative to zero, assume $|\alpha'_j| \neq 0$ and divide by $|\alpha'_j|$, getting

$$\lambda = -\left(\sum_{k=1}^{d}\frac{|v_k|}{|\alpha'_k|}\right)\frac{|v_j|}{|\alpha'_j|^3}. \tag{A66}$$

The right-hand side must be constant for $j = 1, \ldots, d$. This implies

$$\frac{|v_{j+1}|^{2/3}}{(\bar{n}'_c)^{\mathrm{opt}}_{j+1}} = \frac{|v_j|^{2/3}}{(\bar{n}'_c)^{\mathrm{opt}}_{j}}, \tag{A67}$$

with $j = 1, \ldots, d-1$, from which, making use of the constraint on the total number of coherent photons, one obtain Eqs. (27) and (28). Finally, taking the optimal parameters $(\bar{n}'_c)_j$ and $(\bar{n}'_s)_j$, and approximating r'_j with its average value $r' = \mathrm{arcsinh}(\bar{n}_s/d)$, Eq. (A61) becomes $\bar{n}'_T \gg (e^{2r'}+1)\bar{n}'_s$.

For the QCRB, notice that, under the condition $|\alpha'_j|^2 \gg (\bar{n}'_s)_j$, Eq. (10) reduces to Eq. (A62), so the optimization of the QCRB immediately follows from the discussion above.

d. Derivation of Eq. (47)

$\mathcal{G}^{\mathrm{Q}}_{C_3}(\boldsymbol{v}, \bar{n}_s, \bar{n}_T)$ can be derived analytically in the regime $\bar{n}_T \gg 2\bar{n}_s$. In this regime, the QCRB of the entangled strategy is given by Eq. (A56). The optimal QCRB is also known, from Eq. (22). For what concerns the separable strategy, the expression to optimize is the one of Eq. (A62) where, according to the constraint C_3, one needs to set $r'_j = r$. We get

$$\Delta^2(\boldsymbol{v}\cdot\boldsymbol{\theta})_{\mathrm{sQ}} = \left(\sum_{j=1}^{d}\frac{v_j^2}{(\bar{n}'_c)_j}\right)e^{-2r},$$

which is, except for the primed particle numbers $(\bar{n}'_c)_j$, exactly the expression in Eq. (A57). Therefore, we get $\min_{|\alpha'_1|,\ldots,|\alpha'_d|}\Delta^2(\boldsymbol{v}\cdot\boldsymbol{\theta})_{\mathrm{sQ}} = \min_{|\alpha_1|,\ldots,|\alpha_d|,\hat{U}_{\mathrm{QC}}}\Delta^2(\boldsymbol{v}\cdot\boldsymbol{\theta})_{\mathrm{eQ}}$ and, thus, $\mathcal{G}^{\mathrm{Q}}_{C_3}(\boldsymbol{v}, \bar{n}_s, \bar{n}_T) = 1$, as stated in the main text.

e. Derivation of Eq. (12)

We will show here that the optimal conditions of Eqs. (13) can be substituted into Eq. (A54) to get the optimal entangled sensitivity, even in the regime $\bar{n}_T \gg 2\bar{n}_s$. To this aim, we compute the derivatives of the Lagrangian function associated with the minimization of Eq. (A54) under the two constraints $\sum_{j=1}^d \tilde{u}_j^2 = 1$ and $\sum_{j=1}^d |\alpha_j|^2 = d\bar{n}_c$:

$$\frac{\partial}{\partial\tilde{u}_j}\mathcal{L} = 2e^{-2r}\left(\sum_{k=1}^{d}\frac{\tilde{u}_k v_k}{|\alpha_k|}\right)\frac{v_j}{|\alpha_j|} + 2\bar{n}_s\left(\frac{\tilde{u}_j v_j^2}{|\alpha_j|^4}\right) - 2\lambda\tilde{u}_j, \tag{A68}$$

$$\frac{\partial}{\partial|\alpha_j|}\mathcal{L} = -2e^{-2r}\left(\sum_{k=1}^{d}\frac{\tilde{u}_k v_k}{|\alpha_k|}\right)\frac{\tilde{u}_j v_j}{|\alpha_j|^2} - 4\bar{n}_s\left(\frac{\tilde{u}_j^2 v_j^2}{|\alpha_j|^5}\right) - 2|\alpha_j|\mu, \tag{A69}$$

where $\mathcal{L} \equiv \mathcal{L}[\tilde{u}_k, |\alpha_k|, \lambda, \mu]$, λ and μ denoting the two Lagrangian multipliers. We get conditions for the minimum by setting the right-hand sides to zero. This way, we are left with $2d$ coupled equations. By direct substitution, we find that these are solved by Eqs. (13), with $\lambda = [e^{-2r}/(d\bar{n}_c) + \bar{n}_s/(d\bar{n}_c)^2](\sum_j |v_j|)^2$ and $\mu = -\lambda/(d\bar{n}_c)$.

3. Derivation of Eq. (21)

The lower bound in Eq. (21) is obtained by first using the Cauchy-Schwarz inequality,

$$\Delta^2(\boldsymbol{v}\cdot\boldsymbol{\theta})_{\rm eQ} = \boldsymbol{v}^T {\boldsymbol{\mathcal{F}}_{\mathbf{Q}}}^{-1} \boldsymbol{v} \geqslant \frac{|\boldsymbol{v}|^4}{(\boldsymbol{v}^T \boldsymbol{\mathcal{F}}_{\mathbf{Q}} \boldsymbol{v})}. \tag{A70}$$

From Eq. (A51) we then have

$$\boldsymbol{v}^T \boldsymbol{\mathcal{F}}_{\mathbf{Q}} \boldsymbol{v} = (e^{2r}-1)\left(\sum_{j=1}^{d} |\alpha_j| \tilde{u}_j v_j\right)^2 + \sum_{j=1}^{d} |\alpha_j|^2 v_j^2 + \bar{n}_s \sum_{j=1}^{d} \tilde{u}_j^2 v_j^2. \tag{A71}$$

We have

$$\left(\sum_{j=1}^{d} |\alpha_j| \tilde{u}_j v_j\right)^2 \leqslant \left(\sum_{j=1}^{d} v_j^2\right)\left(\sum_{j=1}^{d} |\alpha_j|^2 \tilde{u}_j^2\right) \leqslant \frac{\sum_{j=1}^{d} |\alpha_j|^2}{d},$$

where the first inequality is due to Cauchy-Schwarz and the second is a consequence of $\tilde{u}_j^2 \leqslant 1$ and $\sum_{j=1}^{d} v_j^2 = 1/d$. Using $v_j^2 \leqslant 1/d$, we also have

$$\sum_{j=1}^{d} |\alpha_j|^2 v_j^2 \leqslant \frac{\sum_{j=1}^{d} |\alpha_j|^2}{d}, \quad \text{and} \quad \sum_{j=1}^{d} \tilde{u}_j^2 v_j^2 \leqslant \frac{1}{d}. \tag{A72}$$

Combining Eq. (A71) with the above inequalities gives

$$\boldsymbol{v}^T \boldsymbol{\mathcal{F}}_{\mathbf{Q}} \boldsymbol{v} \leqslant \frac{e^{2r} \sum_{j=1}^{d} |\alpha_j|^2 + \bar{n}_s}{d}.$$

Taking into account that $\sum_{j=1}^{d} |\alpha_j|^2 = \bar{n}_T - \bar{n}_s$ and $|\boldsymbol{v}|^4 = 1/d^2$, from Eq. (A70), we obtain

$$\Delta^2(\boldsymbol{v}\cdot\boldsymbol{\theta})_{\rm eQ} \geqslant \frac{1}{d(d\bar{n}_c e^{2r} + \bar{n}_s)}. \tag{A73}$$

The lower bound is valid for all $\hat{U}_{\rm QC}$ and all $|\alpha_1|^2, \ldots, |\alpha_d|^2$ and thus also for the optimal configuration, giving Eq. (21).

Finally, the upper bound is obtained by replacing Eqs. (13) for $|\alpha_j|^2$ and $\tilde{u}_j$ into Eq. (8).

4. Effect of losses in particle detection

In order to include the effect of particle losses in our calculation we consider a new evolution matrix

$$\boldsymbol{A}^\dagger = \begin{pmatrix} \sqrt{\eta}\,\boldsymbol{I}_d & -\sqrt{1-\eta}\,\boldsymbol{I}_d & \boldsymbol{0} & \boldsymbol{0} \\ \sqrt{1-\eta}\,\boldsymbol{I}_d & \sqrt{\eta}\,\boldsymbol{I}_d & \boldsymbol{0} & \boldsymbol{0} \\ \boldsymbol{0} & \boldsymbol{0} & \sqrt{\eta}\,\boldsymbol{I}_d & -\sqrt{1-\eta}\,\boldsymbol{I}_d \\ \boldsymbol{0} & \boldsymbol{0} & \sqrt{1-\eta}\,\boldsymbol{I}_d & \sqrt{\eta}\,\boldsymbol{I}_d \end{pmatrix} \begin{pmatrix} \boldsymbol{I}_d & \boldsymbol{0} & \boldsymbol{0} & \boldsymbol{0} \\ \boldsymbol{0} & \tilde{\boldsymbol{C}} & \tilde{\boldsymbol{S}} & \boldsymbol{0} \\ \boldsymbol{0} & -\tilde{\boldsymbol{S}} & \tilde{\boldsymbol{C}} & \boldsymbol{0} \\ \boldsymbol{0} & \boldsymbol{0} & \boldsymbol{0} & \boldsymbol{I}_d \end{pmatrix} \begin{pmatrix} \boldsymbol{I}_d & \boldsymbol{0} & \boldsymbol{0} & \boldsymbol{0} \\ \boldsymbol{0} & \boldsymbol{I}_d & \boldsymbol{0} & \boldsymbol{0} \\ \boldsymbol{0} & \boldsymbol{0} & {\boldsymbol{A_1}}^\dagger & \boldsymbol{0} \\ \boldsymbol{0} & \boldsymbol{0} & \boldsymbol{0} & \boldsymbol{I}_d \end{pmatrix}$$

$$= \begin{pmatrix} \sqrt{\eta}\,\boldsymbol{I}_d & -\sqrt{1-\eta}\,\tilde{\boldsymbol{C}} & -\sqrt{1-\eta}\,\tilde{\boldsymbol{S}}{\boldsymbol{A_1}}^\dagger & \boldsymbol{0} \\ \sqrt{1-\eta}\,\boldsymbol{I}_d & \sqrt{\eta}\,\tilde{\boldsymbol{C}} & \sqrt{\eta}\,\tilde{\boldsymbol{S}}{\boldsymbol{A_1}}^\dagger & \boldsymbol{0} \\ \boldsymbol{0} & -\sqrt{\eta}\,\tilde{\boldsymbol{S}} & \sqrt{\eta}\,\tilde{\boldsymbol{C}}{\boldsymbol{A_1}}^\dagger & -\sqrt{1-\eta}\,\boldsymbol{I}_d \\ \boldsymbol{0} & -\sqrt{1-\eta}\,\tilde{\boldsymbol{S}} & \sqrt{1-\eta}\,\tilde{\boldsymbol{C}}{\boldsymbol{A_1}}^\dagger & \sqrt{\eta}\,\boldsymbol{I}_d \end{pmatrix}, \tag{A74}$$

which replaces the evolution matrix in Eq. (A26). The structure of the above matrix is the following: it consists of 4×4 blocks, each block corresponding to a $d \times d$ smaller matrix; the four inner blocks are relative to modes which describe particles traveling along the interferometer, while the outer ones correspond to the vacuum modes just introduced to take care of possible particle losses. The inverse moment matrix can be derived, as above, through the relation $\boldsymbol{M}^{-1} = (\boldsymbol{G}^{-1})^T \boldsymbol{\Gamma} \boldsymbol{G}^{-1}$. We refer to Eq. (A28) to find the expression of $\boldsymbol{\Gamma}$, which, in turn, requires the evaluation of matrix $\boldsymbol{h}$, Eq. (A22). None of the angular momentum operators involved in the definition of $\boldsymbol{\Gamma}$, Eq. (A27), contains the loss vacuum modes, so that, when averaging on the output state, we effectively trace on those modes. This brings about a simplification in the evaluation of $\boldsymbol{\Gamma}$, that is, one needs only to derive the four inner blocks of matrix $\boldsymbol{h}$, while the outer blocks can be safely disregarded. Equations (A33)–(A37) thus become

$$(\boldsymbol{E})_{\rm innerblocks} = \begin{pmatrix} (1-\eta)\boldsymbol{I}_d + \eta(\tilde{\boldsymbol{C}}^2 + \tilde{\boldsymbol{S}}\boldsymbol{E_1}\tilde{\boldsymbol{S}}) & -\eta(\tilde{\boldsymbol{S}}\tilde{\boldsymbol{C}} - \tilde{\boldsymbol{S}}\boldsymbol{E_1}\tilde{\boldsymbol{C}}) \\ -\eta(\tilde{\boldsymbol{S}}\tilde{\boldsymbol{C}} - \tilde{\boldsymbol{C}}\boldsymbol{E_1}\tilde{\boldsymbol{S}}) & (1-\eta)\boldsymbol{I}_d + \eta(\tilde{\boldsymbol{S}}^2 + \tilde{\boldsymbol{C}}\boldsymbol{E_1}\tilde{\boldsymbol{C}}) \end{pmatrix}, \tag{A75}$$

$$(\boldsymbol{EN})_{\rm innerblocks} = \eta \begin{pmatrix} \tilde{\boldsymbol{S}}\boldsymbol{E_1}\boldsymbol{N_1}\tilde{\boldsymbol{S}} & \tilde{\boldsymbol{S}}\boldsymbol{E_1}\boldsymbol{N_1}\tilde{\boldsymbol{C}} \\ \tilde{\boldsymbol{C}}\boldsymbol{E_1}\boldsymbol{N_1}\tilde{\boldsymbol{S}} & \tilde{\boldsymbol{C}}\boldsymbol{E_1}\boldsymbol{N_1}\tilde{\boldsymbol{C}} \end{pmatrix}, \tag{A76}$$

$$(\boldsymbol{\gamma\gamma}^\dagger)_{\rm innerblocks} = \eta \begin{pmatrix} \tilde{\boldsymbol{C}}\boldsymbol{\phi_-}\tilde{\boldsymbol{C}} & -\tilde{\boldsymbol{C}}\boldsymbol{\phi_-}\tilde{\boldsymbol{S}} \\ -\tilde{\boldsymbol{S}}\boldsymbol{\phi_-}\tilde{\boldsymbol{C}} & \tilde{\boldsymbol{S}}\boldsymbol{\phi_-}\tilde{\boldsymbol{S}} \end{pmatrix}, \tag{A77}$$

$$(\boldsymbol{\gamma\gamma}^T)_{\rm innerblocks} = \eta \begin{pmatrix} \tilde{\boldsymbol{C}}\boldsymbol{\phi_+}\tilde{\boldsymbol{C}} & -\tilde{\boldsymbol{C}}\boldsymbol{\phi_+}\tilde{\boldsymbol{S}} \\ -\tilde{\boldsymbol{S}}\boldsymbol{\phi_+}\tilde{\boldsymbol{C}} & \tilde{\boldsymbol{S}}\boldsymbol{\phi_+}\tilde{\boldsymbol{S}} \end{pmatrix}. \tag{A78}$$

The expression of $\boldsymbol{\Gamma}$ obtained from the new matrices is $\boldsymbol{\Gamma}_{ij} = \eta^2[\boldsymbol{\Gamma}_{ij}]_{\eta=1} + \frac{1}{4}\eta(1-\eta)(|\alpha_i|^2 + |u_i|^2 s^2)\delta_{ij}$. We also easily find $\boldsymbol{G}_{ij} = \eta[\boldsymbol{G}_{ij}]_{\eta=1}$. Therefore, applying $\boldsymbol{M}^{-1} = (\boldsymbol{G}^{-1})^T \boldsymbol{\Gamma} \boldsymbol{G}^{-1}$ we obtain our final expression for the inverse moment matrix,

$$(\boldsymbol{M}^{-1})_{ij} = [(\boldsymbol{M}^{-1})_{ij}]_{\eta=1} + \frac{1-\eta}{\eta} \frac{|\alpha_i|^2 + |u_i|^2 \bar{n}_s}{(|\alpha_i|^2 - |u_i|^2 \bar{n}_s)^2} (1 + \cot^2 \theta_i)\delta_{ij}, \tag{A79}$$

from which we recover Eq. (55), using $\Delta^2(\boldsymbol{v}\cdot\boldsymbol{\theta})_{\mathrm{em}} = \boldsymbol{v}^T \boldsymbol{M}^{-1} \boldsymbol{v}$.

5. Proof of Eqs. (57) and (58)

Let us demonstrate Eq. (57): the demonstration of Eq. (58) is analogous. Equation (57) is a direct consequence of

$$\Delta^2(\boldsymbol{v}\cdot\boldsymbol{\theta})_{\mathrm{em}} = \boldsymbol{v}^T \boldsymbol{\mathcal{M}}^{-1} \boldsymbol{v} \geqslant |\boldsymbol{v}|^4 / \boldsymbol{v}^T \boldsymbol{\mathcal{M}} \boldsymbol{v}, \tag{A80}$$

$\boldsymbol{v}^T \boldsymbol{\mathcal{M}} \boldsymbol{v} \leqslant \boldsymbol{v}_{\mu_{\max}}^T \boldsymbol{\mathcal{M}} \boldsymbol{v}_{\mu_{\max}} = \mu_{\max}$ and $|\boldsymbol{v}|^2 = 1/d$. These imply the bound $\Delta^2(\boldsymbol{v}\cdot\boldsymbol{\theta})_{\mathrm{em}} \geqslant 1/(\mu_{\max} d)$, which is saturable for $\boldsymbol{v}/|\boldsymbol{v}| = \boldsymbol{v}_{\mu_{\max}}$. The inequality (A80) follows from the Cauchy-Schwarz inequality $(\boldsymbol{f}^T \boldsymbol{f})(\boldsymbol{g}^T \boldsymbol{g}) \geqslant (\boldsymbol{f}^T \boldsymbol{g})^2$ with $\boldsymbol{f} = \boldsymbol{\mathcal{M}}^{1/2} \boldsymbol{v}$ and $\boldsymbol{g} = \boldsymbol{\mathcal{M}}^{-1/2} \boldsymbol{v}$ and is saturated if and only if $\boldsymbol{f} = \lambda \boldsymbol{g}$ for some real number λ, namely, if and only if $\boldsymbol{v}$ is an eigenvector of $\boldsymbol{\mathcal{M}}$. Note that $\boldsymbol{\mathcal{M}}^{1/2}$ is well definite since $\boldsymbol{\mathcal{M}} \geqslant 0$: this follows from $\boldsymbol{\mathcal{M}} = \boldsymbol{C}^T \boldsymbol{\Gamma}^{-1} \boldsymbol{C}$, $\boldsymbol{\Gamma} \geqslant 0$ being a covariance matrix, and $\boldsymbol{\Gamma}^{-1} \geqslant 0$ being the inverse of a positive semidefinite matrix.

[1] R. Loudon and P. R. Knight, Squeezed light, J. Mod. Opt. **34**, 709 (1987).

[2] M. O. Scully and M. S. Zubairy, *Quantum Optics* (Cambridge University Press, Cambridge, 1987); D. F. Walls and G. J. Milburn, *Quantum Optics* (Springer-Verlag, Berlin, 1994).

[3] G. Breitenbach, S. Schiller, and J. Mlynek, Measurement of the quantum states of squeezed light, Nature (London) **387**, 471 (1997).

[4] U. L. Andersen, T. Gehring, C. Marquardt, and G. Leuchs, 30 years of squeezed light generation, Phys. Scr. **91**, 053001 (2016).

[5] C. M. Caves, Quantum mechanical noise in an interferometer, Phys. Rev. D **23**, 1693 (1981).

[6] M. G. A. Paris, Small amount of squeezing in high-sensitive realistic interferometry, Phys. Lett. A **201**, 132 (1995).

[7] S. M. Barnett, C. Fabre, and A. Maitre, Ultimate quantum limits for resolution of beam displacements, Eur. Phys. J. D **22**, 513 (2003).

[8] L. Pezzè and A. Smerzi, Mach-Zehnder Interferometry at the Heisenberg Limit with Coherent and Squeezed-Vacuum Light, Phys. Rev. Lett. **100**, 073601 (2008).

[9] M. D. Lang and C. M. Caves, Optimal Quantum-Enhanced Interferometry Using a Laser Power Source, Phys. Rev. Lett. **111**, 173601 (2013).

[10] I. Ruo-Berchera, I. P. Degiovanni, S. Olivares, N. Samantaray, P. Traina, and M. Genovese, One- and two-mode squeezed light in correlated interferometry Phys. Rev. A **92**, 053821 (2015).

[11] C. Sparaciari, S. Olivares, and M. G. A. Paris, Gaussian state interferometry with passive and active elements, Phys. Rev. A **93**, 023810 (2016).

[12] R. S. Bondurant and J. H. Shapiro, Squeezed states in phase-sensing interferometers, Phys. Rev. D **30**, 2548 (1984).

[13] L.-A. Wu, H. Kimble, J. Hall, and H. Wu, Generation of Squeezed States by Parametric Down Conversion, Phys. Rev. Lett. **57**, 2520 (1986).

[14] P. Grangier, R. E. Slusher, B. Yurke, and A. LaPorta, Squeezed-Light–Enhanced Polarization Interferometer Phys. Rev. Lett. **59**, 2153 (1987).

[15] M. Xiao, L.-A. Wu, and H. J. Kimble, Precision Measurement Beyond the Shot-Noise Limit, Phys. Rev. Lett. **59**, 278 (1987).

[16] E. S. Polzik, J. Carri, and H. J. Kimble, Spectroscopy with Squeezed Light, Phys. Rev. Lett. **68**, 3020 (1992).

[17] K. Goda, O. Miyakawa, E. E. Mikhailov, S. Saraf, R. Adhikari, K. McKenzie, R. Ward, S. Vass, A. J. Weinstein, and N. Mavalvala, A quantum-enhanced prototype gravitational-wave detector, Nat. Phys. **4**, 472 (2008).

[18] R. Schnabel, Squeezed states of light and their applications in laser interferometers, Phys. Rep. **684**, 1 (2017).

[19] S. Pirandola, B. R. Bardhan, T. Gehring, C. Weedbrook, and S. Lloyd, Advances in photonic quantum sensing, Nature Photon **12**, 724 (2018).

[20] B. J. Lawrie, P. D. Lett, A. M. Marino, and R. C. Pooser, Quantum sensing with squeezed light, ACS Photonics **6**, 1307 (2019).

[21] E. Polino, M. Valeri, N. Spagnolo, and F. Sciarrino, Photonic quantum metrology, AVS Quantum Sci. **2**, 024703 (2020).

[22] R. Demkowicz-Dobrazanski, M. Jarzyna, and J. Kolodinsky, Quantum limits in optical interferometry, Prog. Opt. **60**, 345 (2015).

[23] H. Vahlbruch, M. Mehmet, K. Danzmann, and R. Schnabel, Detection of 15 dB Squeezed States of Light and Their Application for the Absolute Calibration of Photoelectric Quantum Efficiency, Phys. Rev. Lett. **117**, 110801 (2016).

[24] A. Schönbeck, F. Thies, and R. Schnabel, 13 dB squeezed vacuum states at 1550 nm from 12 mW external pump power at 775 nm, Opt. Lett. **43**, 110 (2018).

[25] H. F. Hofmann and T. Ono, High-photon-number path entanglement in the interference of spontaneously down-converted photon pairs with coherent laser light, Phys. Rev. A **76**, 031806(R) (2007).

[26] I. Afek, O. Ambar, and Y. Silberberg, High-NOON states by mixing quantum and classical light, Science **328**, 879 (2010).

[27] M. A. Taylor and W. P. Bowen, Quantum metrology and its application in biology, Phys. Rep. **615**, 1 (2016).

[28] P.-A. Moreau, E. Toninelli, T. Gregory, and M. J. Padgett, Imaging with quantum states of light, Nat. Rev. Phys. **1**, 367 (2019).

[29] I. Ruo-Berchera and I. P. Degiovanni, Quantum imaging with sub-Poissonian light: Challenges and perspectives in optical metrology, Metrologia **56**, 024001 (2019).

[30] C. A. Casacio, L. S. Madsen, A. Terrasson, M. Waleed, K. Barnscheidt, B. Hage, M. A. Taylor, and W. P. Bowen, Quantum-enhanced nonlinear microscopy, Nature (London) **594**, 201 (2021).

[31] M. A. Taylor, J. Janousek, V. Daria, J. Knittel, B. Hage, H.-A. Bachor, and W. P. Bowen, Biological measurement beyond the quantum limit, Nature Photon **7**, 229 (2013).

[32] R. Schnabel, N. Mavalvala, D. E. McClelland, and P. K. Lam, Quantum metrology for gravitational wave astronomy, Nat. Commun. **1**, 121 (2010).

[33] J. Abadie *et al.* (LIGO Collaboration), A gravitational wave observatory operating beyond the quantum shot-noise limit, Nat. Phys. **7**, 962 (2011).

[34] J. Aasi *et al.* (LIGO Collaboration), Enhanced sensitivity of the LIGO gravitational wave detector by using squeezed states of light, Nature Photon **7**, 613 (2013).

[35] R. Demkowicz-Dobrzański, K. Banaszek, and R. Schnabel, Fundamental quantum interferometry bound for the squeezed-light-enhanced gravitational wave detector GEO 600, Phys. Rev. A **88**, 041802(R) (2013).

[36] M. Tse *et al.* (LIGO Collaboration), Quantum-Enhanced Advanced LIGO Detectors in the Era of Gravitational-Wave Astronomy, Phys. Rev. Lett. **123**, 231107 (2019).

[37] F. Acernese *et al.* (VIRGO Collaboration), Increasing the Astrophysical Reach of the Advanced Virgo Detector via the Application of Squeezed Vacuum States of Light, Phys. Rev. Lett. **123**, 231108 (2019).

[38] S. S. Y. Chua, B. J. J. Slagmolen, D. A. Shaddock, and D. E. McClelland, Quantum squeezed light in gravitational-wave detectors, Class. Quantum Grav. **31**, 183001 (2014).

[39] C. Gross, H. Strobel, E. Nicklas, T. Zibold, N. Bar-Gill, G. Kurizki, and M. K. Oberthaler, Atomic homodyne detection of continuous-variable entangled twin-atom states, Nature (London) **480**, 219 (2011).

[40] C. D. Hamley, C S. Gerving, T. M. Hoang, E. M. Bookjans, and M. S. Chapman, Spin-nematic squeezed vacuum in a quantum gas, Nat. Phys. **8**, 305 (2012).

[41] J. Peise, I. Kruse, K. Lange, B. Lücke, L. Pezzè, J. Arlt, W. Ertmer, K. Hammerer, L. Santos, A. Smerzi, and C. Klempt, Satisfying the Einstein-Podolsky-Rosen criterion with massive particles, Nat. Comm. **6**, 8984 (2015).

[42] I. Kruse *et al.*, Improvement of an Atomic Clock using Squeezed Vacuum, Phys. Rev. Lett. **117**, 143004 (2016).

[43] L. Pezzè, A. Smerzi, M. K. Oberthaler, R. Schmied, and P. Treutlein, Quantum metrology with nonclassical states of atomic ensembles, Rev. Mod. Phys. **90**, 035005 (2018).

[44] F. Albarelli, M. Barbieri, M. G. Genoni, and I. Gianani, A perspective on multiparameter quantum metrology: From theoretical tools to applications in quantum imaging, Phys. Lett. A **384**, 126311 (2020).

[45] P. Komar, E. M. Kessler, M. Bishof, L. Jiang, A. S. Sø rensen, J. Ye, and M. D. Lukin, A quantum network of clocks, Nat. Phys. **10**, 582 (2014).

[46] E. Polzik and J. Ye, Entanglement and spin squeezing in a network of distant optical lattice clocks, Phys. Rev. A **93**, 021404 (2016).

[47] T. Baumgratz and A. Datta, Quantum Enhanced Estimation of a Multidimensional Field, Phys. Rev. Lett. **116**, 030801 (2016).

[48] S. Altenburg, M. Oszmaniec, S. Wölk, and O. Gühne, Estimation of gradients in quantum metrology Phys. Rev. A **96**, 042319 (2017).

[49] I. Apellaniz, I. Urizar-Lanz, Z. Zimborás, P. Hyllus, and G. Tóth, Precision bounds for gradient magnetometry with atomic ensembles, Phys. Rev. A **97**, 053603 (2018).

[50] Z. Hou, Z. Zhang, G.-Y. Xiang, C.-F. Li, G.-C. Guo, H. Chen, L. Liu, and H. Yuan, Minimal Tradeoff and Ultimate Precision Limit of Multiparameter Quantum Magnetometry under the Parallel Scheme, Phys. Rev. Lett. **125**, 020501 (2020).

[51] M. Jarzyna and R. Demkowicz-Dobrzański, Quantum interferometry with and without an external phase reference, Phys. Rev. A **85**, 011801(R) (2012).

[52] L. Pezzè, P. Hyllus, and A. Smerzi, Phase-sensitivity bounds for two-mode interferometers, Phys. Rev. A **91**, 032103 (2015).

[53] A. Z. Goldberg, I. Gianani, M. Barbieri, F. Sciarrino, A. M. Steinberg, and N. Spagnolo, Multiphase estimation without a reference mode, Phys. Rev. A **102**, 022230 (2020).

[54] X. Guo, C. R. Breum, J. Borregaard, S. Izumi, M. V. Larsen, T. Gehring, M. Christandl, J. S. Neergaard-Nielsen, and U. L. Andersen, Distributed quantum sensing in a continuous-variable entangled network, Nat. Phys. **16**, 281 (2020).

[55] Y. Xia, W. Li, W. Clark, D. Hart, Q. Zhuang, and Z. Zhang, Demonstration of a Reconfigurable Entangled Radio-Frequency Photonic Sensor Network, Phys. Rev. Lett. **124**, 150502 (2020).

[56] M. Reck, A. Zeilinger, H. J. Bernstein, and P. Bertani, Experimental Realization of Any Discrete Unitary Operator, Phys. Rev. Lett. **73**, 58 (1994).

[57] J. Nokkala, F. Arzani, F. Galve, R. Zambrini, S. Maniscalco, J. Piilo, N. Treps, and V. Parigi, Reconfigurable optical implementation of quantum complex networks, New J. Phys. **20**, 053024 (2018).

[58] P. C. Humphreys, M. Barbieri, A. Datta, and I. A. Walmsley, Quantum Enhanced Multiple Phase Estimation, Phys. Rev. Lett. **111**, 070403 (2013).

[59] T. J. Proctor, P. A. Knott, and J. A. Dunningham, Multiparameter Estimation in Networked Quantum Sensors, Phys. Rev. Lett. **120**, 080501 (2018).

[60] W. Ge, K. Jacobs, Z. Eldredge, A. V. Gorshkov, and M. Foss-Feig, Distributed Quantum Metrology with Linear Networks and Separable Inputs, Phys. Rev. Lett. **121**, 043604 (2018).

[61] Z. Eldredge, M. Foss-Feig, J. A. Gross, S. L. Rolston, and A. V. Gorshkov, Optimal and secure measurement protocols for quantum sensor networks, Phys. Rev. A **97**, 042337 (2018).

[62] M. Gessner, L. Pezzè, and A. Smerzi, Sensitivity Bounds for Multiparameter Quantum Metrology, Phys. Rev. Lett. **121**, 130503 (2018).

[63] R. Nichols, P. Liuzzo-Scorpo, P. A. Knott, and G. Adesso, Multiparameter Gaussian quantum metrology, Phys. Rev. A **98**, 012114 (2018).

[64] Q. Zhuang, J. Preskil, and L. Jiang, Distributed quantum sensing enhanced by continuous-variable error correction, New J. Phys. **22**, 022001 (2020).

[65] Q. Zhuang, Z. Zhang, and J. H. Shapiro, Distributed quantum sensing using continuous-variable multipartite entanglement, Phys. Rev. A **97**, 032329 (2018).

[66] C. Oh, C. Lee, S. H. Lie, and H. Jeong, Optimal distributed quantum sensing using Gaussian states, Phys. Rev. Res. **2**, 023030 (2020).

[67] M. Gessner, A. Smerzi, and L. Pezzè, Multiparameter squeezing for optimal quantum enhancements in sensor networks, Nat. Commun. **11**, 3817 (2020).

[68] D. Triggiani, P. Facchi, and V. Tamma, Heisenberg scaling precision in the estimation of functions of parameters in linear optical networks, Phys. Rev. A **104**, 062603 (2021).

[69] P. A. Knott, T. J. Proctor, A. J. Hayes, J. F. Ralph, P. Kok, and J. A. Dunningham, Local versus global strategies in multiparameter estimation, Phys. Rev. A **94**, 062312 (2016).

[70] M. A. Ciampini, N. Spagnolo, C. Vitelli, L. Pezzè, A. Smerzi, and F. Sciarrino, Quantum-enhanced multiparameter estimation in multiarm interferometers, Sci. Rep. **6**, 28881 (2016).

[71] E. Polino, M. Riva, M. Valeri, R. Silvestri, G. Corrielli, A. Crespi, N. Spagnolo, R. Osellame, and F. Sciarrino, Experimental multiphase estimation on a chip, Optica **6**, 288 (2019).

[72] M. Valeri, E. Polino, D. Poderini, I. Gianani, G. Corrielli, A. Crespi, R. Osellame, N. Spagnolo, and F. Sciarrino, Experimental adaptive Bayesian estimation of multiple phases with limited data, npj Quantum Inf. **6**, 92 (2020).

[73] S.-R. Zhao *et al.*, Field Demonstration of Distributed Quantum Sensing without Post-Selection, Phys. Rev. X **11**, 031009 (2021).

[74] L.-Z. Liu, Y.-Z. Zhang, Z.-D. Li, R. Zhang, X.-F. Yin, Y.-Y. Fei, L. Li, N.-L. Liu, F. Xu, Y.-A. Chen, and J.-W. Pan, Distributed quantum phase estimation with entangled photons, Nat. Phot. **15**, 137 (2021).

[75] K. Qian, Z. Eldredge, W. Ge, G. Pagano, C. Monroe, J. V. Porto and A. V. Gorshkov, Heisenberg-scaling measurement protocol for analytical functions with quantum sensor networks, Phys. Rev. A **100**, 042304 (2019).

[76] J. Rubio, P. A. Knott, T. J. Proctor, and J. A. Dunningham, Quantum sensing network for the estimation of linear functions, J. Phys. A **53**, 344001 (2020).

[77] J. A. Gross and C. M. Caves, One from many: Estimating functions of many parameters, J. Phys. A **54**, 014001 (2021).

[78] C. W. Helstrom, *Quantum Detection and Estimation Theory* (Academic Press, New York, 1976).

[79] A. S. Holevo, *Probabilistic and Statistical Aspects of Quantum Theory* (North-Holland, Amsterdam, 1982).

[80] M. G. A. Paris, Quantum estimation for quantum technology. Int. J. Quant. Inf. **7**, 125 (2009).

[81] The matrix $\mathcal{F}_{\mathbf{Q}}$ has elements $(\mathcal{F}_{\mathbf{Q}})_{jk} = \mathrm{Tr}[\hat{\rho}(\hat{L}_j\hat{L}_k + \hat{L}_k\hat{L}_j)]$, and the Hermitian operators $\hat{L}_j$ ($j = 1, \ldots, d$) are defined by the relation $d\hat{\rho}_{\boldsymbol{\theta}}/d\theta_j = (\hat{L}_j\hat{\rho}_{\boldsymbol{\theta}} + \hat{\rho}_{\boldsymbol{\theta}}\hat{L}_j)/2$, and $\hat{\rho}_{\boldsymbol{\theta}}$ is the sensor's output state [78].

[82] K. Matsumoto, A new approach to the Cramér-Rao-type bound of the pure-state model, J. Phys. A **35**, 3111 (2002).

[83] L. Pezzè, M. A. Ciampini, N. Spagnolo, P. C. Humphreys, A. Datta, I. A. Walmsley, M. Barbieri, F. Sciarrino, and A. Smerzi, Optimal Measurements for Simultaneous Quantum Estimation of Multiple Phases, Phys. Rev. Lett. **119**, 130504 (2017).

[84] S. L. Braunstein and C. M. Caves, Statistical Distance and the Geometry of Quantum States, Phys. Rev. Lett. **72**, 3439 (1994).

[85] V. Gebhart, A. Smerzi, and L. Pezzè, Bayesian Quantum Multiphase Estimation Algorithm, Phys. Rev. Appl. **16**, 014035 (2021).

[86] B. Yurke, S. L. McCall, and J. R. Klauder, SU(2) and SU(11) interferometers, Phys. Rev. A **33**, 4033 (1986).

[87] A specific $\boldsymbol{U}_{\mathrm{QC}}$ and input port D identifies a unique vector $u_j = (\boldsymbol{U}_{\mathrm{QC}})_{Dj}$ but 2^d different (nonorthogonal) vectors $\{\tilde{u}_j\}_{j=1,\ldots,d}$, due to the freedom in the choice of sign for each of the relative phases χ_j.

[88] Let us show how the operator $\hat{W}$ is constructed. We take $\hat{W} = e^{-i\hat{H}}$, where $\hat{H} = \sum_{i,j=1}^{d} \hat{b}_i^\dagger \boldsymbol{F}_{ij}\hat{b}_j$ and $\boldsymbol{F}_{ij}$ is a $d \times d$ Hermitian matrix. According to the Baker-Campbell-Haussdorf formula, one has $e^{i\hat{H}}\hat{b}_D e^{-i\hat{H}} = \sum_{n=0}^{\infty} i^n (K_{\hat{H}})^n \hat{b}_D/n!$, where $(K_{\hat{H}})^n \hat{b}_D$ is recursively defined: $(K_{\hat{H}})^0\hat{b}_D = \hat{b}_D$, $(K_{\hat{H}})^1\hat{b}_D = [\hat{H}, \hat{b}_D]$ and $(K_{\hat{H}})^n\hat{b}_D = (K_{\hat{H}})^{(n-1)}[\hat{H}, \hat{b}_D]$ for $n > 1$. Then, resulting from our choice of $\hat{H}$, we have $(K_{\hat{H}})^n\hat{b}_D = \sum_{j=1}^{d}(\boldsymbol{F}^n)_{Dj}\hat{b}_j$, so that $e^{i\hat{H}}\hat{b}_D e^{-i\hat{H}} = \sum_{n=0}^{\infty} i^n \sum_{j=1}^{d}(\boldsymbol{F}^n)_{Dj}\hat{b}_j/n! = \sum_{j=1}^{d}[\sum_{n=0}^{\infty} i^n (\boldsymbol{F}^n)_{Dj}/n!]\hat{b}_j$. Therefore, if we choose $\boldsymbol{F}$ so that $\sum_{n=0}^{\infty} i^n(\boldsymbol{F}^n)_{Dj}/n! = w_j$, we get $e^{i\hat{H}}\hat{b}_D e^{-i\hat{H}} = \sum_{j=1}^{d} w_j\hat{b}_j$ and the construction is completed. Notice that $\sum_{n=0}^{\infty} i^n(\boldsymbol{F}^n)_{ij}/n!$ defines the exponential matrix $\sum_{n=0}^{\infty} i^n(\boldsymbol{F}^n)_{ij}/n! = (e^{i\boldsymbol{F}})_{ij}$.

[89] We have

$$\left|\sum_{j=1}^{d}|v_j|\right|^p \leqslant \sum_{j=1}^{d}|v_j|^p, \qquad 0 < p < 1,$$

to which $\mathcal{G}_{C_1}^{\mathrm{Q}}(\boldsymbol{v}) \geqslant 1$ can be reduced for $p = 2/3$. To prove the above inequality, we first notice that, for $p \leqslant q$, we have

$$\left|\sum_{j=1}^{d}|v_j|^q\right|^{1/q} \leqslant \left|\sum_{j=1}^{d}|v_j|^p\right|^{1/p}$$

expressing the fact that the p-norm $\|v\|_p$ of a vector is nondecreasing function of p. By an application of the triangular inequality and the above, taking $q = 1$ one gets

$$\left|\sum_{j=1}^{d} v_j\right| \leqslant \left(\sum_{j=1}^{d}|v_j|^p\right)^{1/p}$$

and raising both to the pth power we get our initial claim.

[90] The reverse Hölder's inequality,

$$\sum_{j=1}^{d}|x_j y_j| \geqslant \left(\sum_{j=1}^{d}|x_j|^p\right)^{1/p}\left(\sum_{j=1}^{d}|y_j|^{-q}\right)^{-1/q},$$

holds for any $p, q > 0$ such that $1/p - 1/q = 1$. The result $\mathcal{G}_{C_1}^{\mathrm{Q}}(\boldsymbol{v}) \leqslant d$ is found for $x_j = |v_j|$, $y_j = 1$, $p = 2/3$, and $q = 2$.

[91] The full expression for $\tilde{u}^T\mathcal{M}(\tilde{u})^{-1}\tilde{u}$ when taking $|\alpha_j|^2 = \bar{n}_c$ is

$$\tilde{u}^T\mathcal{M}(\tilde{u})^{-1}\tilde{u} = \bar{n}_c(e^{-2r} - 1)\left(\sum_{j=1}^{d}\frac{\tilde{u}_j^2}{\bar{n}_c - \tilde{u}_j^2\bar{n}_s}\right)^2 + \sum_{j=1}^{d}\frac{(\bar{n}_c + \tilde{u}_j^2\bar{n}_s)\tilde{u}_j^2}{(\bar{n}_c - \tilde{u}_j^2\bar{n}_s)^2},$$

which reduces to Eq. (60) for $\bar{n}_c - \tilde{u}_j^2\bar{n}_s \approx \bar{n}_c$ and taking into

account that $\sum_{j=1}^{d} \tilde{u}_j^2 = 1$. For a random choice of splitting network, the condition $\bar{n}_c - \tilde{u}_j^2 \bar{n}_s \approx \bar{n}_c$ can be understood as $d\bar{n}_c \gg \bar{n}_s$ since, on average, $\mathcal{E}_{\rm QC}[\tilde{u}_j^2] = 1/d$. Furthermore, for $d\bar{n}_c \gg \bar{n}_s$, we also have $d\bar{n}_c \approx \bar{n}_T$, therefore the condition to recover Eq. (60) is $\bar{n}_T \gg \bar{n}_s$.

[92] C. N. Gagatsos, D. Branford, and A. Datta, Gaussian systems for quantum-enhanced multiple phase estimation, Phys. Rev. A **94**, 042342 (2016).

[93] C. N. Gagatsos, D. Branford, and A. Datta, Erratum : Gaussian systems for quantum-enhanced multiple phase estimation, Phys. Rev. A **106**, 029903 (2022).

[94] Z. Jiang, Quantum Fisher information for states in exponential form, Phys. Rev. A **89**, 032128 (2014).

[95] L. Banchi, S. L. Braunstein, and S. Pirandola, Quantum Fidelity for Arbitrary Gaussian States, Phys. Rev. Lett. **115**, 260501 (2015).